MODE STRUCTURE OF A SEMICONDUCTOR LASER WITH FEEDBACK FROM TWO EXTERNAL FILTERS

P. SŁOWIŃSKI[*], B. KRAUSKOPF[†], S. WIECZOREK[‡]

Abstract. We investigate the solution structure and stability of a semiconductor laser receiving time-delayed and frequency-filtered optical feedback (FOF) from two external filters. This system is referred to as the 2FOF laser, and it has been used as pump laser in optical telecommunication and as light source in sensor applications. The underlying idea is that the two filter loops provide a means of stabilizing and controling the laser output. The mathematical model takes the form of delay differential equations for the (real-valued) population inversion of the laser active medium and for the (complex-valued) electric fields of the laser cavity and of the two filters. There are two time delays, which are the travel times of the light from the laser to each of the filters and back.

Our analysis of the 2FOF laser focuses on the basic solutions, known as continuous waves or external filtered modes (EFMs), which correspond to laser output with steady amplitude and frequency. These solutions have been studied for the case of a laser with only a single filtered optical feedback loop. Here, we demonstrate that the second filter drastically modifies the overall structure and stability of the EFMs. A particular challenge for the analysis of the EFMs lies in the need to cope with a considerable number of bifurcation parameters: the feedback phase difference dC_p which quantifies the level of interference between the two feedback signals, detunings Δ_1 and Δ_2 between the laser frequency and the peak frequencies of each filter, the common width Λ of the filters' transmittance profile, and two delay times τ_1 and τ_2.

To analyse the intricate geometric structure of the EFMs we consider the EFM-surface in the (ω_s, N_s, dC_p)-space of steady frequency ω_s, the corresponding steady population inversion N_s, and the feedback phase difference dC_p. The EFM-surface emerges as the natural object for the study of the 2FOF laser because it conveniently catalogues information about its available frequency ranges. We identify five transitions, through four different singularities and a cubic tangency, that change the type of the EFM-surface locally. These transitions determine the EFM-surface bifurcation diagram in the (Δ_1, Δ_2)-plane for different but fixed values of Λ, τ_1 and τ_2. In this way, we classify the possible types of the EFM-surface, which consist of a combination of bands (covering the entire dC_p-range) and islands (covering only a finite range of dC_p).

To investigate the stability of the EFMs, we compute curves of saddle-node and Hopf bifurcations, which interact at Bogdanov-Takens, saddle-node Hopf and Hopf-Hopf bifurcation points. We focus on those bifurcation curves that bound regions with stable EFMs on the EFM-surface, and we study how these stability regions evolve when parameters are changed along a chosen path in the (Δ_1, Δ_2)-plane. We identify potential sources of amplitude instabilities and uncover interesting connections between changes to the EFM-surface itself and changes to the EFM stability. From a viewpoint of practical interests, we find various bands and islands of stability on the EFM-surface that may be accessible experimentally.

Beyond their relevance for the 2FOF laser system, the results presented here also showcase how advanced tools from bifurcation theory and singularity theory can be employed to uncover and represent the complex solution structure of a delay differential equation model that depends on a considerable number of input parameters, including two time delays.

1. INTRODUCTION. Semiconductor lasers are very efficient in transforming electrical energy to coherent light. They consist of an optical cavity filled with semiconductor active medium where electron-hole pairs (or population inversion) are generated by an electrical pump current. As light passes through the active medium, it is amplified by stimulated recombination of electron-hole pairs. Reflections from semitransparent mirrors ensure multiple light passages through the active medium, leading to a build-up of high-intensity coherent light. A fraction of the light exits the cavity through one (or both) of the semitransparent mirrors, and it forms the laser beam [33, 46]. Semiconductor lasers are small (about 1 millimetre long and several micrometres wide), can easily be mass produced and are used in their millions in every day applications — most importantly, in optical telecommunication and optical storage systems. On the down side, semiconductor lasers are

[1]Mathematics Institute, Zeeman Building, University of Warwick, Coventry CV4 7AL, United Kingdom; the research of this author has been supported at the University of Bristol by a Great Western Research Initiative Studentship in collaboration with Bookham Technology.

[2]Department of Mathematics, The University of Auckland, Private Bag 92019, Auckland 1142, New Zealand.

[3]Mathematics Research Institute, CEMPS, University of Exeter, North Park Road, Exeter EX4 4QF, United Kingdom.

known to be very sensitive to optical influences, especially in the form of external optical feedback from other optical components (such as mirrors and lenses) and via coupling to other lasers. Depending on the exact situation, optical feedback may induce many different kinds of laser dynamics. Examples include increased stability [6, 23] but also a period doubling cascade to chaos [76], torus break-up [73], and a boundary crisis [72]. See, for example, [33, 38, 48, 63] as entry points to the extensive literature on the possible nonlinear dynamics in lasers with optical feedback.

The simplest and now classical example of optical feedback is conventional optical feedback (COF) where light is reflected on a normal mirror and then re-enters the laser [43]. However, other types of laser systems with optical feedback have been considered, including lasers with two COF feedback loops [56], with incoherent feedback [20], with optoelectronic feedback [44], with phase-conjugate feedback (PCF) [7, 37] and with filtered optical feedback (FOF) [14, 28]. In all these cases an external feedback loop, or external cavity, is associated with a delay time τ that arises from the travel time of the light before it re-enters the laser. Due to the fast time scales within a semiconductor laser (on the order of picoseconds), external optical paths of a few centimetres lead to considerable delay times that cannot be ignored. As a consequence, an optical feedback created by an external cavity allows the laser to operate at various compound-cavity modes. These modes are referred to as continuous waves (CWs) because the laser emits light with steady amplitude and a specific frequency. The CWs are the simplest nonzero solutions of the system and they form the backbone for understanding the overall dynamics, even when they are unstable. For example, the typical dynamics of a COF laser with irregular drop-outs of the power has been attributed to trajectories that pass closely near several CWs of saddle type [25, 60].

In practical applications a main concern is to achieve stable, and possibly tunable, laser operation. One method of achieving this has been to use filtered optical feedback where the reflected light is spectrally filtered before it re-enters the laser — one speaks of the (single-) FOF laser. As in any optical feedback system, important parameters are the delay time and the feedback strength. Moreover, FOF is a form of coherent feedback, meaning that the phase relationship between outgoing and returning light is also an important parameter. The interest in the FOF laser is due to the fact that filtering of the reflected light allows additional control over the behaviour of the output light by means of choosing the spectral width of the filter and its detuning from the laser frequency. The basic idea is that the FOF laser produces stable output at the central frequency of the filter, which is of interest, for example, for achieving stable frequency tuning of lasers for telecommunications applications [9].

The single-FOF laser system has recently been the subject of a number of experimental and theoretical studies [15, 18, 22, 23, 27, 28, 31, 52, 67, 77, 79, 80]. Here, we assume that a solitary laser (i.e. without feedback) emits light of constant intensity and frequency Ω_0. It has been shown that feedback from a filter can improve the laser performance [6, 23], but it can also induce a wide range of more complicated dynamics. Its CW solutions are called external filtered modes (EFMs) [77], and they lie on closed curves, called EFM-components, in the (ω_s, N_s)-plane of the lasing frequency ω_s (relative to the solitary laser frequency Ω_0) and population inversion N_s of the laser (the number of electron-hole pairs). The EFM-components are traced out by the EFMs as the phase of the electric field of the filter (relative to the phase of the laser field), called here the feedback phase C_p, is varied. An analysis in [28] into the dependence of the FOF laser on the filter width Λ and the detuning Δ between the filter central frequency and the solitary laser frequency showed that there may be at most two EFM-components: one around the solitary laser frequency and one around the filter peak-frequency. A stability and bifurcation analysis of EFMs in [17] shows that the FOF laser is very sensitive to changes in feedback phase C_p. Furthermore, the filter parameters Λ and Δ have a big influence on the possible (non-steady amplitude) dynamics [16, 19]. Importantly, in a single-FOF laser one can observe not only the well-known relaxation oscillations, but also so-called frequency oscillations where only the frequency of the laser field oscillates while

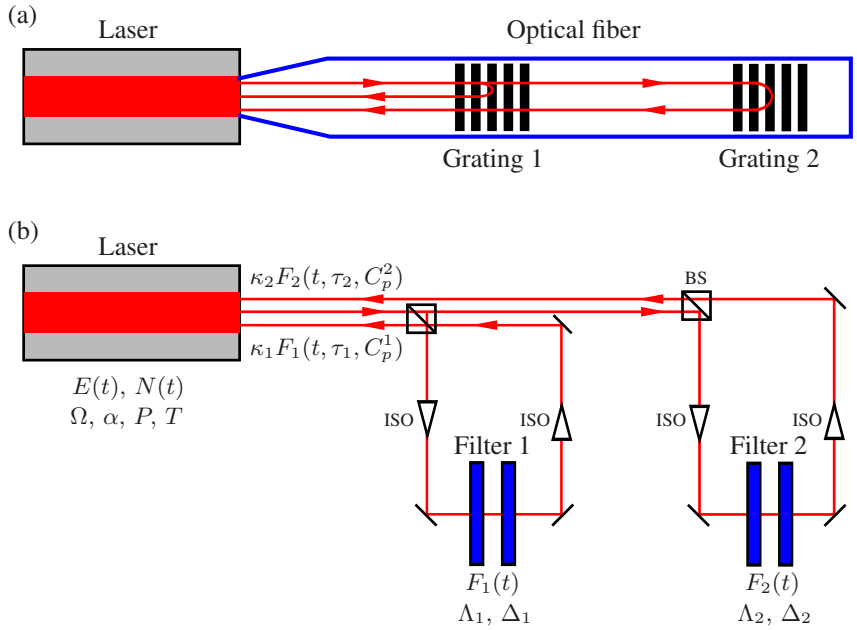

FIG. 1. *Sketch of a 2FOF semiconductor laser realized by coupling to an optical fiber with two fibre Bragg gratings (a), and by two (unidirectional) feedback loops with Fabry-Pérot filters (b); other optical elements are beam splitters (BS) and optical isolators (ISO).*

its amplitude remains practically constant [24]. In light of the strong amplitude-phase coupling of semiconductor lasers, the existence of frequency oscillations is somewhat surprising, and they are due to an interaction with the flanks of the filter transmittance profile [16]. An experimental study of the influence of feedback phase C_p and frequency detuning Δ on the single-FOF laser dynamics can be found in [19]. The limiting cases of small and large Λ and Δ have been considered in [28, 31, 77]. In all these studies the filter transmittance has a single maximum defining its central frequency; the FOF problem for periodic filter transmittance with multiple maxima and minima was considered in [67].

In a number of applications, such as the design of pump lasers for optical communication systems, the requirements on stable and reliable laser operation at a specific frequency are so stringent (especially when the device is on the ocean floor as part of a long-range fiber cable) that other methods of stabilisation have been considered. One approach is to employ FOF from two filtered feedback loops to stabilise the output of an (edge emitting) semiconductor laser [4, 9, 21, 53]. This laser system is referred to as the 2FOF laser for short, and it is the subject of the study presented here. The main idea is that the second filter provides extra frequency control over the laser output. In [4] it has been shown that a second filtered feedback loop may indeed improve the beam quality. In [21] an experimental setup has been realized and it was shown that 2FOF laser may show complicated dynamics as well; however, such dynamics have not been investigated further. The recent 2FOF experiment in [54] uses two independent feedback loops with with Fabry-Pérot filters, and it shows that the second feedback loop allows for precise control of the frequency components of the single-FOF laser; a period-doubling route to chaotic dynamics was also observed. With the focus on operational stability, industrial pump sources with enhanced wavelength and power stability performance due to a 2FOF design are available today [53]. The 2FOF laser has also been considered recently for frequency switching [9] and for sensor applications

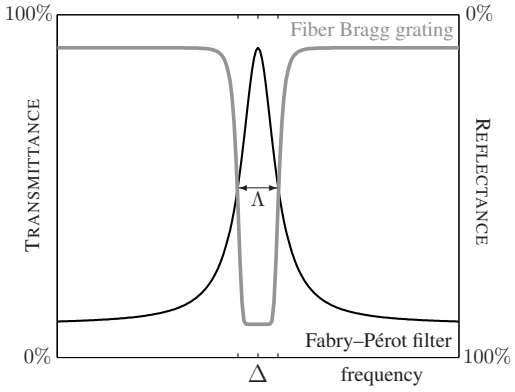

Fig. 2. *Spectrum of light transmitted (left scale) or reflected (right scale) by a Fabry-Pérot filter (black) and by a fiber Bragg grating (grey). The peak is at the filter's central frequency* Δ*, and the filter width* Λ *is defined as the full width at half maximum.*

[61, 62].

The filtered feedback of the 2FOF laser can be realized in two ways: either by reflection from an optical fibre with two fiber Bragg gratings (periodic changes of the refractive index) at given distances [62], or by transmission through two unidirectional feedback loops with Fabry-Pérot filters [54]; see Fig. 1. The two setups are equivalent in the sense that the overall spectral characteristics of the filtering is the same. More specifically, a fiber Bragg grating (FBG) has a peak in the reflectance at its central frequency, while a Fabry-Pérot filter (FP) has a peak in the transmittance at its central frequency; see Fig. 2. There are some important practical differences between the two setups in Fig. 1 that are discussed in more detail in Sec. 2. Nevertheless, the 2FOF laser in either form can be modelled by rate equations for the complex-valued electric field E inside the laser, for the real-valued population inversion N inside the laser, and for the complex-valued electric fields F_1 and F_2 inside the two filters. The 2FOF laser is hence described by a delay differential requation (DDE) model, which describes the time evolution of seven real-valued variables in the presence of two discrete time delays τ_1 and τ_2.

In this paper we perform an extensive study of the external filtered modes (EFMs) of the 2FOF laser as modelled by the DDE model (2.1)–(2.4), introduced in detail in Sec. 2 below. The analysis shows that the second filter has a significant influence on the structure of the EFMs. As was already mentioned, in the single-FOF laser one may find two (disjoint) EFM-components. However, in the 2FOF system, the number of (disjoint) EFM-components depends on the exact phase relationship between the two filters. When the filter loops have the same delay times, the interference between the filter fields can give rise to at most three EFM-components — one around the solitary laser frequency and one around the peak frequency of each filter. However, when the two delay times are not the same, then the interference between the filter fields may lead to any number of EFM-components.

The overall structure of the EFMs depends on a considerable number of system parameters and is quite complicated. To deal with this difficulty we consider the EFM-surface in the three-dimensional (ω_s, N_s, dC_p)-space, where dC_p is the phase difference between the two filter fields. The EFM-surface is a natural object for the study of basic solutions in the 2FOF laser because its intersection curves with planes of constant dC_p are the EFM-components, similar to those for the single-FOF laser. In other words, the EFM-surface is a catalogue of all possible EFM-components of the 2FOF laser that may be encountered for different, fixed value of dC_p. Indeed, the EFM-surface is rendered here via computing the EFM-components in a suitable number of cross sections

for fixed dC_p.

We first consider the EFM-surface for the case of two identical filter loops, but with nonzero phase difference between the filters. Then we study the influence of the two filter detunings Δ_1 and Δ_2 (from the solitary laser frequency Ω_0). This leads to a bifurcation diagram in the (Δ_1, Δ_2)-plane whose open regions correspond to different types of the EFM-surface. In the spirit of singularity theory, we present a classification where the rationale is to distinguish types of the EFM-surface that induce different corresponding EFM-components. The boundary curves in the (Δ_1, Δ_2)-plane are formed by singularity transitions (for example, through saddle points and extrema) of the EFM-surface, and they can be computed as such. We also consider how the EFM-surface bifurcation diagram in the (Δ_1, Δ_2)-plane changes with the spectral width Λ of the filters. This allows us to investigate the transition of the FOF laser between the two limiting cases: the case of an infinitesimally narrow filter profile, which corresponds to monochromatic optical injection at the filter peak frequency, and the case of an infinitely wide filter profile, which corresponds to conventional (i.e. unfiltered) optical feedback. Finally, we study effects of different delay times of the two filter loops to demonstrate that, in contrast to the single-FOF laser, the 2FOF laser may have an arbitrary number of EFM-components.

We also present an investigation of the stability of the EFMs. Its goal is limited, namely, to determine whether the properties of the EFM-surface are reflected by the regions of EFM-stability on it. As one might expect, there is no one-to-one correspondence between the two, as only a part of the EFMs on the EFM surface is stable. Nevertheless, we find clearly differing types of EFM-stability regions that are assocoated with certain types of the EFM surface.

Overall, the EFM-surface emerges as the natural object that one should consider to understand the steady-state dynamics of the 2FOF laser. Our analysis reveals a complicated dependence of the EFM-surface on several key parameters and provides a comprehensive and compact way of understanding the EFM solutions. These results are obtained through the computation of parameter-dependent surfaces of solutions of a DDE with two delays which, we believe, represents the state-of-the-art of numerical bifurcation analysis for DDEs with considerable numbers of parameters.

The paper is organised as follows. In section Sec. 2 we introduce the rate equation model of the 2FOF laser and discuss its properties. In Sec. 3 we define the EFMs and show how they can be computed as solutions of a transcendental equation and its envelope; furthermore, we introduce the EFM-components and the EFM-surface. Section 4 is devoted to the classification of the EFM surface into different types, where the two delays are assumed to be equal. In (4.1) we consider how the EFM-components for $dC_p = 0$ depend on the detunings of the two filters. We then present in Sec. 4.2 the types of EFM-surface for which the number of EFM components is independent of the choice of dC_p. In Sec. 4.3 we identify and study five transitions that change the number of EFM-components and, hence, the type of the EFM-surface. Section 4.4 presents the EFM-surface bifurcation diagram in the (Δ_1, Δ_2)-plane for fixed and identical filter widths Λ, together with representatives of the associated EFM-surface types. In Sec. 4.5 we show how the EFM-surface bifurcation diagram changes as Λ is varied from zero to very large values. This involves a bifurcation at infinity of the (Δ_1, Δ_2)-plane, which it is discussed in Sec. 4.6. The stability of the EFMs is the subject of Sec. 5. We first consider in Sec. 5.1 the EFM stability regions for two identical undetuned filter loops and then present in Sec. 5.2 the EFM-stability regions for representative types of the EFM-surface along a path in the (Δ_1, Δ_2)-plane. Section 6 discusses the influence of a nonzero difference $d\tau$ between the two delay times on the EFM surface structure and the associated EFM-stability regions. We conclude in Sec. 7, where we also present an outlook on future work and briefly discuss how (different types of) regions of stable EFMs of the 2FOF laser could be identified experimentally. Finally, the Appendix gives more details of how the EFM-surface has been rendered from data obtained from dedicated continuation runs with the packageDDE-BIFTOOL [11].

2. MODEL OF THE 2FOF LASER. The 2FOF design with fiber Bragg gratings (FBG) as in Fig. 1 (a) is the one that has been employed in industrial pump sources [53], and it is also the one considered in [21, 61, 62]; see also the analysis of FOF from a FBG in [51]. Its main advantage is that FBGs are simple and cheap to manufacture in a fiber at desired locations; furthermore, apart from the need to couple the light into the fiber without any direct reflections (to avoid COF), no additional optical elements are required so that the device is relatively simple; see Fig. 1 (a). The downside is that, once a FBG is imprinted into an optical fiber, it cannot be modified. Furthermore, the two filters are not independent feedback loops. When the two FBGs operate at different frequencies (as in the actual devices) then they are transparent to each other's central frequency, meaning that the first FBG only slightly weakens the light reflected from the second FBG and one may assume that there are no direct interactions between these two filters. However, when both FBGs operate very close to the same frequency then the feedback from the second FBG is almost completely blocked, so that the laser receives feedback only from one filter. Another issue is that the light reflected from a FBG is due to the interaction with the entire grating, which means that the round-trip time of the reflected light is not so easy to determine. Furthermore, the optical fiber and the FBGs are susceptible to mechanical strain and to thermal expansion. Such perturbations result in a modifications of the filter peak frequency and the feedback phase via changes of the feedback loop length at a sub-wavelength scale. For these reasons it is difficult to perform controlled experiments with the FBGs setup over large ranges of parameters of interest.

The experimental setup in Fig. 1 (b) is less practical in industrial applications, but it allows for exact and independent control of all relevant system parameters. More specifically, the FOF comes from two independent unidirectional filter loops that do not influence one another. The two delay times and feedback phases can easily be changed in the experiment as independent parameters. Furthermore, the system can be investigated for any combination of filter frequencies and widths (but note that every change of the filter properties requires a different FP filter). Finally, this experimental setup has recently been used successfully in studies of the 2FOF laser [54], as well as, with only a single FOF loop, in studies of the single-FOF laser [18, 19]. In particular, it has been shown that the system is modelled very well by a rate equation model where the filters are assumed to have a Lorentzian transmittance profile [28, 77].

In spite of the differences in terms of which parameter ranges can be explored in an experiment, both realisations of the 2FOF laser in Fig. 1 can be modelled by the dimensionless rate equations

$$\frac{dE}{dt} = (1 + i\alpha)N(t)E(t) + \kappa_1 F_1(t) + \kappa_2 F_2(t), \tag{2.1}$$

$$T\frac{dN}{dt} = P - N(t) - (1 + 2N(t))|E(t)|^2, \tag{2.2}$$

$$\frac{dF_1}{dt} = \Lambda_1 E(t - \tau_1)e^{-iC_p^1} + (i\Delta_1 - \Lambda_1)F_1(t), \tag{2.3}$$

$$\frac{dF_2}{dt} = \Lambda_2 E(t - \tau_2)e^{-iC_p^2} + (i\Delta_2 - \Lambda_2)F_2(t). \tag{2.4}$$

The well established assumptions here are that the delay times τ_1 and τ_2 are larger than the light roundtrip time inside the laser cavity and that the filters have a Lorentzian transmittance profile (Fig. 2); see [22, 28, 77] for more details. More specifically, one obtains Eqs. (2.1)–(2.4) as an extension of the rate equations model of the single-FOF laser [28, Eqs. (1)–(3)] with an additional equation for the field of the second filter.

Equation (2.1) describes the time evolution of the complex-valued slowly-varying electric field

Parameter	Meaning	Value
Laser		
P	pump parameter	3.5
α	linewidth enhancement factor	5
T	inversion decay rate / photon decay rate	100
Feedback loops		
κ_1	first loop feedback strength	from 0.01 to 0.05
κ_2	second loop feedback strength	from 0.01 to 0.05
τ_1	first loop round-trip time	500
τ_2	second loop round-trip time	500 to 800
C_p^1	first loop feedback phase	2π-periodic
C_p^2	second loop feedback phase	2π-periodic
Filters		
Δ_1	first filter central frequency detuning	from -0.82 to 0.82
Δ_2	second filter central frequency detuning	from -0.82 to 0.82
Λ_1	first filter spectral width	from 0.0 to 0.5
Λ_2	second filter spectral width	from 0.0 to 0.5

TABLE 1
System parameters and their values.

amplitude $E(t) = E_x(t) + iE_y(t)$ of the laser. Equation (2.2) describes the normalized population inversion $N(t)$ within the laser active medium. In (2.1)–(2.2) the material properties of the laser are described by the linewidth enhancement factor α (which quantifies the amplitude-phase coupling or frequency shift under changes in population inversion [32]), the ratio T between the population inversion and the field decay rates, and the dimensionless pump parameter P. Time is measured in units of the inverse photon decay rate of $10^{-11}s$. Throughout, we use values of the semiconductor laser parameters from [17] that are given in table 1.

The two FOF loops enter equation (2.1) as feedback terms $\kappa_1 F_1(t)$ and $\kappa_2 F_2(t)$ with normalised feedback strengths κ_1 and κ_2 [70, p. 93] of the normalised complex-valued fields $F_1(t)$ and $F_2(t)$ of the two filters. In general, the presence of a filter in the system gives rise to an integral equation for the filter field. However, in the case of a Lorentzian transmittance profile as assumed here, derivation of the respective integral equation yields the description of the filter fields by DDEs (2.3) and (2.4); see [77] for more details.

The two filter loops are characterised by a number of parameters. As for any coherent feedback, we have the feedback strength κ_i, the delay time τ_i and the feedback phase C_p^i of the respective filter field, which is accumulated by the light during its travel through the feedback loop, where $i = 1$ or $i = 2$. Hence, $C_p^i = \Omega_0 \tau_i$. Owing to the large difference in time scales between the optical period $2\pi/\Omega_0$ and the delay time τ_i, one generally considers τ_i and C_p^i as independent parameters. Namely, as has been justified experimentally [19, 30], changing the length of the feedback loop on the optical wavelength scale of nanometres changes C_p^i, but effectively does not change τ_i. Two different strategies for changing C_p^i have been used experimentally: in [19] this is achieved by changing the length of the feedback loop on the optical wavelength scale with a piezo actuator, and in [30] C_p is varied indirectly through very small changes in the pump current which, in turn, affect Ω_0.

The optical properties of the filters are given by the detunings Δ_i of their central frequencies from the solitary laser frequency, and by their spectral widths Λ_i, defined as the frequency width

at half-maximum (FWHM) of the (Lorentzian) transmittance profile. In this paper we consider the filter detunings Δ_1 and Δ_2 as independent parameters. Furthermore, we keep both feedback strengths as well as both filter widths equal, so that throughout we use

$$\kappa := \kappa_1 = \kappa_2 \quad \text{and} \quad \Lambda := \Lambda_1 = \Lambda_2.$$

The values of the feedback parameters are also given in table 1.

We remark that system (2.1)–(2.4) contains as limiting cases two alternative setups that have also been considered for the stabilisation of the laser output. First, when the spectral width of only one filter is very large (so that there is no effective frequency filtering) then the laser effectively receives feedback from an FOF loop and from a COF loop; see, for example, [3, 13]. Second, when the spectral widths of both filters are very large then one is dealing with a laser with two external COF loops; see, for example, [57, 66] and the discussion in Sec. 4.7.

System (2.1)–(2.4) shares symmetry properties with many other systems with coherent optical feedback. Namely, the system has an S^1-symmetry [29, 34, 40] given by simultaneous rotation over any fixed angle of the laser field E and both filter fields F_1 and F_2. This symmetry can be expressed by the transformation

$$(E, N, F_1, F_2) \mapsto \left(Ee^{i\beta}, N, F_1 e^{i\beta}, F_2 e^{i\beta}\right) \tag{2.5}$$

for any $0 \leq \beta \leq 2\pi$. In other words, solutions (trajectories) of (2.1)–(2.4) are not isolated but come in S^1-families. In particular, the EFMs introduced in the next chapter are group orbits under this symmetry, and they typically take the form of circular limit cycles in the (E, N, F_1, F_2) phase space [17, 34]. To facilitate numerical continuation and stability analysis with DDE-BIFTOOL, we exploit the symmetry and study EFMs as isolated equilibria in a transformed system which is obtained as follows. After substitution of $\left(Ee^{ibt}, N, F_1 e^{ibt}, F_2 e^{ibt}\right)$ into (2.1)–(2.4) and dividing through by an exponential factor we obtain a new system where the *reference frequency* b is an additional unknown. A suitable choice of b 'freezes' motion along the group orbit but introduces phase indeterminacy of E — an EFM becomes a circle of inifintely many equilibria. To remove the phase indeterminacy we impose a suitable algebraic constraint which fixes the argument of E and, thus, selects one of infinitely many equilibria; see [29, 58] and Appendix A for details.

There is also a rather trivial symmetry property: the feedback phases C_p^i are 2π-periodic parameters, which means that they are invariant under the translation

$$C_p^i \mapsto C_p^i + 2\pi. \tag{2.6}$$

This property is quite handy, because results can be presented either over a compact fundamental interval of width 2π or on the covering space $\mathbb{R}$ of C_p^i; see also [17].

3. EXTERNAL FILTERED MODES. l The simplest nonzero solutions of the 2FOF laser correspond to the laser emitting monochromatic light with steady amplitude and specific frequency ω_s (relative to the solitary laser frequency Ω_0). These solutions are the external filtered modes or EFMs. Mathematically, an EFM is a group orbit of (2.1)–(2.4) under the S^1-symmetry (2.5), which means that it takes the form

$$(E(t), N(t), F_1(t), F_2(t)) = \left(E_s e^{i\omega_s t}, N_s, F_s^1 e^{i(\omega_s t+\phi_1)}, F_s^2 e^{i(\omega_s t+\phi_2)}\right). \tag{3.1}$$

Here, E_s, F_s^1 and F_s^2 are steady and real-valued amplitudes of the laser and filter fields, N_s is the corresponding steady population inversion, a constant ω_s is the lasing frequency, and constants ϕ_1, ϕ_2 are the phase shifts between the laser field and the two filter fields. To find the EFMs we follow the method presented in [28, 29]. We substitute ansatz (3.1) into (2.1)–(2.4) and separate real and imaginary parts to obtain

$$\Omega(\omega_s) - \omega_s = 0 \tag{3.2}$$

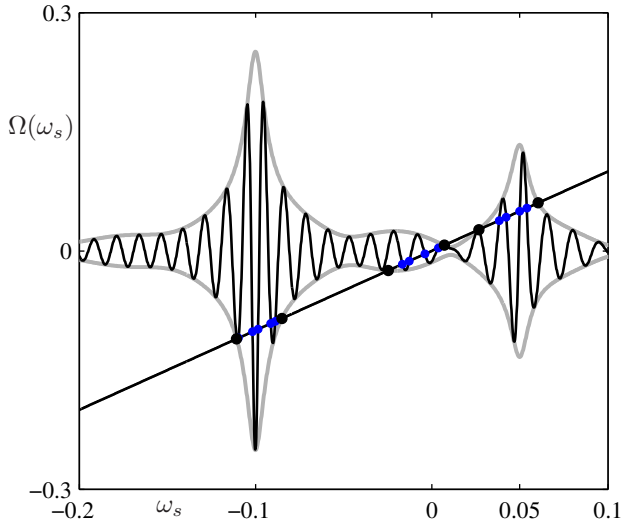

FIG. 3. *The graph of* (3.3) *(black curve) oscillates between its envelope (grey curve) given by* (3.9)*. Frequencies of EFMs (blue dots) are found from intersection points of the graph of* $\Omega(\omega_s)$ *with the diagonal; also shown are the intersection points (black dots) with the envelope. Here* $C_p^1 = 0$*,* $C_p^2 = \pi/3$*,* $\Delta_1 = -0.1$*,* $\Delta_2 = 0.05$*,* $\kappa_1 = 0.05$*,* $\kappa_2 = 0.025$*,* $\Lambda_1 = \Lambda_2 = 0.005$*,* $\tau_1 = 500$ *and* $\tau_2 = 400$*.*

where

$$\Omega(\omega_s) = -\sqrt{1+\alpha^2}\left(\frac{\kappa_1\Lambda_1\sin\left(\phi_1+\tan^{-1}(\alpha)\right)}{\sqrt{{\Lambda_1}^2+(\omega_s-\Delta_1)^2}}+\frac{\kappa_2\Lambda_2\sin\left(\phi_2+\tan^{-1}(\alpha)\right)}{\sqrt{{\Lambda_2}^2+(\omega_s-\Delta_2)^2}}\right), \tag{3.3}$$

and

$$\phi_i \quad = \quad \omega_s\tau_i + C_p^i + \tan^{-1}\left(\frac{\omega_s-\Delta_i}{\Lambda_i}\right). \tag{3.4}$$

Equation (3.2) is a transcendental and implicit equation that allows one to determine all possible frequencies ω_s of the EFMs for a given set of filter parameters. More specifically, the sought frequency values ω_s of the 2FOF laser can be determined from (3.2) numerically by root finding; for example, by Newton's method in combination with numerical continuation. The two terms of the sum in the parentheses of (3.3) correspond to the first and the second filter, respectively. If one of the κ_i is set to zero, then (3.2) reduces to the transcendental equation from [28] for the frequencies of EFMs of the single-FOF laser. The advantage of the formulation of (3.2) is that it has a nice geometric interpretation: $\Omega(\omega_s)$ is a function of ω_s that oscillates between two fixed envelopes. More precisely, when C_p^1 or C_p^2 are changed over 2π the graph of $\Omega(\omega_s)$ sweeps out the area in between the envelopes.

Figure 3 shows an example of the solutions of (3.2) as intersection points (blue dots) between the oscillatory function $\Omega(\omega_s)$ and the diagonal (the straight line through the origin with slope 1); see also [77]. Once ω_s is known, the corresponding values of the other state variables of the EFMs

can be found from

$$N_s = -\left(\frac{\kappa_1 \Lambda_1 \cos(\phi_1)}{\sqrt{{\Lambda_1}^2 + (\omega_s - \Delta_1)^2}} + \frac{\kappa_2 \Lambda_2 \cos(\phi_2)}{\sqrt{{\Lambda_2}^2 + (\omega_s - \Delta_2)^2}} \right), \tag{3.5}$$

$$E_s = \sqrt{\frac{P - N_s}{1 + 2N_s}}, \tag{3.6}$$

$$F_s^1 = \frac{E_s \Lambda_1}{\sqrt{{\Lambda_1}^2 + (\omega_s - \Delta_1)^2}}, \tag{3.7}$$

$$F_s^2 = \frac{E_s \Lambda_2}{\sqrt{{\Lambda_2}^2 + (\omega_s - \Delta_2)^2}}. \tag{3.8}$$

This means that an EFM is, in fact, uniquely determined by its value of ω_s. Furthermore, it is useful to consider the envelope of $\Omega(\omega_s)$ (grey curves) so that Figure 3 represents all the relevant geometric information needed to determine and classify EFMs. Note that in this specific example the EFMs are separated into three groups. The diagonal intersects the region bounded by the envelope in three disjoint intervals, in which the frequency ω_s of the EFMs may lie; these intervals correspond to three different EFM-components as is discussed in Sec. 3.1. As Fig. 3 suggests, EFMs are created and lost in saddle-node bifurcations when an extremum of the (black) graph passes through one of the boundary points (black dots) as a parameter (for example, C_p^1) is changed.

This geometric picture is very similar to that for the single-FOF laser [28], but there is an important difference. The envelope of $\Omega(\omega_s)$ for the FOF laser is found by considering the extrema of the sine function (in (3.3) for, say, $\kappa_2 = 0$). It turns out that the envelope for the single-FOF laser is described by a polynomial of degree four, whose roots are the boundary points of at most two intervals (or components) with possible EFMs [28]. However, for the 2FOF laser, considering the extrema of the two sine functions in (3.3) is not sufficient since they appear in a sum. Hence, we also need to consider mixed terms resulting from the summation. With the use of standard trigonometric formulae, the equation for the envelope can be found as

$$\Omega_e(\omega_s) = \pm \sqrt{1+\alpha^2} \Bigg[\frac{\kappa_1^2 \Lambda_1^2}{\Lambda_1^2 + (\omega_s - \Delta_1)^2} + \frac{\kappa_2^2 \Lambda_2^2}{\Lambda_2^2 + (\omega_s - \Delta_2)^2} + \frac{2\kappa_1 \kappa_2 \Lambda_1 \Lambda_2 \cos\left(C_p^2 - C_p^1 + \omega_s \, (\tau_2 - \tau_1) + \tan^{-1}\left(\frac{\omega_s - \Delta_2}{\Lambda_2}\right) - \tan^{-1}\left(\frac{\omega_s - \Delta_1}{\Lambda_1}\right)\right)}{\sqrt{\Lambda_1^2 + (\omega_s - \Delta_1)^2}\sqrt{\Lambda_2^2 + (\omega_s - \Delta_2)^2}} \Bigg]^{1/2}. \tag{3.9}$$

Indeed, when one of the κ_i is set to zero then (3.9) reduces to the fourth-order polynomial describing the envelope of the single-FOF laser in [28]. However, for general values of the parameters, (3.9) is a transcendental equation, and not a polynomial of degree six as one might have hoped; nevertheless, by means of (3.9) the envelope $\Omega_e(\omega_s)$ can be plotted readily.

The transcendental nature of (3.9) means that the study of the EFM structure of the 2FOF laser is a considerable challenge. As is shown here, the key is to find a suitable geometric viewpoint that allows one to understand the dependence of the EFMs on the different filter loop parameters.

A first observation is that (3.9) depends on the differences

$$dC_p := C_p^2 - C_p^1 \quad \text{and} \quad d\tau := \tau_2 - \tau_1,$$

which we will, hence, consider as parameters in what follows; note that dC_p is 2π-periodic as well.

3.1. EFM-components of the 2FOF laser. It is well-known for the single-FOF laser that its EFMs lie on closed curves in the (ω_s, N_s)-plane. These curves are called EFM-components, and they arise as the set of all EFMs found for different values of feedback phase C_p, whilst the other parameters of the system are fixed. More specifically, when C_p is changed, EFMs are born in a saddle-node bifurcation, then move over the respective EFM-component in the direction of increasing ω_s, and finally disappear again in another saddle-node bifurcation. From an experimental point of view, EFM-components are quite natural objects that can be measured as groups of EFMs whose frequencies vary with the feedback phase C_p; see [19]. For the single-FOF laser one finds either one or two EFM-components, depending on the properties of the filter. Intuitively, one expects one EFM-component centred around the solitary laser frequency and, if the detuning Δ is large enough, a second EFM-component around the filter central frequency. As was already mentioned, the exact dependence on the filter properties can be studied for the single-FOF laser by considering the roots of a polynomial of degree four that arises from the equation for the envelope of the EFMs; see [28] for details.

We now consider EFM-components of the 2FOF, which we define as the branches of EFMs that one finds when the feedback phases, C_p^1 or C_p^2 are changed while the feedback phase difference dC_p is fixed. This definition is the appropriate generalisation from the single-FOF laser [28]. The underlying idea is that the value of dC_p determines the interference of the light from the two filtered feedback loops and, hence, an important property of the overall feedback the laser sees.

For the 2FOF laser the structure of the EFM-components is quite a lot more complicated than for the single-FOF laser. Intuitively, one may think that now up to three EFM-components may occur in the (ω_s, N_s)-plane: one centred around the solitary laser frequency and two more around the peak frequencies of the two filters. However, this intuition is not correct, and we will show that there may, in fact, be any number of EFM-components. Physically, the reason for this vastly more complicated EFM structure of the 2FOF laser is the interference between the two filter fields, which can be interpreted as giving rise to a complicated 'effective' filter profile. Mathematically, the reason behind the more complicated EFM structure lies in the transcendental nature of the envelope equation (3.9).

We now proceed with providing a geometrical representation of the EFM structure of the 2FOF laser in dependence on system parameters. Since the transcendental EFM equation (3.2) is complicated and depends on all system parameters, its solutions can only be found numerically (except for certain very special choices of the parameters). From the value of the EFM frequency ω_s one can compute the values of the other EFM quantities E_s, N_s, F_s^1, F_s^2, ϕ_1 and ϕ_2. In particular, the inversion N_s can be expressed as a function of ω_s as

$$\begin{aligned} N_s^2 + (\omega_s - \alpha N_S)^2 =& \frac{\kappa_1^2 \Lambda_1^2}{{\Lambda_1}^2 + (\omega_s - \Delta_1)^2} + \frac{\kappa_2^2 \Lambda_2^2}{{\Lambda_2}^2 + (\omega_s - \Delta_2)^2} + \\ & \frac{2\kappa_1\kappa_2\Lambda_1\Lambda_2 \cos\left(dC_p + \omega_s\, d\tau + \tan^{-1}\left(\frac{\omega_s-\Delta_2}{\Lambda_2}\right) - \tan^{-1}\left(\frac{\omega_s-\Delta_1}{\Lambda_1}\right)\right)}{\sqrt{{\Lambda_1}^2 + (\omega_s - \Delta_1)^2}\sqrt{{\Lambda_2}^2 + (\omega_s - \Delta_2)^2}}. \end{aligned} \tag{3.10}$$

From this quadratic expression we can conclude that for any ω_s there are either no, one or two solutions for N_s. In particular, any EFM-component is a smooth closed curve that consists of two branches, one with a higher and one with a lower value of N_s, which connect at two points where

(3.10) has exactly one solution. EFM-components in the (ω_s, N_s)-plane can be computed from the implicit transcendental equations (3.2) and (3.10) by root solving, ideally in combination with numerical continuation. An alternative approach is to continue EFMs in parameters as periodic orbits of the governing system (2.1)–(2.4) of delay differential equations or as equilibria of the transformed system described in Appendix 1. Either can be achieved with the numerical continuation package DDE-BIFTOOL; additionaly, the stability of the EFMs can be determined with DDE-BIFTOOL.

The starting point of our study of the EFM structure is the special case that the two filters are identical, apart from having differing feedback phases C_p^1 and C_p^2. Hence, we now set

$$\Delta_1 = \Delta_2, \quad \text{and} \quad \tau_1 = \tau_2.$$

The EFMs for this special case are given by the EFMs of a corresponding single-FOF laser with effective feedback strength

$$\kappa^{\text{eff}} \quad = \quad 2\kappa \cos\left(\frac{dC_p}{2}\right) \tag{3.11}$$

and effective feedback phase

$$C_p^{\text{eff}} = \left(C_p^1 + C_p^2\right)/2.$$

In other words, we obtain a non-trivial reduction of the 2FOF laser to the single-FOF laser, where the feedback phase difference dC_p arises as a natural parameter that controls the effective feedback strength κ^{eff} as a result of interference between the two filter fields. One extreme case is that of constructive interference when $dC_p = 0$ so that $\kappa^{\text{eff}} = 2\kappa$. The other extreme is the case of destructive interference when $dC_p = \pi$ and $\kappa^{\text{eff}} = 0$. Hence, by changing dC_p we can 'switch on' or 'switch off' the overall filter field that the laser sees.

3.2. The EFM-surface of the 2FOF laser. To be able to study the EFM-components of the 2FOF laser more comprehensively, we now consider the EFM-surface in (ω_s, N_s, dC_p)-space. In other words, in this space, the EFM-surface is considered as the one-parameter family (parametrised by dC_p) of actual EFM-components themselves, which arise naturally as closed curves in the (ω_s, N_s)-plane by intersection with planar sections given by $dC_p = const$. In practice, an EFM-component for a given $dC_p = const$ is computed by continuation of an EFM in the parameters C_p^1 and ω_s, while setting $C_p^2 = C_p^1 + dC_p$; the EFM-surface is then rendered from a sufficient number of EFM-components for fixed dC_p; see Appendix A for details.

To illustrate the basic concept, Fig. 4 shows the EFM-surface for the simplest case of identical filters that are also undetuned, that is, $\Delta_1 = \Delta_2 = 0$. For this special choice there is always a single EFM-component of the correpsonding single-FOF laser with κ^{eff} given by (3.11). Panel (a) shows the EFM-surface for $dC_p \in [-\pi, \pi]$ intersected with the two planes given by $dC_p = 0$ and $dC_p = 0.9\pi$, respectively. The corresponding EFM-components arise from the shape of the envelope given by (3.9); it is shown in panels (b1) and (c1) together with the solution curve of (3.3) for $C_p^1 = 0$. The EFM-components themselves, with these EFMs on them, are shown in panels (b2) and (c2). Figure 4 illustrates that changing dC_p results in a change in the EFM-component, as well as the number of EFMs. For the shown case of two identical filters with equal delay times we can say more: here the change of the EFM-component is entirely due to the effective feedback rate κ^{eff} as described by (3.11). In other words, the EFM-surface is composed of the EFM-components of the corresponding single-FOF laser with κ^{eff} as determined by dC_p. The EFM-component is maximal for the constructive-interference case $dC_p = 0$, and it shrinks when dC_p is changed. This also means that fewer EFMs exist; compare Fig. 4 (b1) and (c1). Finally, as the case of entirely destructive interference for $dC_p = \pi$ is approached, the EFM-component shrinks down to a point, which is the degenerate EFM corresponding to the unique solitary laser mode.

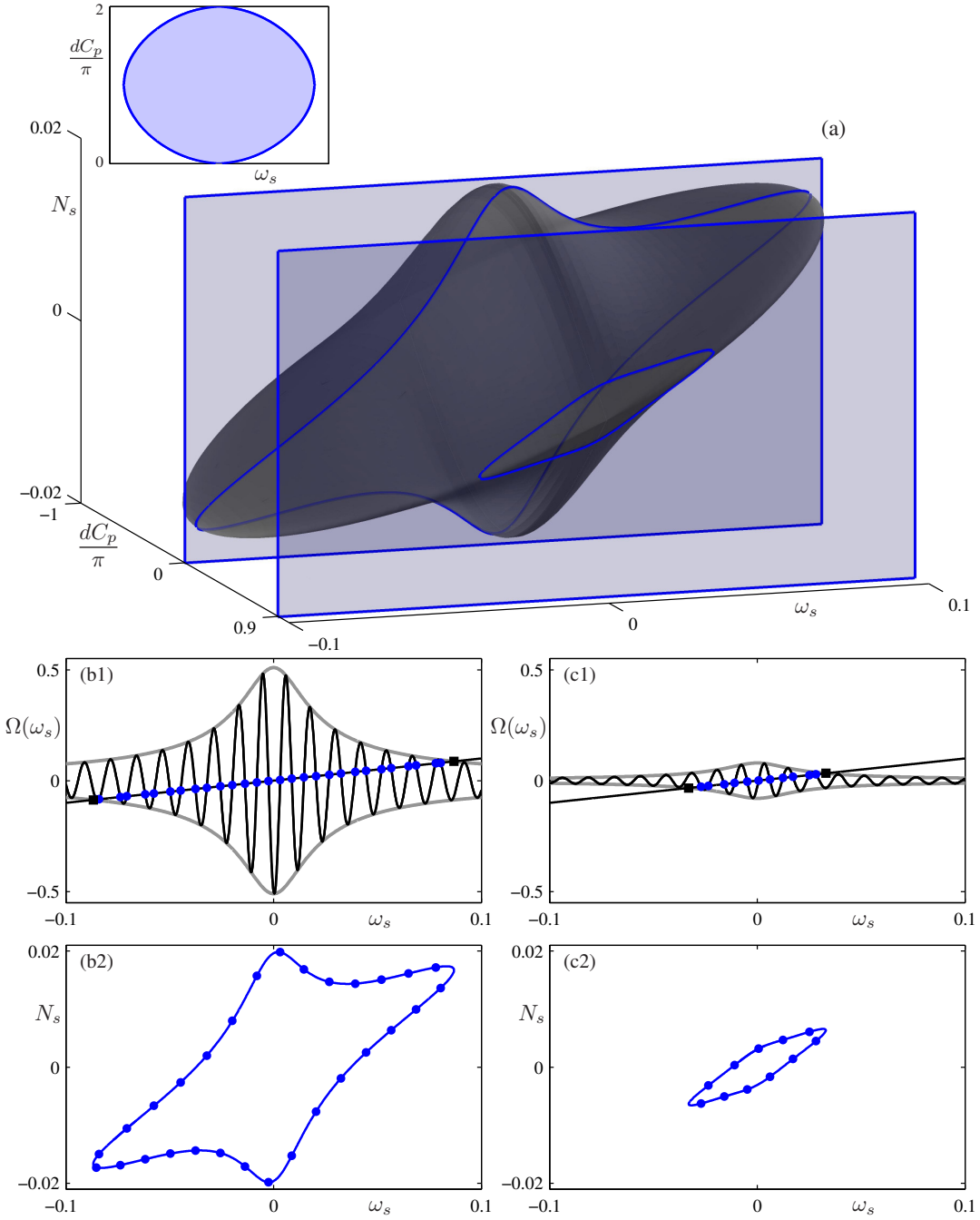

FIG. 4. *EFM-components arising as sections through the EFM-surface. Panel (a) shows the EFM-surface in* (ω_s, N_s, dC_p)*-space, intersected with the planes defined by* $dC_p = 0$ *and* $dC_p = 0.9\pi$*, respectively. Panels (b1) and (c1) show the corresponding envelopes (grey curves) given by* (3.9)*. The black solution curve of* (3.3) *inside it is the one for* $C_p^1 = 0$*; it gives rise to the marked blue EFMs. Panels (b2) and (c2) show the two respective EFM-components and individual EFMs (blue dots) in the* (ω_s, dC_p)*-plane. Shown is the case of two identical filters with* $\Delta_1 = \Delta_2 = 0$*.*

We conclude from this section that the EFM-surface in (ω_s, N_s, dC_p)-space has emerged as the main object of study. It represents the EFM structure of the 2FOF laser in a convenient geometric way; in particular, EFM-components can easily be obtained as planar slices for fixed dC_p.

4. CLASSIFICATION OF THE EFM-SURFACE FOR $d\tau = 0$. So far we have only considered the special case that the two filters are identical and not detuned from the laser; furthermore, the two delay times are equal. We now address the question how the EFM-surface changes as the system is moved away from this special point in the space of parameters. In this section we consider the case that the two filter loops have the same delay time, that is, $d\tau = 0$. The influence of a difference in delay times is the subject of Sec. 6.

We start by considering in Sec. 4.1 how the EFM-components depend on the detunings Δ_1 and Δ_2 for fixed $dC_p = 0$. We then proceed to study how the EFM-surface itself changes with Δ_1 and Δ_2. This can be represented for a fixed filter width Λ of both filters by an EFM-surface bifurcation diagram in the (Δ_1, Δ_2)-plane, where each open region corresponds to a different type of EFM-surface. In Sec. 4.2 we first consider the case that the EFM-surface gives rise to a dC_p-independent number of EFM-components. We then introduce in Sec. 4.3 five codimension-one singularity transitions — through extrema and saddle points, and through a cubic tangency (with respect to $dC_p = const$) — that change the EFM-surface in terms of how many EFM-components it induces when sliced for fixed dC_p. These five singularity transitions induce a division of the (Δ_1, Δ_2)-plane into open regions of different EFM-surface type. In Sec. 4.3.1 we discuss EFM-surface types that arise due to transitions through extrema and saddle points, and in Sec. 4.3.2 we discuss EFM-surface types that arise due to the cubic tangency. Finally, Sec. 4.5 shows how the EFM-surface bifurcation diagram in the (Δ_1, Δ_2)-plane changes with the filter width Λ.

Throughout this section we make use of the fact that the EFM-surface can be represented by its projection onto the (ω_s, dC_p)-plane. This is the case because, due to (3.10), this surface consists of two sheets in (ω_s, dC_p, N)-space over the (ω_s, dC_p)-plane, except at the boundary of its projection. The boundary itself is given by (real-valued) solutions of

$$\begin{aligned} dC_p = \pm \cos^{-1} \Bigg[& \frac{\sqrt{\Lambda_1^2 + (\omega_s - \Delta_1)^2}\sqrt{\Lambda_2^2 + (\omega_s - \Delta_2)^2}}{2\kappa_1\kappa_2\Lambda_1\Lambda_2} \\ & \times \left(\frac{\omega_s^2}{(1+\alpha^2)} - \frac{\kappa_1^2\,\Lambda_1^2}{\Lambda_1^2 + (\omega_s - \Delta_1)^2} - \frac{\kappa_2^2\,\Lambda_2^2}{\Lambda_2^2 + (\omega_s - \Delta_2)^2} \right) \Bigg] \\ & - \omega_s\, d\tau - \tan^{-1}\left(\frac{\omega_s - \Delta_2}{\Lambda_2}\right) + \tan^{-1}\left(\frac{\omega_s - \Delta_1}{\Lambda_1}\right). \end{aligned} \tag{4.1}$$

This equation is derived from (3.9), and it has the advantage that it does not depend on any of the state variables of (2.1)–(2.4). Hence, in contrast to computing the EFM-surface itself, which requires the continuation of EFMs in parameters, its projection onto the (ω_s, dC_p)-plane can be computed directly from (4.1). Note also that the projection in the (ω_s, dC_p)-plane is independent of the choice of the additional state variable (here N_s) that one chooses for visualisation of the EFM-surface.

4.1. Dependence of the EFM-components for fixed $dC_p = 0$ on the detunings. We now fixed $dC_p = 0$ and consider the detunings Δ_1 and Δ_2 as free parameters. We first consider an intermediate fixed filter width $\Lambda = \Lambda_1 = \Lambda_2 = 0.015$ of both filters; moreover, $\tau_1 = \tau_2 = 500$ and the other parameters are as given in Table 1. In this situation, one may find one, two or three EFM-components in the FOF laser. Because both the top and the bottom part of the envelope given by (3.9) intersect the diagonal, the EFM-component around a solitary laser frequency $\omega_s = 0$

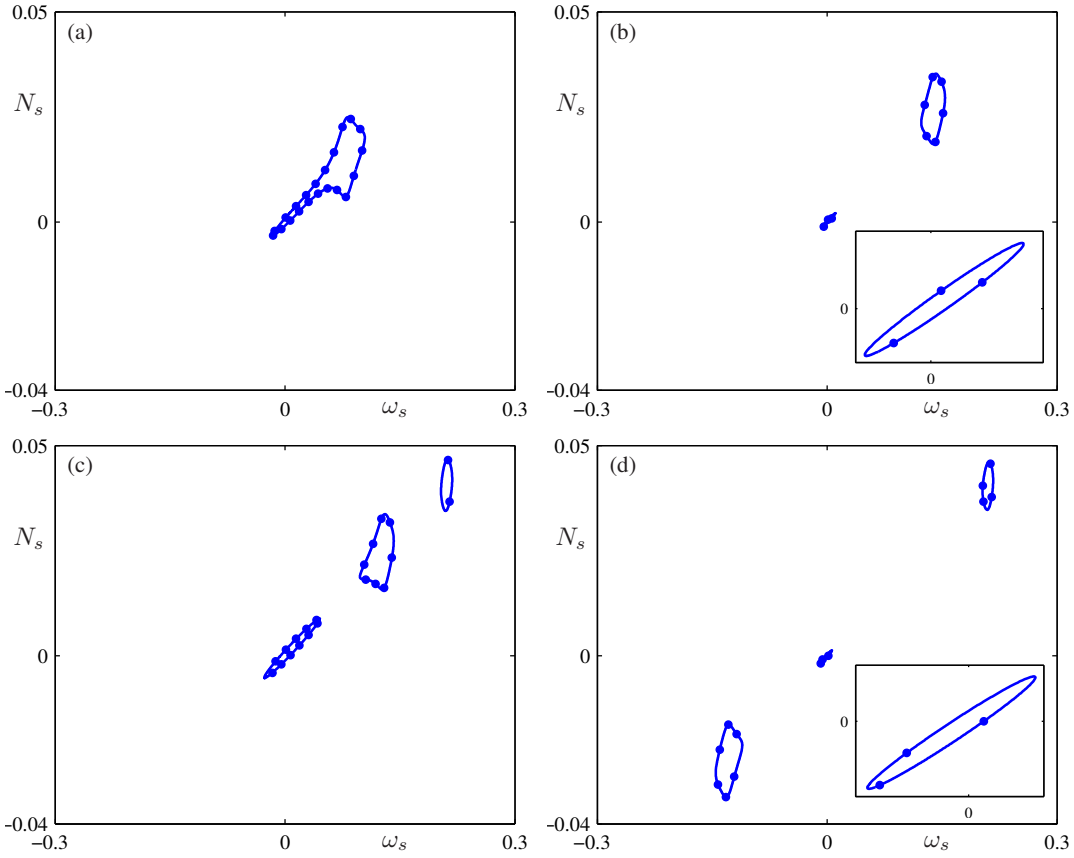

FIG. 5. *EFM-components and EFMs (blue dots) of the 2FOF laser for* $dC_p = 0$, $\Delta_1 = 0.08$, $\Delta_2 = -0.027$ *(a),* $\Delta_1 = 0.14$, $\Delta_2 = -0.027$ *(b),* $\Delta_1 = 0.21$, $\Delta_2 = 0.013$ *(c) and* $\Delta_1 = 0.21$, $\Delta_2 = -0.13$ *(d); here* $\kappa = 0.05$, $\Lambda_1 = \Lambda_2 = 0.01$, $\tau_1 = \tau_2 = 500$ *and the other parameters are as given in Table 1.*

is always present; this also means that there is a pair of saddle-node bifurcation points where EFMs are born or lost. In the presence of the two filters, one may find additional EFM-components, which exist around the peak frequencies of the filters as given by Δ_1 and Δ_2; note that (3.9) has two obvious extrema for $\omega_s = \Delta_1$ and $\omega_s = \Delta_2$. Each additional EFM-component comes with its own pair of saddle-node bifurcation points, given geometrically by the condition that an extremum of (3.9) intersects the diagonal $\omega_s = \Omega(\omega_s)$; see Fig. 3.

Figure 5 shows EFM-components for nonzero detunings and fixed $dC_p = 0$; more specifically, $\Delta_1 = 0.08$, $\Delta_2 = -0.027$ (a), $\Delta_1 = 0.14$, $\Delta_2 = -0.027$ (b), $\Delta_1 = 0.21$, $\Delta_2 = 0.013$ (c) and $\Delta_1 = 0.21$, $\Delta_2 = -0.13$ (d). In panels (a) and (b) the frequency of the second filter is detuned so much from the solitary laser frequency that the influence of the second filter is negligible and one observes only up to two EFM-components, as for a single-FOF laser. In Fig. 5 (c) and (d) we fix $\Delta_1 = 0.21$, and change Δ_2 from $\Delta_2 = 0.13$ (c) to $\Delta_2 = -0.13$ (d). In both panels there are three EFM-components. The central one near $\omega_s = 0$, as well as one around the peak frequency of each filter. Observe that the change of location of the EFM-component around the peak frequency of the second filter almost does not affect the EFM-component around the first filter peak frequency $\Delta_1 = 0.21$.

Note that the filters are quite narrow ($\Lambda_1 = \Lambda_2 = 0.01$), namely much narrower than the

detunings Δ_1 and Δ_1 between the laser and the filters. As a result, in Fig. 5 (b), (c) and (d) the EFM-component around the solitary laser frequency has an elliptical shape, as known from COF systems [64, 46]. This is the case because the flanks of both filters' transmittance profile near $\omega_s = 0$ are quite flat, meaning that all frequencies around the solitary laser frequency are fed back with approximately the same low feedback strength. Therefore, this situation resembles the effect of weak COF [46]. In Fig. 5 (a) for $\Delta_1 = 0.08$ and $\Delta_2 = -0.027$, on the other hand, the EFM-component around the solitary laser frequency has a 'bulge' which is the result of the frequency selective feedback from the first filter.

For a fixed value of the spectral width $\Lambda = \Lambda_1 = \Lambda_2$ of both filters, one obtains curves in the (Δ_1, Δ_2)-plane that bound regions where the 2FOF laser system has one, two or three EFM-components for $dC_p = 0$. The regions are bounded by curves that can be computed by means of numerical continuation. Namely, the number of EFM-components changes when two saddle-node points (black dots in Fig. 3) come together. This happens when the envelope given by $\Omega_e(\omega_s)$ from (3.9) is tangent to the diagonal. Hence, the conditions that are continued in Δ_1 and Δ_2 to obtain the boundary curves are,

$$\Omega(\omega_s) = \omega_s \quad \text{and} \quad \frac{d\Omega_e(\omega_s)}{d\omega_s} = 1.$$

Figure 6 shows these boundary curves in the (Δ_1, Δ_2)-plane for six different values of Λ. Open regions are labelled with the number of EFM-components that one finds for $dC_p = 0$ for the respective values of the detunings Δ_1 and Δ_2. Note the two symmetries of the panels of Fig. 6, given by reflection across the diagonal $\Delta_1 = \Delta_2$, and reflection across the anti-diagonal $\Delta_1 = -\Delta_2$. The boundary curves are coloured grey and orange for presentation purposes, depending on whether they are symmetric with respect to the diagonal or antidiagonal. Figure 6 (a) shows the limiting special case of $\Lambda = 0$, which corresponds to an infinitely narrow filter so that EFM-components consist of single EFMs. The boundary curves in the (Δ_1, Δ_2)-plane for this case can be obtained analytically by substituting in Eq. (3.9) $\omega_s = \Delta_1$ and $\omega_s = \Delta_2$ respectively. The coordinates of the vertical and horizontal lines in Fig. 6 (a) are given by $\kappa\sqrt{1+\alpha^2}$ and the end points at the diagonal by $2\kappa\sqrt{1+\alpha^2}$; compare with [28]. Figure 6 (b) for $\Lambda = 0.001$ shows how the limiting case unfolds for $\Lambda > 0$. The black parts of curves in Fig. 6 (a) open up to reveal new open regions. As Λ is increased, the boundary curves deform, but initially there is no qualitative change; see Fig. 6 (c) for $\Lambda = 0.01$. However, as Λ is increased further, the bifurcation diagram does change qualitatively because the different curves move sufficiently relative to one another to 'disentangle'; see Fig. 6 (d) for $\Lambda = 0.06$, where there are now no longer regions with three EFM-components near the diagonal. For larger values of Λ, the curves cease to extend to infinity and are now confined to a compact region of the (Δ_1, Δ_2)-plane; as Fig. 6 (e) for $\Lambda = 0.12$ illustrates. This implies that there is now a single large and connected region with one EFM-component. For even larger values of Λ, there are six non-overlapping curves, each bounding a small region where one finds two EFM-components; see Fig. 6 (f) for $\Lambda = 0.14$. When Λ is increased even further, the small regions disappear and one finds a single EFM-component for any point in the (Δ_1, Δ_2)-plane. Physically the filters are now so wide that they do not provide sufficient differentiation of the feedback light in frequency; hence, the 2FOF laser is effectively a COF laser.

Figure 7 (a) is a three-dimensional plot in $(\Delta_1, \Delta_2, \Lambda)$-space that represents the entire transition of the boundary curves in the (Δ_1, Δ_2)-plane for $dC_p = 0$ as the filter spectral width Λ is changed. Shown are surfaces (coloured orange and grey as in Fig. 6) that divide this parameter space into regions with one, two or three EFM-components. The bifurcation diagrams in Fig. 6 are horizontal cross sections through Fig. 7 (a); the shown (semitransparent) cross section for $\Lambda = 0.01$ yields Fig. 6 (c). Note that the grey surfaces in Fig. 7 (a) extend to higher values of Δ than the orange surfaces, which can be explained as follows. For $dC_p = 0$ the two filter fields interfere constructively,

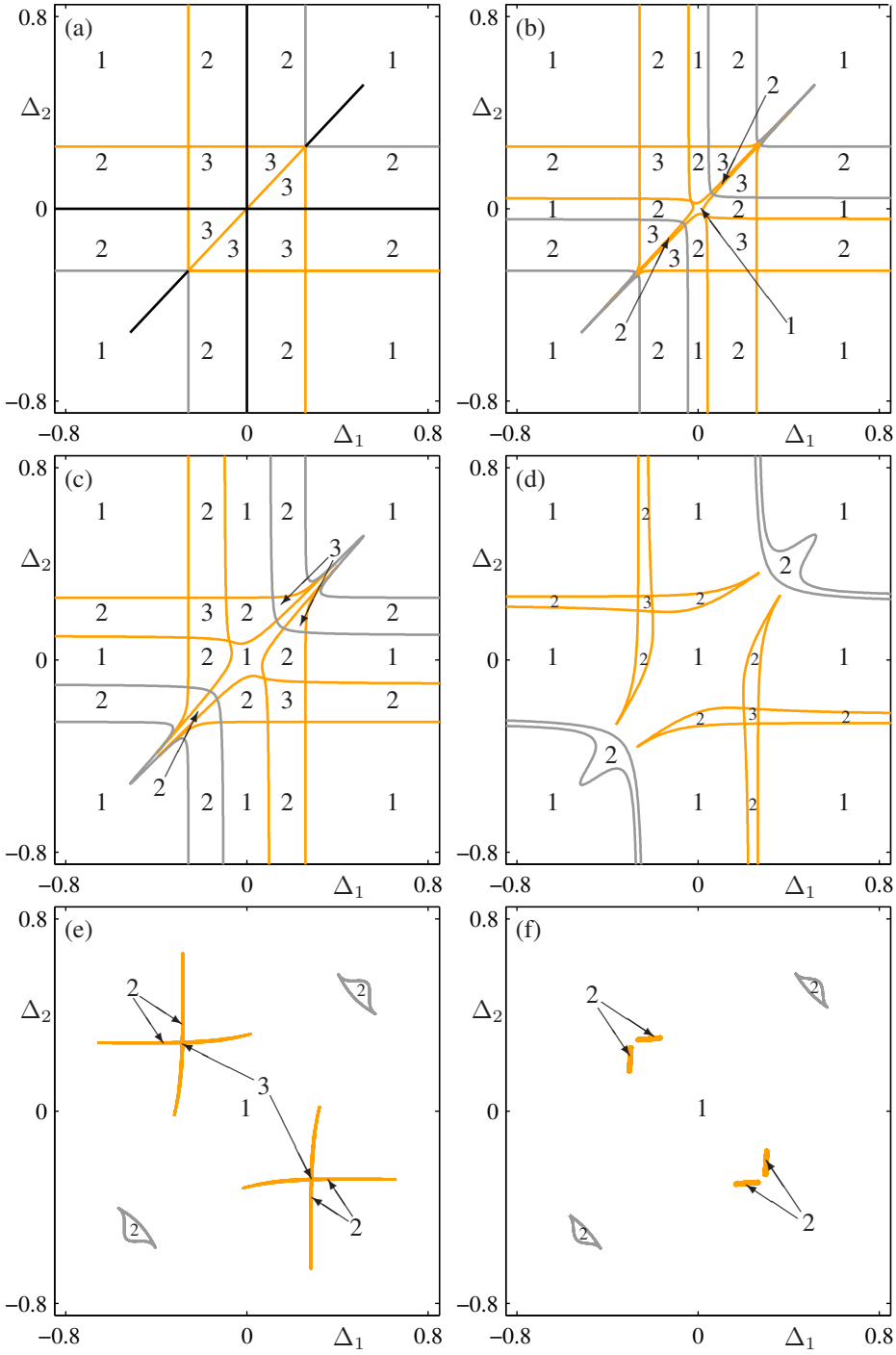

FIG. 6. *Regions in the* (Δ_1, Δ_2)*-plane with a one, two or three EFM-components of the 2FOF laser for* $dC_p = 0$. *From (a) to (f)* Λ *takes the values* $\Lambda = 0$, $\Lambda = 0.001$, $\Lambda = 0.01$, $\Lambda = 0.06$, $\Lambda = 0.12$ *and* $\Lambda = 0.14$.

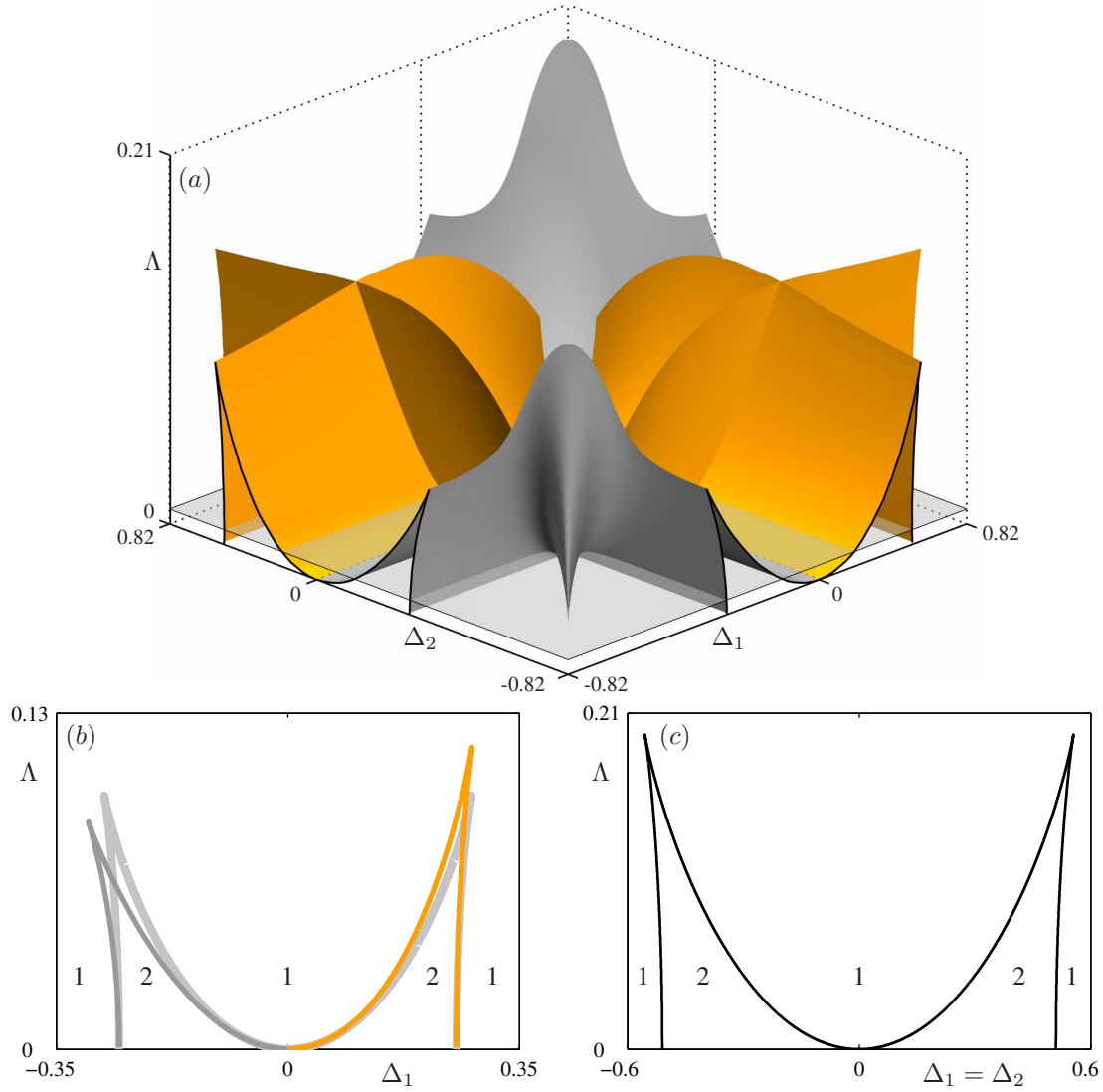

FIG. 7. *Panel (a) shows surfaces (orange and grey) that divide the* $(\Delta_1, \Delta_2, \Lambda)$*-space into regions with one, two and three EFM-components of the 2FOF laser for* $dC_p = 0$*; in the shown (semitransparent) horizontal cross section for* $\Lambda = 0.01$ *one finds the bifurcation diagram from Fig. 6 (c) . Panel (b) shows the bifurcation diagram in the* (Δ_1, Λ)*-plane for fixed* $\Delta_2 = 0.82$*; the light grey curve is the boundary curve for the limiting single-FOF laser for* $\Delta_2 = \infty$*. Panel (c) shows the projection onto the* (Δ_1, Λ)*-plane of the section along the diagonal* $\Delta_1 = \Delta_2$ *through the surfaces in panel (a).*

so that for $\Delta_1 \approx \Delta_2$ the amplitude of the solution curve of (3.3) is larger than that around a single filter. Hence, a second EFM-component around the peak frequencies of both filters may exist for higher values of Λ, and the maximum of the grey surfaces is exactly at the diagonal where $\Delta_1 = \Delta_2$. Above all surfaces (for sufficiently large Λ) the 2FOF laser is effectively a COF laser and only one EFM-component exists for any choice of Δ_1 and Δ_2.

Figures 7 (b) and (c) show that the three-dimensional bifurcation diagram in panel (a) brings out important special cases where the 2FOF laser reduces to the single-FOF laser in a nontrivial way. Figure 7 (b) shows the two-dimensional bifurcation diagram in the (Δ_1, Λ)-plane for $\Delta_2 = 0.82$.

name	C_{min}	C_{max}	panel	Δ_1	Δ_2	Λ
$\widehat{B}$	1	1	Fig. 9 (a)	0.080	-0.270	0.01
$\widehat{B}B$	2	2	Fig. 9 (b)	0.140	-0.270	0.01
$\widehat{B}BB$	3	3	Fig. 9 (c)	0.210	0.130	0.01
$B\widehat{B}B$	3	3	Fig. 9 (d)	0.210	-0.130	0.01

TABLE 2

Notation and parameter values for the types of EFM-surface in Fig. 9. The second and third column show the minimal number $C_{\min}$ and the maximal number $C_{\max}$ of EFM-components (for suitable fixed dC_p) of the type; note that in all cases the number of EFM-components is independent of dC^p .

Also shown in light grey is the corresponding bifurcation diagram of the single-FOF laser (with detuning Δ_1) that one obtains for the limit that $\Delta_2 = \infty$ (when the second filter does not influence the system any more); compare with [28, Fig. 3(a)]. The closeness of the two bifurcation diagrams in Fig. 7 (b) shows that for $\Delta_2 \geq 0.82$ the influence of the second filter is already so small that it does not influence the number of EFM-components. Figure 7 (c) shows the projection onto the (Δ_1, Λ)-plane of the diagonal section for $\Delta_1 = \Delta_2$ through the surfaces in Fig. 7 (a). Along the diagonal the 2FOF laser reduces to the single-FOF laser with the effective parameters as given by (3.11); in fact, the boundary curve in Fig. 7 (c) is exactly that from [28, Fig. 3(a)] for the corresponding effective parameters, namely $\kappa^{\text{eff}} = 2\kappa_1$ for $dC_p = 0$. Since this curve scales linearly with κ [28], it is exactly twice the size as the light grey curve in Fig. 7 (b).

4.2. EFM-surface types with dC_p-independent number of EFM-components. We now turn to the question of where in the (Δ_1, Δ_2)-plane the corresponding EFM-surface is such that it has a dC_p-independent number of EFM-components. To investigate this question, we consider how the bifurcation diagram in Fig. 6 (c), for the representative value of $\Lambda = 0.01$, with regions of one, two or three EFM-components in the (Δ_1, Δ_2)-plane for a fixed $dC_p = 0$ changes when dC_p is varied over the interval $[-\pi, \pi]$. In the process the boundary curves between regions move in the (Δ_1, Δ_2)-plane and then return to their original positions. Figure 8 shows the resulting curves (again in orange and grey) in the (Δ_1, Δ_2)-plane for $\Lambda = 0.01$, where the dC_p-interval $[-\pi, \pi]$ is covered in 60 equidistant steps. As a function of dC_p the curves now cover overlapping (orange and grey) regions in the (Δ_1, Δ_2)-plane, meaning that in these regions the number of EFM-components depends on the value of dC_p.

By contrast, in the open white regions in the (Δ_1, Δ_2)-plane of Fig. 8 the number of EFM is independent of the value of dC_p. This means that the projection of the EFM-surface consists of either one, two or three bands that extend over the entire dC_p-interval $[-\pi, \pi]$. In total there are four such types (up to symmetry) of EFM-surface, and their representatives in terms of projections of the EFM-surface onto the (ω_s, dC_p)-plane are shown in Fig. 9; for the respective values of Δ_1 and Δ_2 see Table 2. Each such band in the projection is represented in Figs. 8 and 9 by the letter B. Furthermore, $\widehat{B}$ denotes the band around the frequency of the solitary laser, $\omega_s = 0$, and is referred to as the central band. It plays a special role because it corresponds to a part of the EFM-surface that always extends over the entire dC_p-interval $[-\pi, \pi]$. Moreover, $\widehat{B}$ can be found for any value of detuning of the two filters, even in the COF limit of an infinitely wide filter; see the discussion of Fig. 7 (a) in Sec. 4.1.

The notation we use here is more specific than simply counting the number of EFM-components; for example, it distinguishes the case $B\widehat{B}B$, where the filters are detuned to both sides of the laser frequency $\omega_s = 0$, from the cases $\widehat{B}BB$ and $BB\widehat{B}$ (which are related by symmetry), where both filters are detuned on the same side of the laser frequency. Note also that type $\widehat{B}B$ differs physically

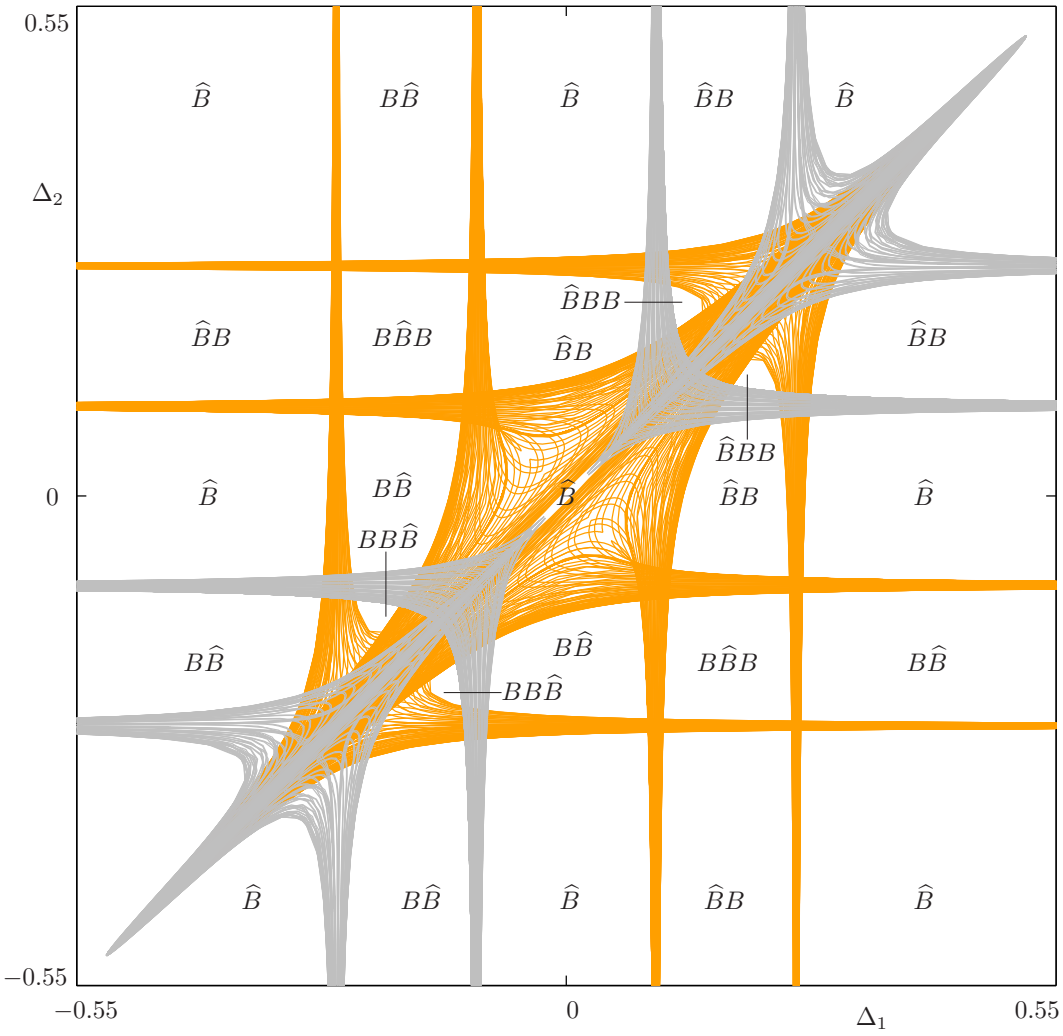

FIG. 8. *Boundary curves (orange or grey) in the* (Δ_1, Δ_2)*-plane for* $\Lambda = 0.01$ *for 60 equidistant values of* dC_p *from the interval* $[-\pi, \pi]$*; compare with Fig. 6 (c). In the white regions the 2FOF laser has one, two or three EFM-components independently of the value of* dC_p*, as is indicated by the labelling with symbols* $\widehat{B}$ *and* B*; representatives of the four types of EFM-components can be found in Fig. 9.*

from type $B\widehat{B}$ in terms of whether the second band B is towards higher or lower frequencies with respect to the laser frequency (that is, for negative or positive ω). Nevertheless, these two types are related to each other mathematically, because they are each other's images under the symmetry transformation $(\Delta_1, \Delta_2) \mapsto (-\Delta_1, -\Delta_2)$. Indeed any type that is not symmetric itself comes as a symmetric pair, and it is sufficient to show only one type of such a pair in Fig. 9.

4.3. Transitions of the EFM-surface. Consider a path in the (Δ_1, Δ_2)-plane that takes one from a white region to another white region, where the number EFM-components does not depend on the value of dC_p. It is clear from Fig. 8 that any such path necessarily leads through (at least one) (grey or orange) region where the EFM-surface is such that the number of EFM-

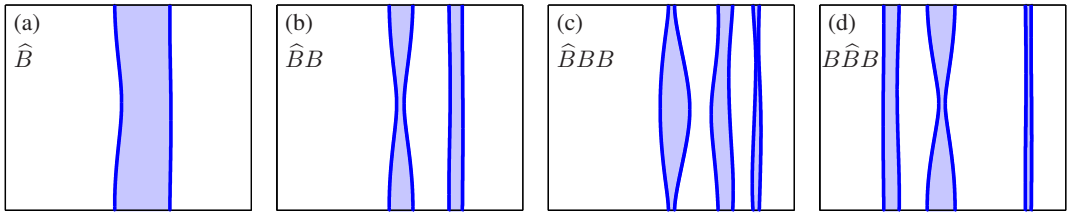

FIG. 9. *The four simple banded types of EFM-surface of the 2FOF laser in the labelled regions of Fig. 8, represented by the projection (shaded) onto the* (ω_s, dC_p)*-plane; the blue boundary curves are found directly from* (4.1). *For notation and the corresponding values of* Δ_1 *and* Δ_2 *see Table 2; in all panels* $\omega_s \in [-0.3, 0.3]$ *and* $dC_p \in [-\pi, \pi]$. *Examples of corresponding EFM-components for* $dC_p = 0$ *are presented in Fig. 5.*

components does actually depend on the value of dC_p. For example, a single band $\widehat{B}$ may change into two bands $\widehat{B}B$, and the question arises what changes of the EFM-surface itself are involved in this transition.

The point of view we take here is that the classification of the EFM-surface into different types is generated by five (local) transitions of codimension one, which we introduce in Sec. 4.3.1 below. Each such transition changes the nature of the associated EFM-components one encounters when dC_p is changed over $[-\pi, \pi]$. More specifically, we find four generic singularity transitions that change the EFM-surface topologically as a surface in three-dimensional space; as a result, the number of EFM-components changes locally. Furthermore, we consider a cubic tangency of the EFM-surface with respect to a plane $dC_p = const$, which also changes the number of EFM-components locally. These five transitions generate what we refer to as the EFM-surface bifurcation diagram in the (Δ_1, Δ_2)-plane, whose open regions correspond to different EFM-surface types with a dC_p-dependent number of EFM-components; they are introduced in Secs. 4.4 and 4.5.

The classification of the EFM-surface as generated by the five transitions considered here strikes a good balance between mathematical detail and physical relevance. On the one hand, the analysis of possible changes in the EFM-surface with dependence on parameters is complete with regard to the five different singularity transitions and their interactions. On the other hand, the five transitions considered are physically relevant in the sense that they distinguish between EFM-surface types that could be identified experimentally, for example, by mapping out the corresponding EFM-components for a sequence of different values of dC_p.

4.3.1. The four singularity transitions. The codimension-one singularity transitions are characterised by the fact that an isolated singularity of the parametrised EFM-surface is crossed at an isolated point of a curve in the (Δ_1, Δ_2)-plane. These transitions define topological changes of the EFM-surface, and will be referred to as bifurcations of of the EFM-surface. To be more specific, let δ be the bifurcation parameter that parametrises a curve in the (Δ_1, Δ_2)-plane, where we assume that the respective bifurcation curve is crossed transversely at $\delta = 0$. We can then view the EFM-surface in (ω_s, dC_p, N_s)-space locally near $\delta = 0$ as given by level sets $F(\omega_s, dC_p, N_s) = \delta$ of a function $F : \mathbb{R}^3 \to \mathbb{R}$. The singularity is then given by the condition that $\mathrm{grad}(F) = 0$; generically, the Hessian at this point is nonsingular, which means that the singularity is of codimension one [1, 26, 55]. In this case, the surface is locally quadratic and has the normal form

$$F(u, v, w) = \pm u^2 \pm v^2 \pm w^2 = \delta, \tag{4.2}$$

where the signs are given by the signs of the eigenvalues of the Hessian at the singularity. If all signs are the same then one is dealing with the transition through an extremum of the surface, that is, a minimum or a maximum; we speak of a minimax transition [41]. Otherwise, the singularity is a saddle. The unfolding of such a saddle on a two-dimensional surface is well know; see, for example,

[2]. It is the transition form a one-sheeted hyperboloid via a cone to a two-sheeted hyperboloid; we speak of a saddle transition [41]. Different cases in our context arise depending on how the cone associated with the saddle point is aligned in $(\omega_s,\, dC_p, N_s)$-space.

There are four distinct singularity transition of the EFM-surface in $(\omega_s,\, dC_p, N_s)$-space.

- M the minimax transition through an extremum (a local minimum or maximum). The minimax transition M of the EFM-surface is illustrated in Fig. 10, where, in terms of the projection onto the $(\omega_s,\, dC_p)$-plane, it results in the creation or disappearance of an island. The locus of M in the $(\Delta_1,\, \Delta_2)$-plane is represented by orange curves in what follows.

- S_C the saddle transitions in the direction of the dC_p-axis. The saddle transition S_C of the EFM-surface is illustrated in Fig. 11, where, in terms of the projection onto the $(\omega_s,\, dC_p)$-plane, it results in a transition between an island and a band. The locus of S_C in the $(\Delta_1,\, \Delta_2)$-plane is represented by blue curves in what follows.

- S_ω the saddle transitions in the direction of the ω_s-axis. The saddle transition S_ω of the EFM-surface is illustrated in Fig. 12, where, in terms of the projection onto the $(\omega_s,\, dC_p)$-plane, it results for example, in a transition between a band with a hole and two separate bands. The locus of S_ω in the $(\Delta_1,\, \Delta_2)$-plane is represented by green curves in what follows.

- S_N the saddle transitions in the direction of the N_s-axis. The saddle transition S_N of the EFM-surface is illustrated in Fig. 13, where, in terms of the projection onto the $(\omega_s,\, dC_p)$-plane, it results in the creation or disappearance of a hole in a band. The locus of S_N in the $(\Delta_1,\, \Delta_2)$-plane is represented by red curves in what follows.

Figures 10–13 illustrate how the minimax transition M and the three saddle transitions S_C, S_ω and S_N lead to changes in the EFM-surface. In each of these figures, we show in the left column the relevant local part of the EFM-surface in $(\omega_s,\, dC_p,\, N_s)$-space before, (approximately) at and (in Figs. 11–13) after the bifurcation. The right column shows how the projection of the EFM-surface onto the $(\omega_s,\, dC_p)$-plane (shown over a dC_p-interval of 4π) changes accordingly; the local regions where the change occurs are highlighted. In Figs. 10–13 all the presented surfaces have been rendered from continuations of the EFMs as solutions of equations (2.1)–(2.4); the projections, on the other hand, were obtained directly from (4.1).

Figure 10 illustrates the minimax transition M, where a compact piece of the EFM-surface in $(\omega_s,\, dC_p,\, N_s)$-space shrinks to a point. Panel (b1) is very close to the bifurcation; note that after the bifurcation the piece is simply gone, which is why we do not present a separate illustration for this situation. In projection onto the $(\omega_s,\, dC_p)$-plane, the local, compact piece of the EFM-surface is an 'island' that shrinks and then disappears in a minimax transition of the projection; note that there are infinitely many such islands due to the translational symmetry in dC_p; see panels (a2) and (b2).

Figure 11 illustrates the saddle transition S_C. The local mechanism for this change of the EFM-surface in $(\omega_s,\, dC_p,\, N_s)$-space is shown in panels (a1)–(c1). The surface in Fig. 11 (a1) is a one-sheeted hyperboloid. It develops a pinch point and, hence, becomes a cone at the moment of bifurcation in Fig. 11 (b1); note that the cone (more precisely its axis of rotation) is aligned with the dC_p-axis. After the bifurcation, the EFM-surface is a two-sheeted hyperboloid so that it consists locally of two parts; see Fig. 11 (c1). As the projections onto the $(\omega_s,\, dC_p)$-plane in panels (a2)–(c2) show, the overall result is the division of a 'band' into a 'string of islands.' Note that the saddle transition S_C manifests itself as a saddle transition of the projection, where the relevant (shaded) part of the surface is aligned with the dC_p-axis.

Figure 12 illustrates the saddle transition S_ω. Locally near the point of bifurcation we again find that the EFM-surface in $(\omega_s,\, dC_p,\, N_s)$-space changes from a one-sheeted hyperboloid in panel (a1), via a cone in panel (b1) to a two-sheeted hyperboloid in panel (c1). However, now the cone's

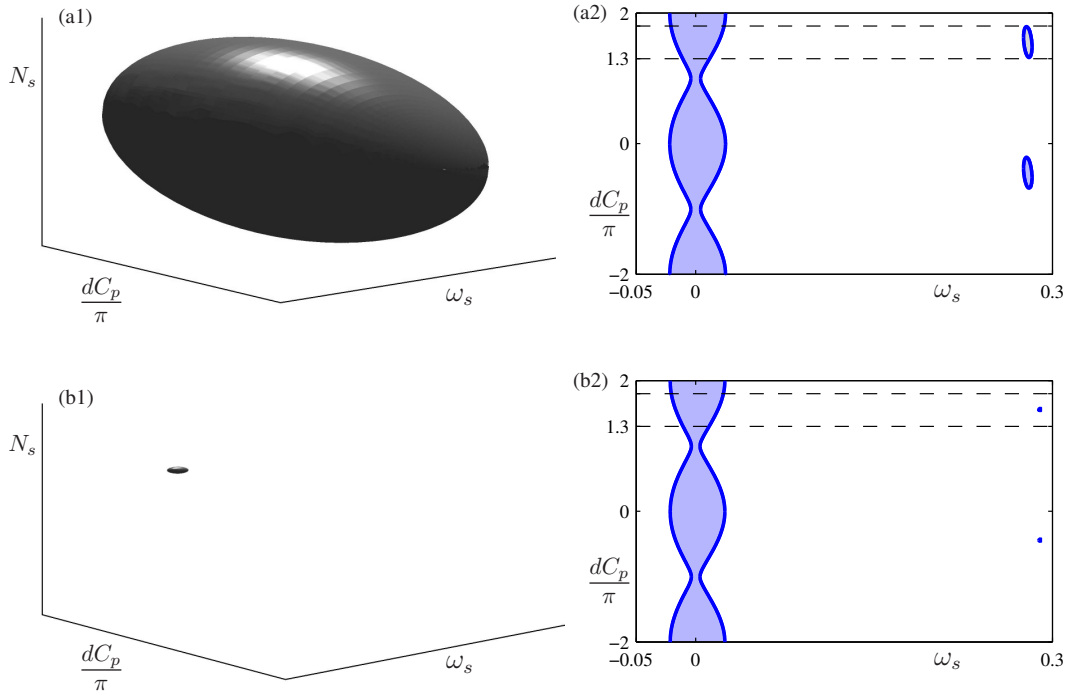

FIG. 10. *Minimax transition M of the EFM-surface in (ω_s, dC_p, N_s)-space, where a connected component of the EFM-surface (a1) shrinks to a point (b1). Panels (a2) and (b2) show the corresponding projection onto the (ω_s, dC_p)-plane of the entire EFM-surface; the local region where the transition M occurs is highlighted by dashed lines and the projections of the part of the EFM-surface in panels (a1) and (b1) is shaded grey. Here $\Lambda = 0.01$, $\Delta_1 = 0.4$, and $\Delta_2 = 0.28$ in (a) and $\Delta_2 = 0.28943$ in (b).*

axis of rotation is aligned with the ω_s-axis. As the projections onto the (ω_s, dC_p)-plane in panels (a2)–(c2) show, overall we find that a single band with a 'string of holes' changes into two separate bands. The saddle transition S_ω also manifests itself as a saddle transition of the projection.

Figure 13 illustrates the saddle transition S_N. In panel (a1) there are two sheets of the EFM-surface in (ω_s, dC_p, N_s)-space with different and separate values of N_s. At the bifurcation point the two sheets connect locally at a single point. In the process, a 'hole' is created in the EFM-surface, which then grows in size; see panels (b1) and (c1). If one considers a small neighbourhood of the emerging hole, then one realises that the transition is locally that from a two-sheeted hyperboloid in panel (a1), via a cone aligned along the N_s-axis in panel (b1) to a one-sheeted hyperboloid in panel (c1). The projections onto the (ω_s, dC_p)-plane in panels (a2)–(c2) clearly show how a string of holes appears in the saddle transition S_N. Note that this bifurcation is a minimax transition of the projection but, in contrast to transition M, the projection of the surface is now 'on the outside' so that locally a hole is created instead of an island.

It is an important realisation that the loci of the four singularity transitions M, S_C, S_ω and S_N can be computed effectively, because they can be expressed as an implicit formula by considering a suitable derivative of the envelope equation (3.9) with respect to the parameter in question. More specifically, one follows a fold with respect to dC_p of the boundary curve of the projection of the EFM-surface onto the (ω_s, dC_p)-plane. Such a dC_p-fold bounds an interval of dC_p-values, which is either an island or a hole of the projection. When the dC_p-fold is continued along a

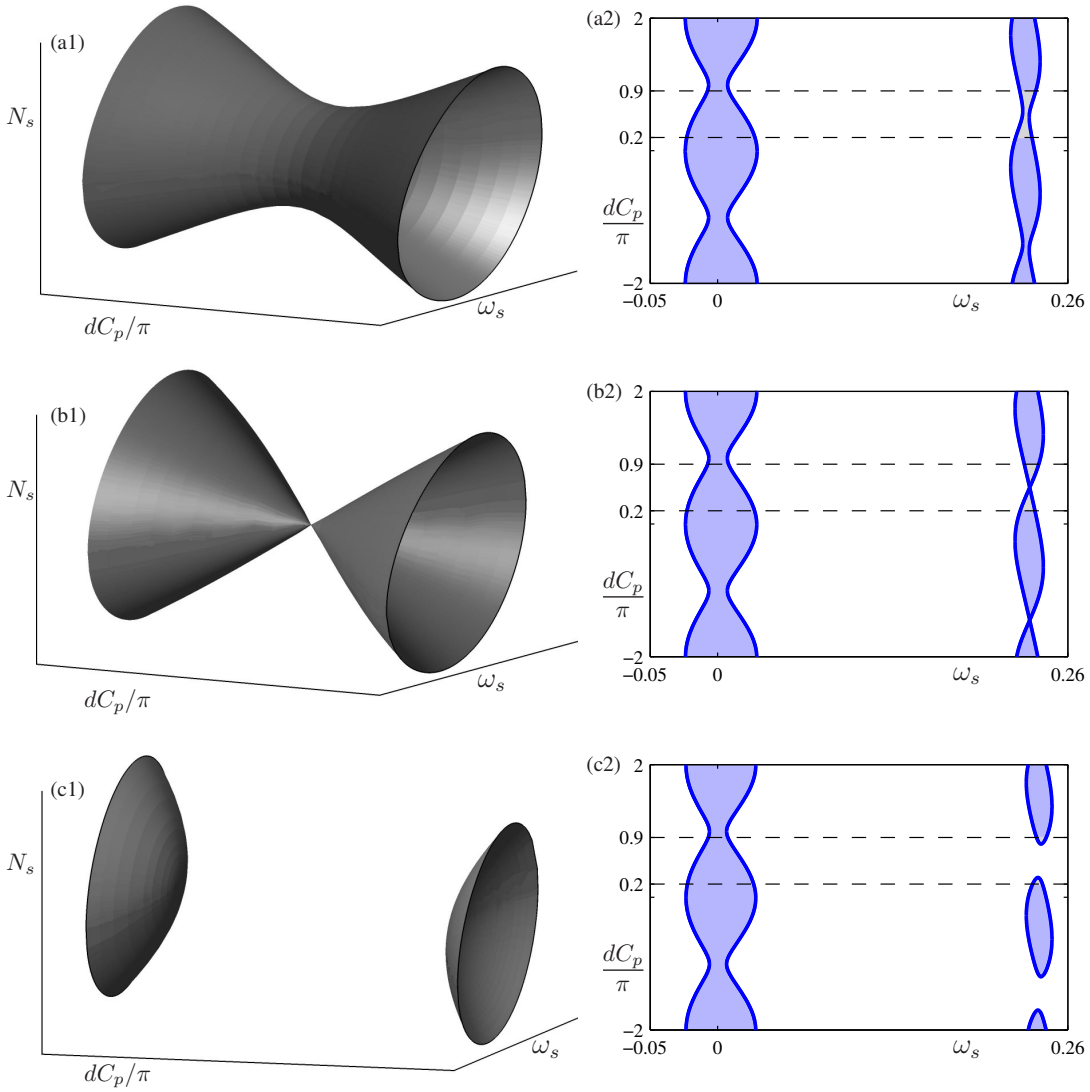

FIG. 11. *Saddle transition S_C of the EFM-surface in (ω_s, dC_p, N_s)-space, where locally the surface changes from a one-sheeted hyperboloid (a1) to a cone aligned in the dC_p-direction (b1) to a two-sheeted hyperboloid (c1). Panels (a2)–(c2) show the corresponding projection onto the (ω_s, dC_p)-plane of the entire EFM-surface; the local region where the transition S_C occurs is highlighted by dashed lines and the projections of the part of the EFM-surface in panels (a1)–(c1) is shaded grey. Here $\Lambda = 0.01$, $\Delta_1 = 0.4$, and $\Delta_2 = 0.23$ in (a), $\Delta_2 = 0.232745$ in (b) and $\Delta_2 = 0.24$ in (c).*

curve (parametrised by δ) in the (Δ_1, Δ_2)-plane, say, Δ_2 for fixed Δ_1, then a singularity transition corresponds to a fold with respect to the continuation parameter δ. Such a fold with respect to the parameter δ can be detected and then followed as a boundary curve in the (Δ_1, Δ_2)-plane. Note that this continuation approach makes no difference between the cases M, S_C, S_ω and S_N of singularity transitions. However, which of the singularity transitions one is dealing with can readily be identified by checking the (projections of the) EFM-surface at nearby parameter point in the (Δ_1, Δ_2)-plane. In this way, the loci of the singularity transitions can be computed numerically as

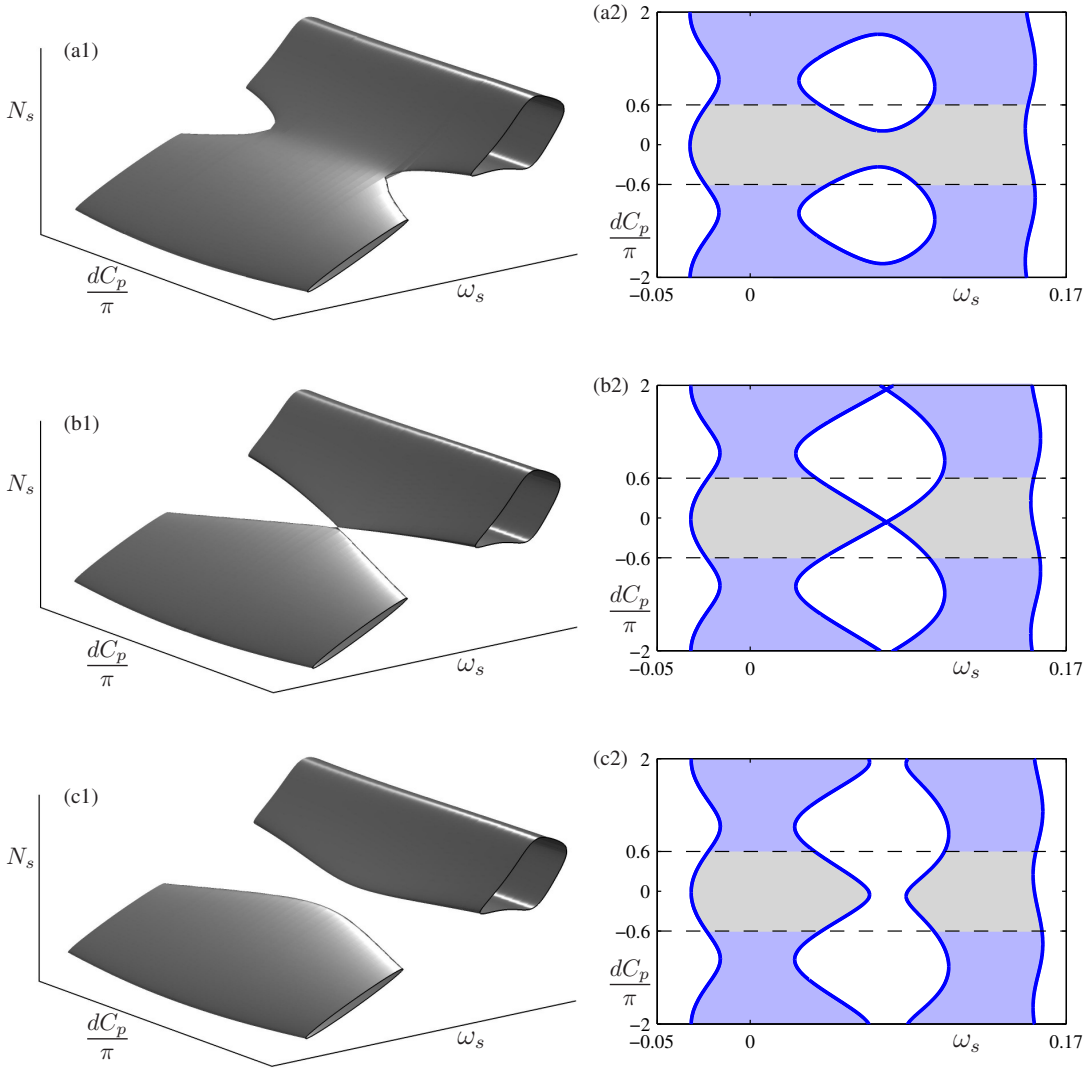

FIG. 12. *Saddle transition S_ω of the EFM-surface in (ω_s, dC_p, N_s)-space, where a connected component (a1) pinches (b1) and then locally disconnects (c1); here the associated local cone in panel (b1) is aligned in the ω_s-direction. Panels (a2)–(c2) show the corresponding projection onto the (ω_s, dC_p)-plane of the entire EFM-surface; the local region where the transition S_ω occurs is highlighted by dashed lines and the projections of the part of the EFM-surface in panels (a1)–(c1) is shaded grey. Here $\Lambda = 0.01$, $\Delta_1 = 0.4$, and $\Delta_2 = 0.13$ in (a), $\Delta_2 = 0.133535$ in (b) and $\Delta_2 = 0.135$ in (c).*

bifurcation curves in the (Δ_1, Δ_2)-plane that form boundaries between regions of different EFM-surface types.

4.3.2. The cubic tangency. Due to the special role of the parameter dC_p we also consider here a fifth local mechanism that changes the type of the EFM-surface.

$\mathcal{C}$ the cubic tangency $\mathcal{C}$ of the EFM-surface; it is defined by the condition that the first and second derivatives with respect to ω_s of equation (3.9) for the envelope of $\Omega(\omega_s)$ both vanish at an isolated point, and the third derivative is nonzero. The cubic tangency $\mathcal{C}$

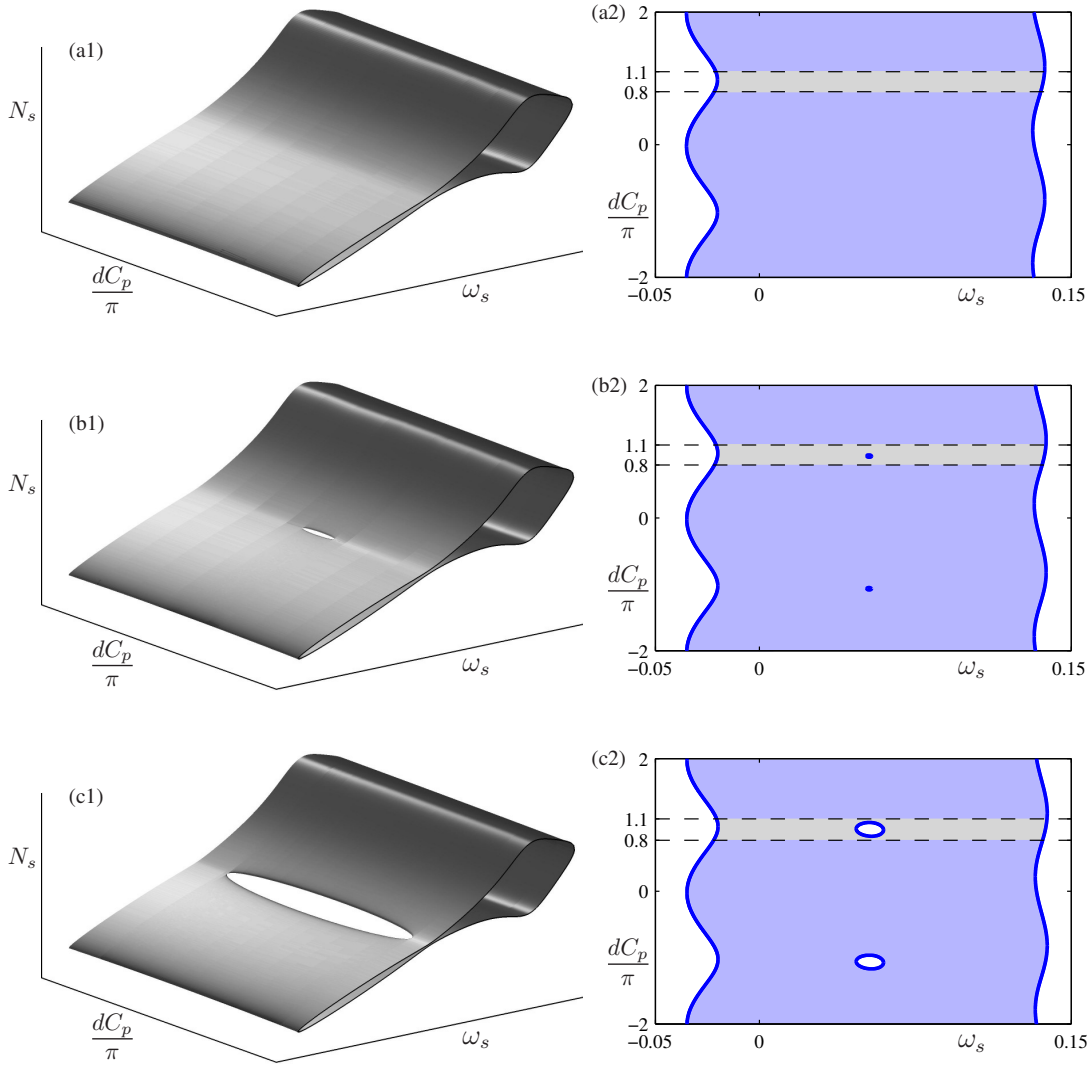

FIG. 13. *Saddle transition S_N of the EFM-surface in (ω_s, dC_p, N_s)-space, where two sheets that lie on top of each other in the N_s direction (a1) connect at a point (b1) and then create a hole in the surface (c1); here the associated local cone in panel (b1) is aligned in the N-direction. Panels (a2)–(c2) show the corresponding projection onto the (ω_s, dC_p)-plane of the entire EFM-surface; the local region where the transition S_N occurs is highlighted by dashed lines and the projections of the part of the EFM-surface in panels (a1)–(c1) is shaded grey. Here $\Lambda = 0.01$, $\Delta_1 = 0.4$, and $\Delta_2 = 0.0.11$ in (a), $\Delta_2 = 0.11085$ in (b) and $\Delta_2 = 0.1115$ in (c).*

of the EFM-surface is illustrated in Fig. 14, where, in terms of the projection onto the (ω_s, dC_p)-plane, it results in the creation of a pair of local extrema of dC_p that form a bulge of the EFM-surface. The locus of $\mathcal{C}$ in the (Δ_1, Δ_2)-plane is represented by black and grey curves in what follows.

Figure 14 illustrates the cubic tangency $\mathcal{C}$. Before the transition the EFM-surface in (ω_s, dC_p, N_s)-space is such that it does not feature dC_p-folds of the boundary curve in projection onto the (ω_s, dC_p)-plane; see panels (a1) and (a2). At the moment of transition the EFM-surface is such

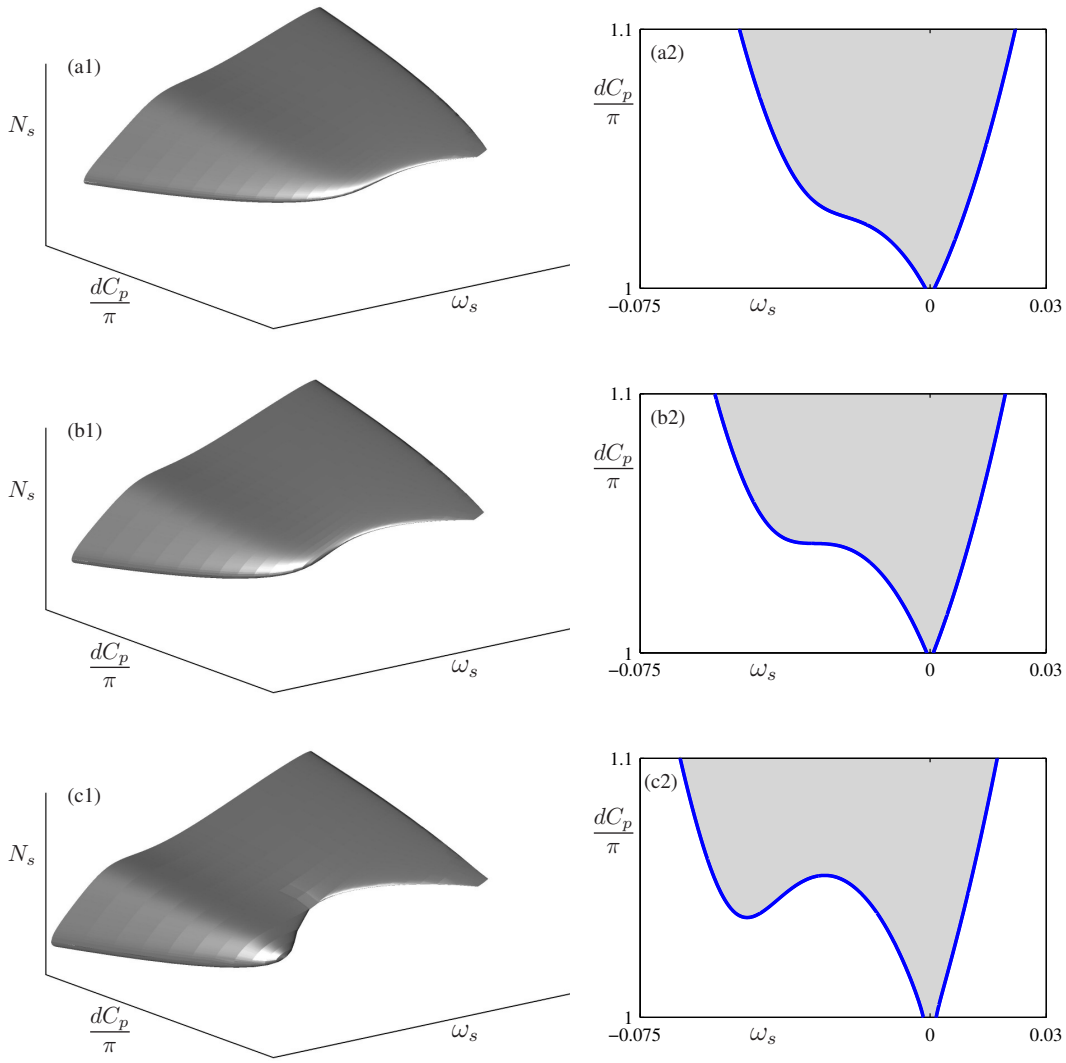

FIG. 14. *Cubic tangency $\mathcal{C}$ of the EFM-surface in (ω_s, dC_p, N_s)-space, where a part of the surface (a1) becomes tangent to a plane $\{dC_p = const\}$ (b1) and then develops a bulge (c1). The unfolding of the cubic tangency into two dC_p-folds can be seen clearly in the projections onto the (ω_s, dC_p)-plane in panels (a2)–(c2). Here $\Lambda = 0.015$, and $(\Delta_1, \Delta_2) = (-0.03, -0.0301)$ in (a), $(\Delta_1, \Delta_2) = (-0.04, -0.0401)$ in (b) and $(\Delta_1, \Delta_2) = (-0.05, -0.051)$.*

that the boundary curve of the envelope has a cubic tangency with a curve $dC_p = const$; see panels (b1) and (b2). This cubic tangency of the boundary curve unfolds into a pair of a local minimum and a local maximum of dC_p for nearby values of ω_s; see panels (c1). This pair of extrema corresponds to a 'bulge' of the EFM-surface; see panels (c1). As a result, there is now an interval of dC_p-values where one finds two distinct EFM-components. The locus $\mathcal{C}$ of cubic tangency can be computed by numerical continuation of the condition that the first two derivatives with respect to ω_s of the envelope equation (3.9) are zero.

4.4. The EFM-surface bifurcation diagram in the (Δ_1, Δ_2)-plane for fixed Λ. For a fixed value of Λ the five transitions M, S_C, S_ω, S_N and $\mathcal{C}$ of codimension one give rise to boundary curves that divide the (Δ_1, Δ_2)-plane into a finite number of regions. Each such region defines a

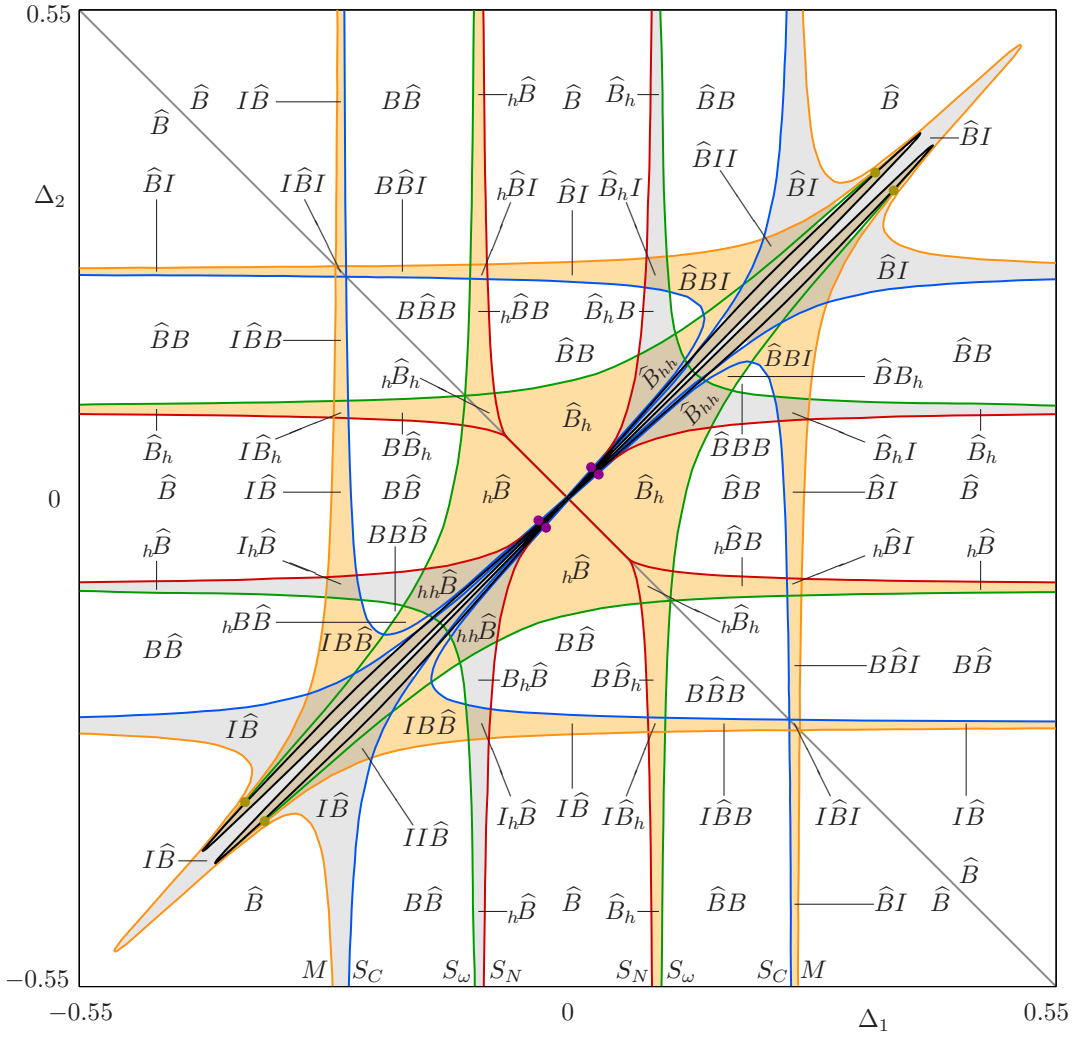

FIG. 15. *EFM-surface bifurcation diagram in the* (Δ_1, Δ_2)*-plane for* $\Lambda = 0.01$ *with regions of different types of the EFM-surface; see Fig. 16 for representatives of the labelled types of the EFM-surface and Table 3 for the notation. The main boundary curves are the singularity transitions M (orange curves),* S_C *(blue curves),* S_ω *(green curves) and* S_N *(red curves). The locus of cubic tangency (black curves) can be found near the diagonal; also shown is the anti-diagonal.*

type of the EFM-surface, and we speak of the EFM-surface bifurcation diagram in the (Δ_1, Δ_2)-plane.

We first consider in Fig. 15 the EFM-surface bifurcation diagram for the case $\Lambda = 0.01$. As in Fig. 8, the white regions correspond to the band-like types of the EFM-surface from Sec. 4.2 with a dC_p-independent number of EFM-components. In the grey and orange regions, on the other hand, one finds new EFM-surface types. In Fig. 15 we labelled those types that are associated with transitions between the band-like EFM-surface types; there are a total of 15 additional types, and their representatives are shown in Fig. 16; for notation and parameter values of the individual panels see Table 3. As before, the symbol B denotes a connected component of the EFM-surface

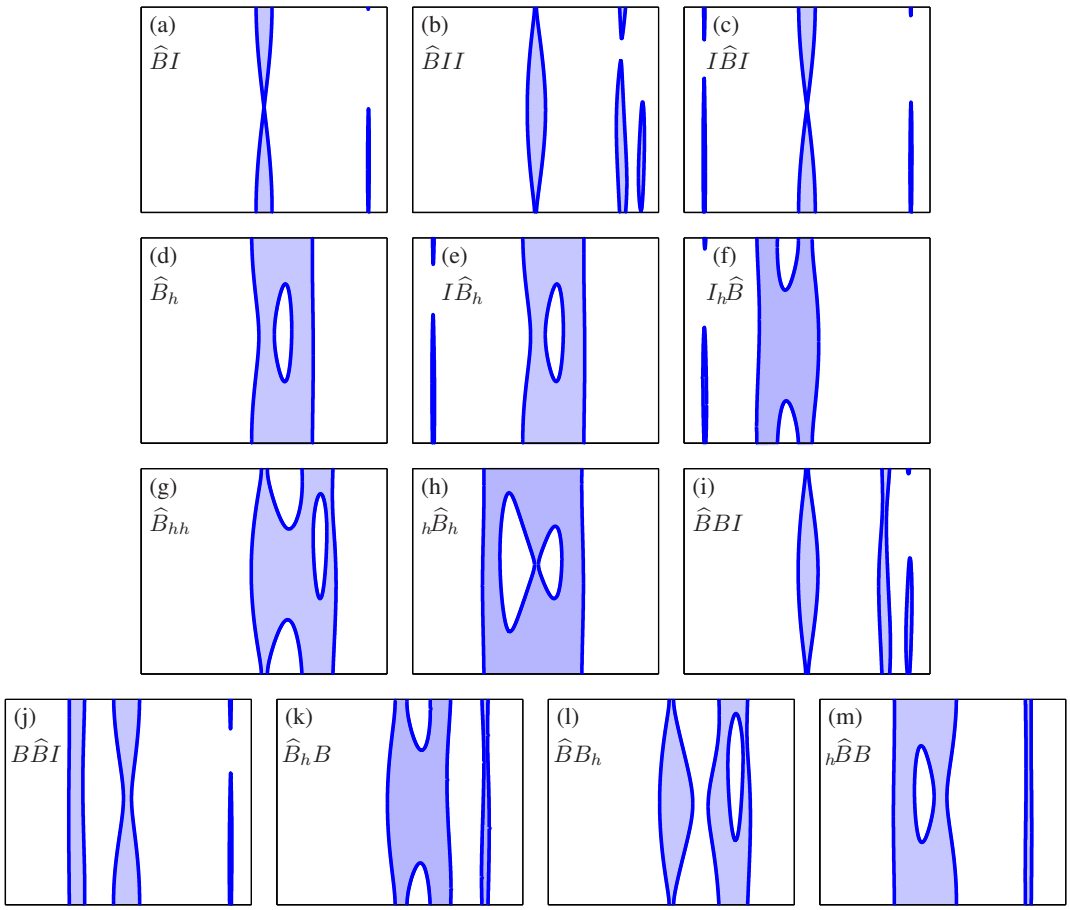

FIG. 16. *Additional types of EFM-surface of the 2FOF laser in the labelled regions of Fig. 15, represented by the projection (shaded) onto the* $(\omega_s,\, dC_p)$*-plane; the blue boundary curves are found directly from* (4.1)*. For notation and the corresponding values of* Δ_1 *and* Δ_2 *see Table 3; in all panels* $\omega_s \in [-0.3,\, 0.3]$ *and* $dC_p \in [-\pi,\, \pi]$*.*

in the form of a band in projection onto the $(\omega_s,\, dC_p)$-plane that extends over the entire C_p-range $[-\pi, \pi]$.

There are two noteworthy features of the EFM-surface types in Fig. 16. First of all, there are connected components of the EFM-surface that do not extend over the entire C_p-range $[-\pi, \pi]$; we use the symbol I to refer to them because their projection onto the $(\omega_s,\, dC_p)$-plane consists of an 'island' when $dC_p \in \mathbb{R}/2\pi\mathbb{Z}$ (infinitely many islands in the covering space when $dC_p \in \mathbb{R}$). Owing to the underlying symmetry $(\Delta_1,\, \Delta_2) \mapsto (-\Delta_1,\, -\Delta_2)$, we again represent in the notation the position of an island with respect to the central band $\widehat{B}$. As second new feature is the fact that a band may have up to two (periodically repeated) holes. Similarly to the islands, we reflect in the notation the position of a hole with respect to the laser frequency (at $\omega_s = 0$). Namely, we indicate with left and right subscripts whether a hole is to the left or to the right of $\{\omega_s = 0\}$; for example, we distinguish the case $\widehat{B}_{hh}$ from ${}_h\widehat{B}_h$. We observe that islands never have holes for any values of the parameters as considered here; this means that the symbol I does never have a subscript.

In Fig. 16 we again show only one representative for any pair that is related by symmetry. Obtaining a representative of the symmetric counterpart corresponds to a reflection of the respective

name	C_{min}	C_{max}	panel	Δ_1	Δ_2	Λ
$\widehat{B}I$	1	2	Fig. 16 (a)	0.255	-0.270	0.01
$\widehat{B}II$	1	3	Fig. 16 (b)	0.260	0.210	0.01
$I\widehat{B}I$	1	3	Fig. 16 (c)	0.254	-0.251	0.01
$\widehat{B}_h$	1	2	Fig. 16 (d)	0.100	-0.270	0.01
$I\widehat{B}_h$	1	3	Fig. 16 (e)	0.100	-0.250	0.01
$I_h\widehat{B}$	1	3	Fig. 16 (f)	-0.100	0.250	0.01
$\widehat{B}_{hh}$	1	3	Fig. 16 (g)	0.160	0.110	0.01
${}_h\widehat{B}_h$	1	3	Fig. 16 (h)	0.095	-0.110	0.01
$\widehat{B}BI$	2	3	Fig. 16 (i)	0.250	0.190	0.01
$B\widehat{B}I$	2	3	Fig. 16 (j)	0.250	-0.130	0.01
$\widehat{B}_hB$	2	3	Fig. 16 (k)	0.210	0.100	0.01
$\widehat{B}B_h$	2	3	Fig. 16 (l)	0.180	0.130	0.01
${}_h\widehat{B}B$	1	3	Fig. 16 (m)	0.210	-0.100	0.01

TABLE 3

Notation and parameter values for the types of EFM-surface in Fig. 16; the second and third column show the minimal number $C_{\min}$ and the maximal number $C_{\max}$ of EFM-components (for suitable fixed dC_p) of the type.

image in the line $\omega_s = 0$; this operation is mirrored in the notation by reversing the symbol string representing the EFM-surface type. In Fig. 15 this symmetry operation corresponds to reflection in the antidiagonal of the (Δ_1, Δ_2)-plane. Note also the symmetry of the EFM-surface bifurcation diagram given by reflection in the diagonal; it corresponds to an exchange of the two filters and, hence, does not change the EFM-surface type.

The outer part of the EFM-surface bifurcation diagram in Fig. 15, away from the diagonal, is characterised by grey and orange intersecting strips, which are each bounded by a pair of curves of singularity transitions. These strips must be crossed in the (Δ_1, Δ_2)-plane to move between different white regions of band-like types of the EFM-surface. As an example, consider a sufficiently large fixed value of one of the detunings, say, of Δ_1, while the other detuning, Δ_2, is allowed to change. The grey strip bounded by the pair of curves M and S_C is responsible for the transition from a single band $\widehat{B}$ to two bands $\widehat{B}B$ via the appearance of a string of islands that then merge into the new band B. The pair S_N and S_ω, on the other hand, also results in a transition from $\widehat{B}$ to $\widehat{B}B$, but via the appearance of a string of holes in $\widehat{B}$ that then merge to form a gap that splits off the new band B. Note that the illustrations of the singularity transitions in Figs. 10–13 are all for $\Delta_1 = 0.4$; hence, they also illustrate the transition from $\widehat{B}$ to $\widehat{B}B$ via S_N and S_ω and back to $\widehat{B}$ via S_C and M as Δ_2 is increased from, say, $\Delta_2 = 0$.

The grey and orange strips in Fig. 15 are unbounded and extend all the way to infinity. This follows from the fact that the limit $\Delta_i \to \pm\infty$ reduces to the single-FOF laser in a nontrivial way, as was discussed in Sec. 4.1. More specifically, for the chosen value of $\Lambda = 0.01$ the curve in the (Δ_1, Λ)-plane of Fig. 7 (b) is intersected four times, and this accounts for the four stripes one finds for $\Delta_2 \to \pm\infty$ (and similarly for $\Delta_1 \to \pm\infty$).

The anti-diagonal is shown in Fig. 15 because along it one finds special, degenerate cases of the EFM-surface. There are two different cases, and they are shown in Fig. 17. Along the red part of the anti-diagonal we find a degenerate saddle transition S_N. At the moment of transition the upper and lower sheets of the EFM-surface touch at a single, isolated point (and its 2π-translates in dC_p);

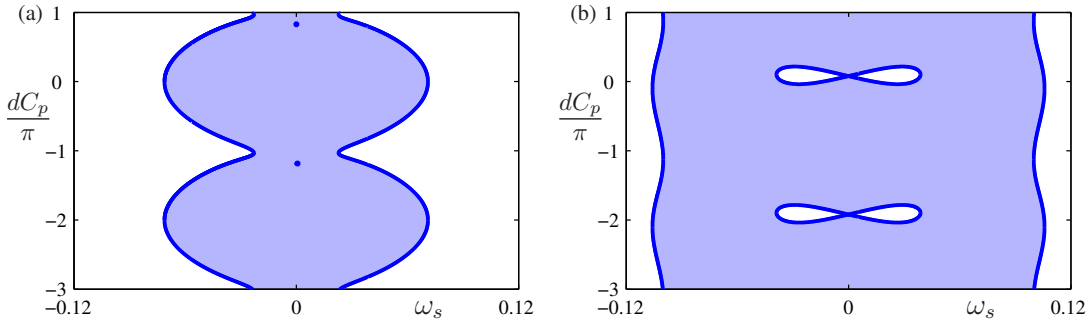

FIG. 17. *Projection of the EFM-surface onto* (ω_s, dC_p)*-plane for* $\Lambda = 0.01$. *Panel (a) is for* $\Delta_1 = -\Delta_2 = 0.003$ *and panel (b) is for* $\Delta_1 = -\Delta_2 = 0.08$.

see Fig. 17 (a). However, as Fig. 15 shows, on either side of the red part of the anti-diagonal we find the symmetrically related pair ${}_h\widehat{B}$ and $\widehat{B}_h$, which each features a hole. Hence, when the red part of the anti-diagonal is crossed, the hole shrinks and then re-appears on the other side of the line $\omega_s = 0$; physically, the hole is on the side of the filter profile that is detuned furthest from the solitary laser frequency. From a bifurcation point of view, along the red part of the anti-diagonal the EFM-surface changes locally from a two-sheeted hyperboloid to a cone and back to a two-sheeted hyperboloid, rather than to a one-sheeted hyperboloid; compare with Fig. 13 of the non-degenerate saddle transition S_N.

Along the grey part of the anti-diagonal, on the other hand, we find a degenerate saddle transition S_C. Note that the EFM-surface type on either side of this grey curve is the same and invariant under the symmetry operation $\Delta_1 \mapsto -\Delta_2$. Figure 17 (b) shows the moment of transition for the case that the anti-diagonal bounds the two regions of EFM-surface type ${}_h\widehat{B}_h$ in Fig. 15. In this transition the two holes (and their 2π-translates in dC_p) touch to form a lemniscate in Fig. 17 (b). This means that the EFM-surface is connected (locally) at isolated points with $\omega_s = 0$. We also found this degenerate type of connection of the EFM-surface at such isolated points in Fig. 4 — for the case that the surface is of type $\widehat{B}$. In effect, along the grey part of the anti-diagonal the EFM-surface changes locally from a one-sheeted hyperboloid to a cone and back to a one-sheeted hyperboloid, rather than to a two-sheeted hyperboloid; compare with Fig. 11 of the non-degenerate saddle transition S_C.

4.4.1. The locus of cubic tangency in the (Δ_1, Δ_2)**-plane.** In Fig. 15 one finds (black) curves of cubic tangency near the diagonal in the central region of the (Δ_1, Δ_2)-plane. To understand their role for the EFM-surface bifurcation diagram, we show in Fig. 18 an enlargement of the (Δ_1, Δ_2)-plane near the central (white) region where the EFM-surface is of type $\widehat{B}$. Recall that this central region must exist as a perturbation of the special case of the EFM-surface for $\Delta_1 = \Delta_2 = 0$ in Fig. 4 (a); from the physical point of view, this type of EFM-surface exists (for $\kappa \neq 0$) as the continuation of the solitary laser mode for $\kappa = 0$. Note that for $\Lambda = 0.01$, as in Figs. 15 and 18, this central region is quite small; however, as we will see in Sec. 4.5, it may grow considerable when the filter spectral width Λ is increased.

The central (white) region of EFM-surface type $\widehat{B}$ in Fig. 18 is bounded entirely by curves of cubic tangency. Therefore, as the filters are detuned away from the solitary laser frequency, the first transformation of the EFM-surface that gives rise to an additional EFM-component is a cubic tangency. We find it convenient to distinguish two different types of cubic tangency. The (black) curves $\mathcal{C}_a$ are invariant under reflection in the anti-diagonal; they correspond to cusp points of the orange curves in Figs. 6 and 8. The (grey) curves $\mathcal{C}_d$ are invariant under reflection in the

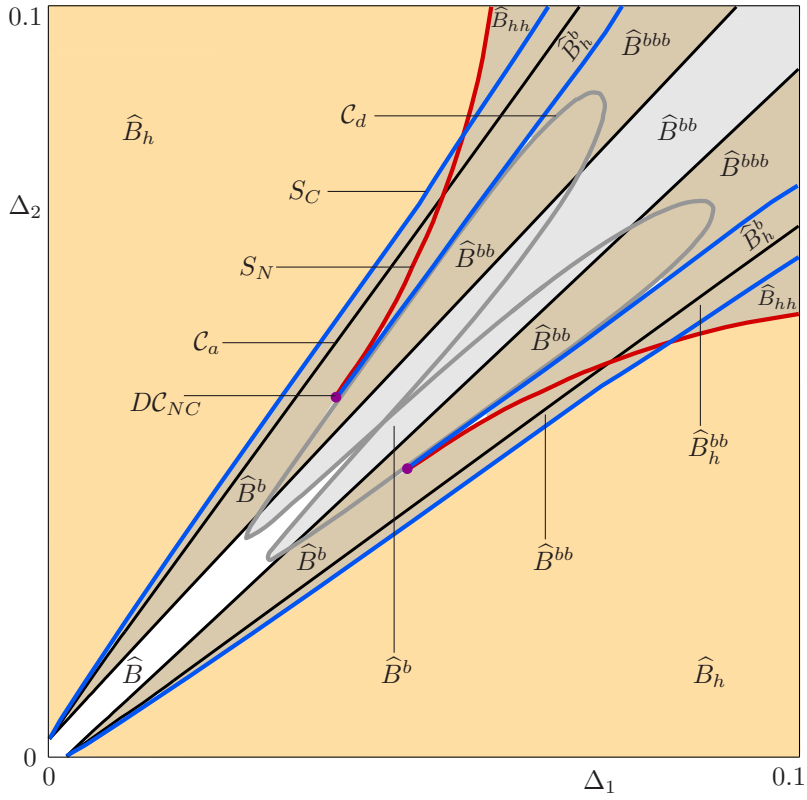

FIG. 18. *Enlargement near the center of the* (Δ_1, Δ_2)*-plane of Fig. 15 with (blue) curves of* S_C *transition, (red) curves of* S_N *transition, and (black) curves* $\mathcal{C}_a$ *and (grey) curves* $\mathcal{C}_d$ *of cubic tangency; see Fig. 19 for representatives of the labelled types of the EFM-surface and Table 4 for the notation.*

anti-diagonal; they correspond to cusp points of the grey curves in Figs. 6 and 8. The (black) cubic tangency locus $\mathcal{C}_a$ consists of two elongated and self-intersecting closed curves, one above and one below the diagonal; see Fig. 15. The (grey) cubic tangency locus $\mathcal{C}_d$ also consists of two self-intersecting closed curves, but they cross the diagonal and one lies above and the other below the anti-diagonal; see Fig. 18 and note that the locus $\mathcal{C}_d$ is too small to be visible in Fig. 15.

Crossing either of the boundary curves $\mathcal{C}_a$ and $\mathcal{C}_d$ from inside the central (white) region labelled $\widehat{B}$ in Fig. 18 results in the appearance of a bulge of the EFM-surface. We represent this in our notation of this region as $\widehat{B}^b$ by a superscript b; as before, whether the superscript appears on the left or on the right of the central band $\widehat{B}$ indicates its position with respect to the solitary laser frequency given by $\omega_s = 0$. As Fig. 18 shows, we find a complicated EFM-surface bifurcation diagram consisting of an interplay of cubic tangency curves $\mathcal{C}_a$ and $\mathcal{C}_d$ with saddle-transition curves S_C and S_N. The four sets of curves divide the (Δ_1, Δ_2)-plane into regions of additional EFM-surface types, which are all characterised by a certain number of bulges as represented in the notation. The corresponding EFM-surface types are shown in projection onto the (ω_s, dC_p)-plane in Fig. 19 (a), (b), (d), (k) and (m); for notation and parameter values of the individual panels see Table 4. Note that near the central region of the (Δ_1, Δ_2)-plane the EFM-surface is subject to the interaction of both filters near the frequency of the laser, which means that there are no other bands or islands.

Figure 18 also shows that crossing the saddle-transition curve S_C may result in the creation of

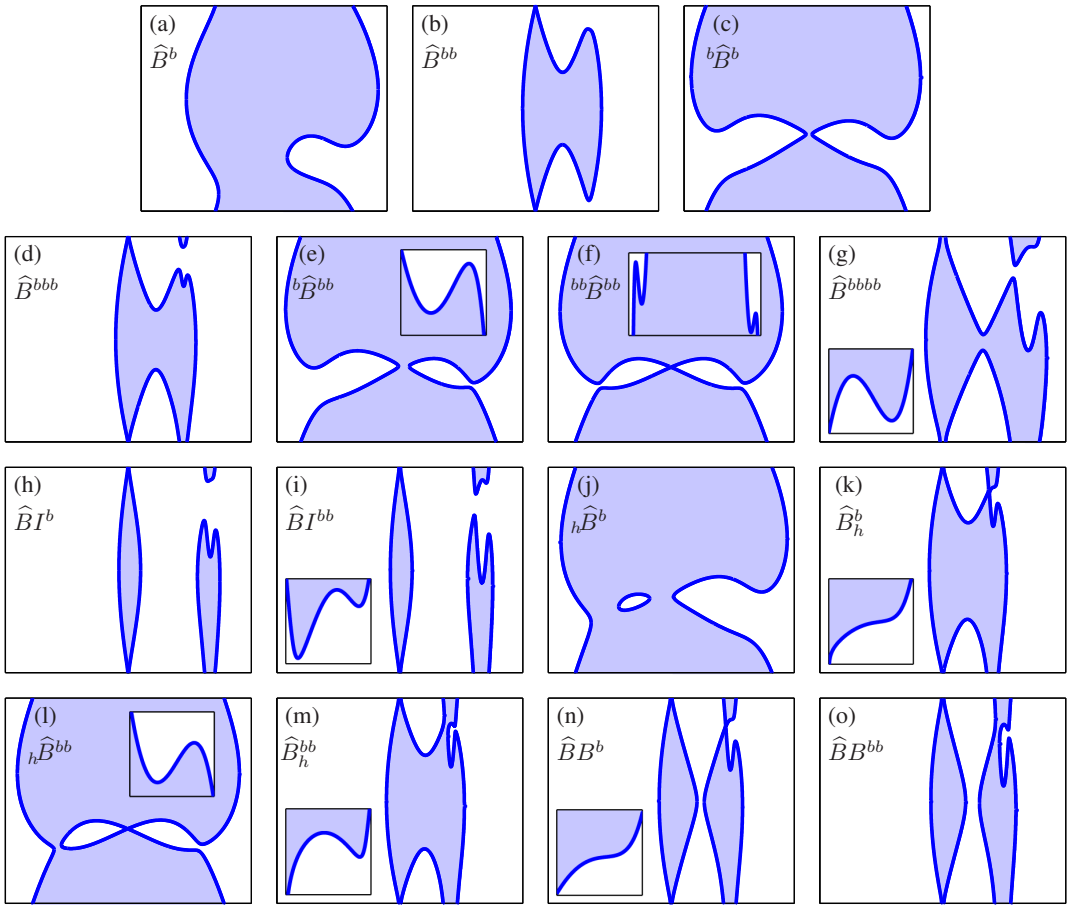

FIG. 19. *Additional types of EFM-surface of the 2FOF laser that feature bulges, represented by the projection (shaded) onto the* (ω_s, dC_p)*-plane; the blue boundary curves are found directly from* (4.1)*. Where necessary, insets show local enlargements. The corresponding regions in the* (Δ_1, Δ_2)*-plane can be found in Figs. 18, 23 and 27; for notation and the corresponding values of* Δ_1*,* Δ_2 *and* Λ *see Table 4. In all panels* $\omega_s \in [-0.3, 0.3]$ *and* $dC_p \in [-\pi, \pi]$*.*

a hole, which happens, for example, in the transition from $\widehat{B}^{bbb}$ to $\widehat{B}^{b}_{h}$. This new mechanism for the creation of a hole is illustrated in Fig. 20 for the simpler case of a transition from $\widehat{B}^{bb}$ to $\widehat{B}_{h}$; see also Fig. 19 (b) and Fig. 16 (d). In Fig. 20 (a1) and (a2) there are two bulges; one of the bulges is rather small, indicating that it has just been created in a nearby cubic tangency. At the saddle transition S_C in Fig. 20 (b) we find that the two bulges connect locally in the central point of a cone that is aligned in the dC_p-direction. In contrast to the case shown in Figure 11, the geometry of the EFM-surface is now such that this bifurcation leads to the creation of a hole; see panels (c1) and (c2). This hole can then disappear again when the (red) curve S_N in Fig. 18 is crossed; for example, this happens in the transition from $\widehat{B}^{b}_{h}$ to $\widehat{B}^{b}$.

The connection between cubic tangency and the singularity transitions is given by codimension-two points on the locus of cubic tangency. This feature is prominent in Fig. 18, where curves S_N (red) and S_C (blue) of saddle transition end at (purple) points on the (grey) curve $\mathcal{C}_d$. In Fig. 21 we present a local unfolding of such a codimension-two point, which is characterised by the fact that the envelope curve given by (3.9) has a cusp point. When making a circle around the codimension-two point $D\mathcal{C}_{NC}$ on the curve $\mathcal{C}$, starting at region 1, one finds that a hole appears near the boundary

name	C_{min}	C_{max}	panel	Δ_1	Δ_2	Λ
$\widehat{B}^b$	1	2	Fig. 19 (a)	-0.0200	0.2000	0.098
$\widehat{B}^{bb}$	1	2	Fig. 19 (b)	0.1320	0.1300	0.010
${}^b\widehat{B}^b$	1	3	Fig. 19 (c)	-0.2400	0.2300	0.098
$\widehat{B}^{bbb}$	1	3	Fig. 19 (d)	0.1400	0.1300	0.010
${}^b\widehat{B}^{bb}$	1	3	Fig. 19 (e)	-0.2300	0.2170	0.098
${}^{bb}\widehat{B}^{bb}$	1	3	Fig. 19 (f)	-0.2140	0.2150	0.098
$\widehat{B}^{bbbb}$	1	3	Fig. 19 (g)	-0.2350	0.1780	0.020
$\widehat{B}I^b$	1	3	Fig. 19 (h)	0.2100	0.1900	0.010
$\widehat{B}I^{bb}$	1	3	Fig. 19 (i)	0.2150	0.1850	0.098
${}_h\widehat{B}^b$	1	3	Fig. 19 (j)	-0.2120	0.2400	0.098
$\widehat{B}^b_h$	1	3	Fig. 19 (k)	0.1300	0.1161	0.010
${}_h\widehat{B}^{bb}$	1	3	Fig. 19 (l)	-0.2120	0.2200	0.098
$\widehat{B}^{bb}_h$	1	3	Fig. 19 (m)	0.1337	0.1161	0.010
$\widehat{B}B^b$	2	3	Fig. 19 (n)	0.2100	0.1600	0.010
$\widehat{B}B^{bb}$	2	3	Fig. 19 (o)	0.1530	0.1355	0.010

TABLE 4

Notation and parameter values for the types of EFM-surface in Fig. 19; the second and third column show the minimal number $C_{\min}$ and the maximal number $C_{\max}$ of EFM-components (for suitable fixed dC_p) of the type.

of EFM-surface in the saddle transition S_N; compare with Fig. 20. The hole then disappears in the saddle transition S_C. As a result, there are now two bulges, that is, pairs of local maxima and minima with respect to dC_p, which disappear one after the other when the cubic tangency curve $\mathcal{C}$ is crossed twice to complete the circle back to region 1. This unfolding can indeed be found locally in Fig. 18, but note that it involves the EFM-surface of type $\widehat{B}^b$ as that corresponding to region 1 in Fig. 21; hence, region 2 corresponds to $\widehat{B}^b_h$, region 3 to $\widehat{B}^{bbb}$, and region 4 to $\widehat{B}^{bb}$.

A second case of a codimension-two point on the curve of cubic tangency can be found in Fig. 15, where the curves M (orange) and S_ω (green) end at (golden) points on the (black) curve $\mathcal{C}_a$. The local unfolding of such a codimension-two point is presented in Fig. 22; it is again characterised by a cusp point on the envelope curve given by (3.9), but this time the cusp points the other way with respect to the EFM-surface. When making a circle around the codimension-two point $D\mathcal{C}_{NC}$ on the curve $\mathcal{C}$, starting at region 1, an island is created when the minimax transition M is crossed; this island then merges with the remainder of the EFM-surface in the saddle transition S_ω. As a result, there are again two bulges, which disappear one after the other when the curve $\mathcal{C}$ is crossed twice to complete the circle back to region 1. This unfolding can be found locally in Fig. 15, where the EFM-surface of type $\widehat{B}I$ corresponds to region 1 in Fig. 21; hence, region 2 corresponds to $\widehat{B}II$, region 3 to $\widehat{B}I^{bb}$, and region 4 to $\widehat{B}I^b$. Note that, in terms of the envelope curve (3.9), the unfolding in Fig. 22 is topologically equivalent to that in Fig. 21. However, the two unfoldings differ in where (the projection of) the EFM-surface lies with respect to the boundary; hence, the respective panels of Fig. 21 and Fig. 22 (where the EFM-surface is always on the left) can be transformed into one another by exchanging the colours blue and white in the regions, followed by a reflection.

Note that Fig. 19 shows the comprehensive list, in order of increasing complexity, of EFM-surface types that feature bulges — of which there are quite a few more than we identified in

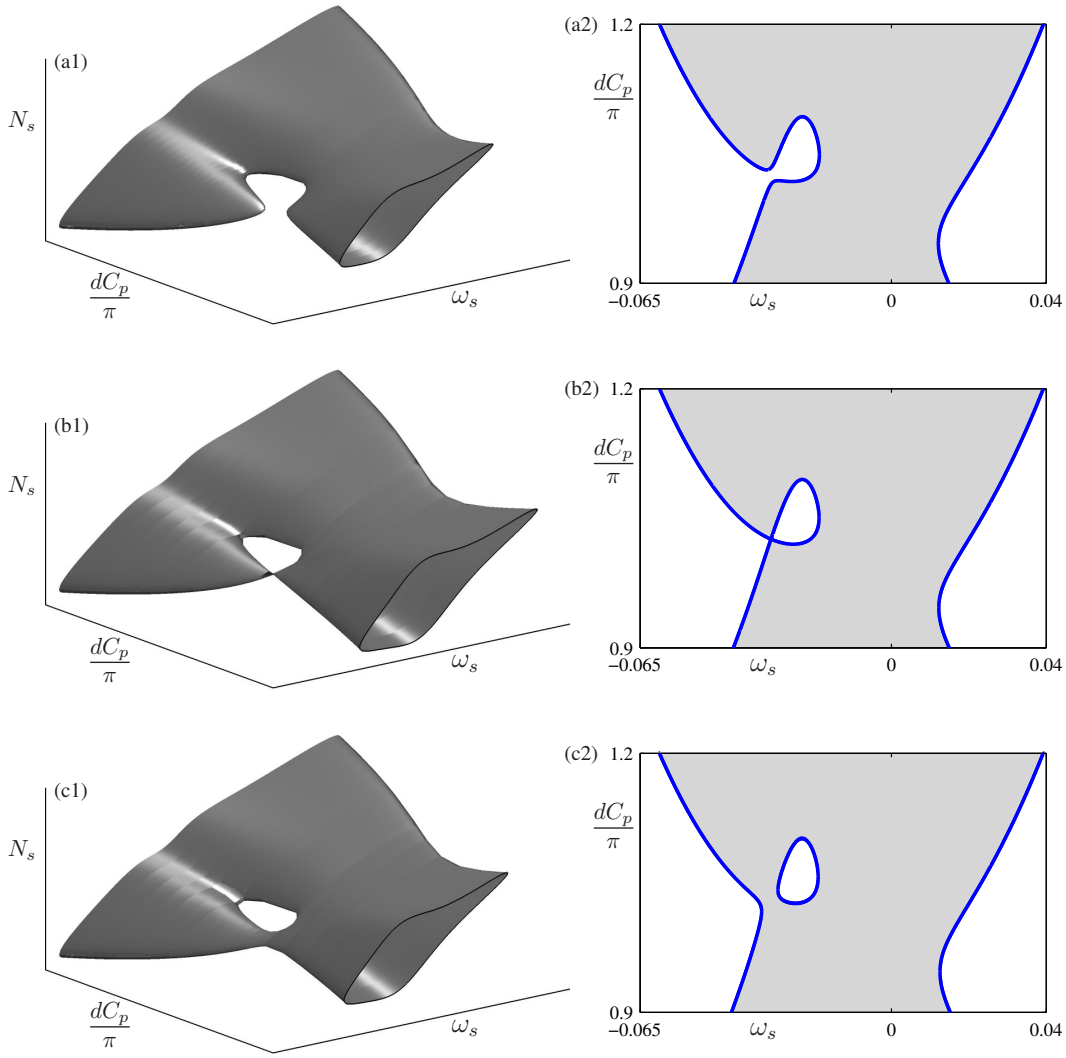

FIG. 20. *Global manifestation of local saddle transition S_C of the EFM-surface where two bulges connect to form a hole. Panels (a1)–(c1) show the relevant part of the EFM-surface and panels (a2)–(c2) the corresponding projection onto the (ω_s, dC_p)-plane. Here $\Lambda = 0.015$ and $\Delta_2 = -0.02$, and $\Delta_1 = -0.0248$ in (a), $\Delta_1 = -0.02498$ in (b) and $\Delta_1 = -0.0252$ in (c).*

Fig. 18. Additional EFM-surface types can be found near the diagonal of the (Δ_1, Δ_2)-plane, but further away from the central point $\Delta_1 = \Delta_2 = 0$. Figure 23 (a) shows the respective enlargement of the EFM-surface bifurcation diagram from Fig. 15, which features an interaction of cubic tangency curves $\mathcal{C}_a$ with saddle-transition curves S_C and S_ω. We find five additional EFM-surface types with bulges, representatives of which in the (ω_s, dC_p)-plane are also shown in Fig. 19 (h), (i), (k), (n) and (o); for notation and parameter values of the individual panels see again Table 4. Note, in particular, that crossing the saddle-transition curve S_ω may lead to secondary bands or islands with bulges.

To obtain the remaining cases of EFM-surface types with bulges in Fig. 19 it is necessary to change the filter width parameter Λ. As an example of how new regions of EFM-surface types are

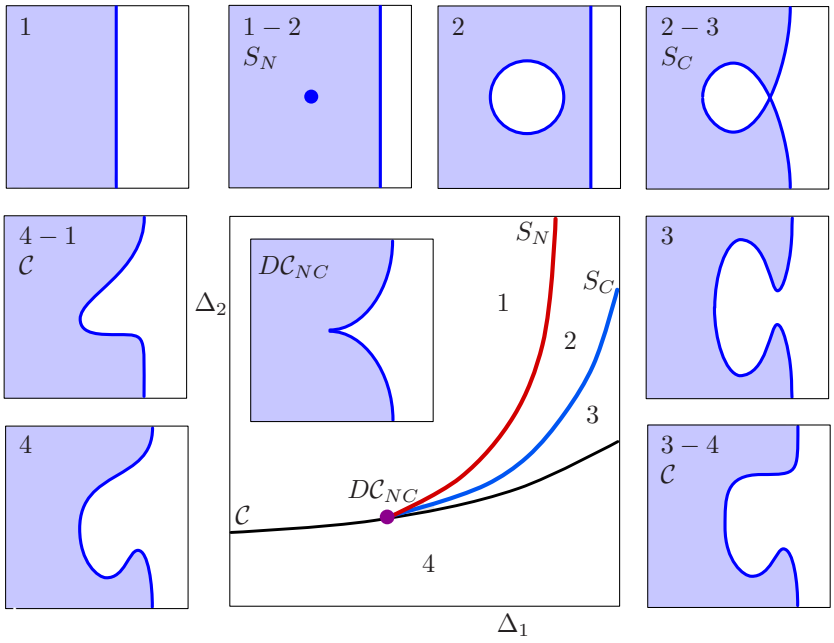

FIG. 21. *Sketch of the local bifurcation diagram in the* (Δ_1, Δ_2)*-plane near the (purple) codimension-two point* DC_{NC} *on the curve* $\mathcal{C}$ *of cubic tangency, from which the (red) curve* S_N *and the (blue) curve* S_C *of saddle transition emanate; compare with Figs. 18 and 27 (a) and (b).*

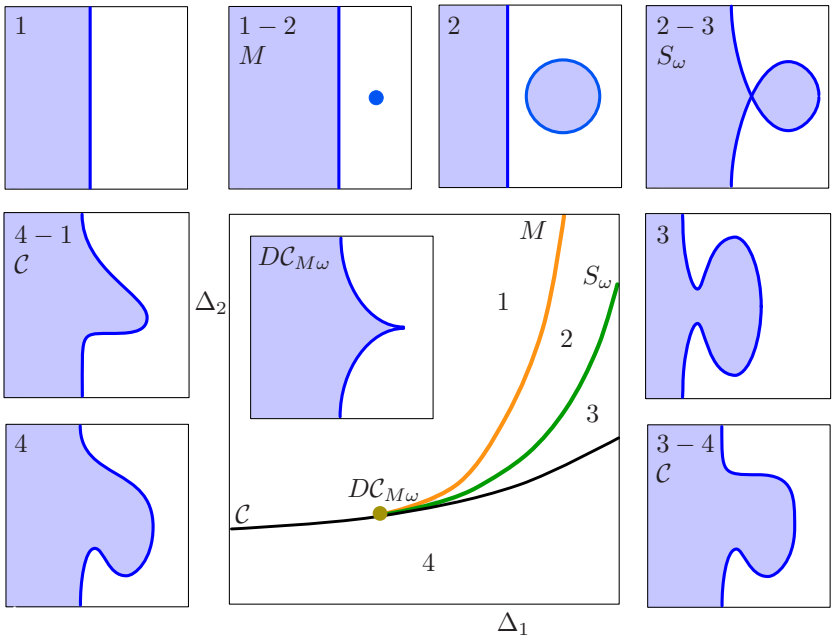

FIG. 22. *Sketch of the local bifurcation diagram in the* (Δ_1, Δ_2)*-plane near the (golden) codimension-two point* $DC_{M\omega}$ *on the curve* $\mathcal{C}$ *of cubic tangency, from which the (orange) curve* M *and the (green) curve* S_ω *of saddle transition emanate; compare with Figs. 15 and 26.*

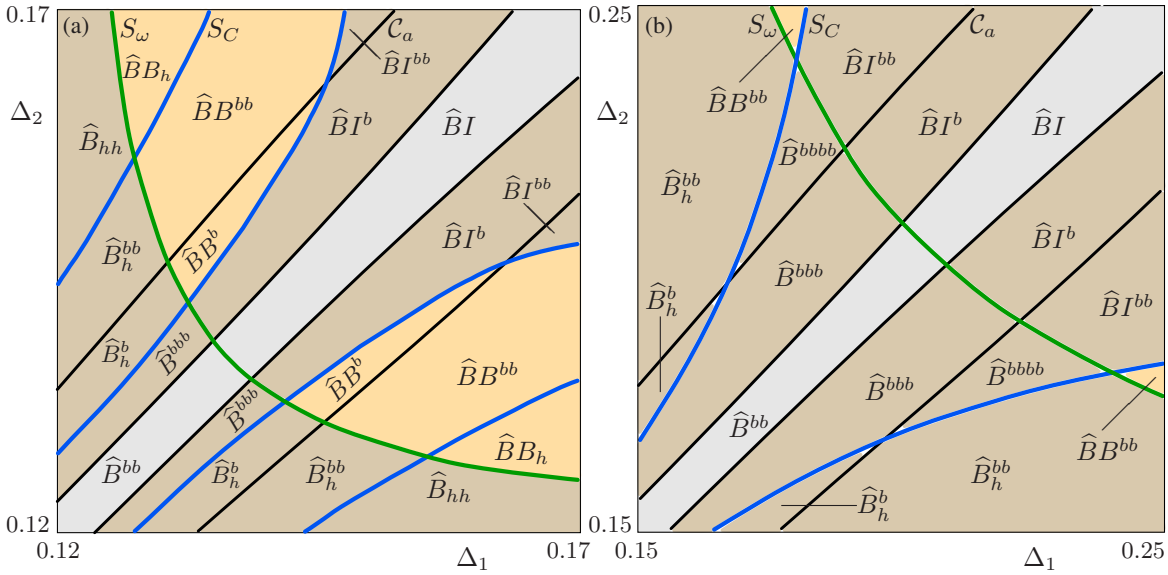

FIG. 23. *Enlargement near the diagonal of the* (Δ_1, Δ_2)*-plane with (blue) curves of* S_C *transition, (green) curves of* S_ω *transition, and* S_C *transition, and (black) curves* $\mathcal{C}_d$ *of cubic tangency; see Fig. 19 for representatives of the labelled types of the EFM-surface and Table 4 for the notation. Panel (a) is for* $\Lambda = 0.01$ *as Fig. 15, and panel (b) is for* $\Lambda = 0.02$

created in a subtle way with changing Λ, Fig. 23 (b) shows a similar enlargement as panel (a), but now for $\Lambda = 0.02$. Note that the relative position of the curve S_ω has changed in such a way that one finds a region where the EFM-surface is of type $\widehat{B}^{bbbb}$; see Fig. 19 (g). The location in $(\Delta_1, \Delta_2, \Lambda)$-space of all EFM-surface types in Fig. 19 can be found in Table 4; we will encounter more types in the next section.

4.5. Dependence of the EFM-surface bifurcation diagram on the filter width Λ. We now consider more globally how the EFM-surface bifurcation diagram in the (Δ_1, Δ_2)-plane changes with the common filter width Λ. Figure 6 already indicated that substantial changes to the regions of band-like EFM types must be expected. In particular, for sufficiently large Λ the grey and orange curves in Fig. 6 do not extend to infinity in the (Δ_1, Δ_2)-plane any longer. To study this phenomenon we compactify the (Δ_1, Δ_2)-plane by the stereographic change of coordinates

$$\widetilde{\Delta}_i = \frac{\Delta_i}{|\Delta_i| + \eta}, \quad \eta > 0. \tag{4.3}$$

Note that (4.3) transforms the (Δ_1, Δ_2)-plane to the square $[-1, 1] \times [-1, 1]$ in the $(\widetilde{\Delta}_1, \widetilde{\Delta}_2)$-plane, where $\widetilde{\Delta}_i = \pm 1$ corresponds to $\Delta_i = \pm\infty$; we speak of the $(\widetilde{\Delta}_1, \widetilde{\Delta}_2)$-square from now on. The parameter η is the value of Δ_i that is mapped to $\widetilde{\Delta}_i = 0.5$, and we chose $\eta = 0.4$ to ensure that the main structure of the EFM-surface bifurcation diagram in the (Δ_1, Δ_2)-plane is represented well in the $(\widetilde{\Delta}_1, \widetilde{\Delta}_2)$-square.

Figure 24 shows the EFM-surface bifurcation diagram in the $(\widetilde{\Delta}_1, \widetilde{\Delta}_2)$-square in the style of Fig. 15. The (white) regions of band-like EFM-surface types are labelled; see Table 1. Also shown are the singularity transitions curves M (orange), S_C (blue), S_ω (green), S_N (red) and the cubic tangency curves $\mathcal{C}_a$ (black) and $\mathcal{C}_d$ (grey).

Figure 24 (a) for $\Lambda = 0.01$ is simply the compactified version of Fig. 15 in the $(\widetilde{\Delta}_1, \widetilde{\Delta}_2)$-square. Note that the (orange and grey) stripes now end at discrete points at the sides of the square.

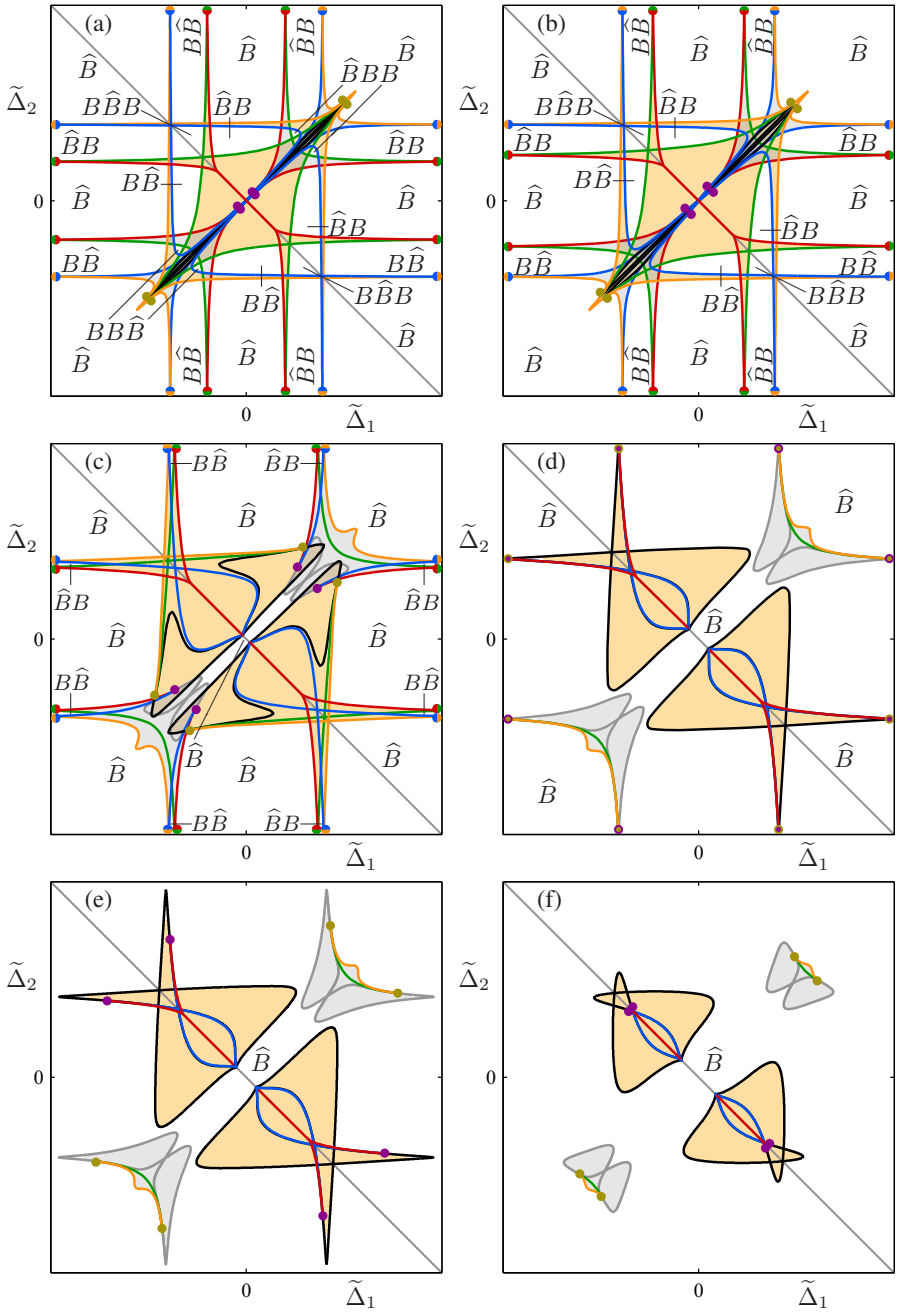

FIG. 24. *EFM-surface bifurcation diagram in the compactified* $(\widetilde{\Delta}_1, \widetilde{\Delta}_2)$*-square,* $[-1,1]\times[-1,1]$*, showing regions of band-like EFM-surface types; compare with Fig. 15. The boundary of the square corresponds to* $\Delta_i = \pm\infty$*; from (a) to (e)* Λ *takes values* $\Lambda = 0.01$*,* $\Lambda = 0.015$*,* $\Lambda = 0.06$*,* $\Lambda = 0.098131$*,* $\Lambda = 0.1$ *and* $\Lambda = 0.13$*. The boundary curves are the singularity transitions* M *(orange curves),* S_C *(blue curves),* S_ω *(green curves),* S_N *(red curves) and locus of cubic tangencies* $\mathcal{C}_a$ *(black curves) and* $\mathcal{C}_d$ *(grey curves); also shown are codimension-two points (purple and golden), points on the bounduary and the anti-diagonal.*

Namely, for $\Delta_i = \pm\infty$ the respective filter does not influence the laser any longer, so that the system reduces to single-FOF laser on the sides of the $(\widetilde{\Delta}_1, \widetilde{\Delta}_2)$-square. Hence, the end points of the stripes are exactly the four intersection points of the line $\Lambda = 0.01$ with the light grey limiting curve in Fig. 7 (b). As Λ is increased, the grey and orange areas of other EFM-surface types expands and four (symmetry-related) smaller regions of band-like EFM-surface types $BB\widehat{B}$ and $\widehat{B}BB$ disappear; see Fig. 24 (b). As Λ is increased further, additional regions of band-like EFM-surface types disappear; see Fig. 24 (c). In the process the pairs of (orange and grey) stripes move closer together, owing to the fact that the four intersection points with the light grey curve in Fig. 7 (b) do the same. Moreover, the (black and grey) cubic tangency curves extend over a much larger region of the $(\widetilde{\Delta}_1, \widetilde{\Delta}_2)$-square; hence, the region near $\widetilde{\Delta}_1 = \widetilde{\Delta}_2 = 0$ where one finds EFM-surface type $\widehat{B}$ opens up considerably.

Figure 24 (d) is for $\Lambda = 0.098131$, which is the approximate value of Λ where one finds the cusp points of the grey limiting curve in Fig. 7 (c). This value can be computed analytically as

$$\Lambda_C = \frac{2}{3\sqrt{3}}\kappa\sqrt{1+\alpha^2} \tag{4.4}$$

from the formula in [28] for the single-FOF laser. In the context of the EFM-surface bifurcation diagram, this values corresponds to a bifurcation at infinity of the (Δ_1, Δ_2)-plane and, hence, a bifurcation at the boundary of the $(\widetilde{\Delta}_1, \widetilde{\Delta}_2)$-square. More specifically, for $\Lambda = \Lambda_C$ the pairs of orange and grey stripes now end at single points. the cubic tangency curves $\mathcal{C}_a$ (black) and $\mathcal{C}_d$ (grey) extend all the way to the boundary of the square. Note further that the central region of EFM-surface type $\widehat{B}$ is no longer bounded by curves of cubic tangency but is now joined up with four, previously separated regions of the same type. For $\Lambda > \Lambda_C$ the stripes no longer extend to the boundary of the square. As a result, one now finds orange and grey pairs of islands that are bounded almost entirely by (black and grey) cubic tangency curves. The complement of these islands is a single connected (white) region of EFM-surface type $\widehat{B}$; see Fig. 24 (e). When Λ is increased further, these islands become smaller; see Fig. 24 (f).

4.6. Unfolding of the bifurcation at infinity. As we know from Sec. 4.4, the boundaries of the orange and grey regions are formed not only by the curves $\mathcal{C}_a$ and $\mathcal{C}_d$ of cubic tangency, but also by the singularity transitions M, S_C, S_ω and S_N. Figure 25 shows how these boundary curves interact in the transition through $\Lambda = \Lambda_C$ in a neighbourhood of the respective point on the boundary of the $(\widetilde{\Delta}_1, \widetilde{\Delta}_2)$-square. There are two cases: one for the orange regions and one for the grey regions in Fig. 24.

Row (a) of Fig. 25 shows the transition for the grey regions, which involves the (grey) cubic tangency curve $\mathcal{C}_d$; labels in the regions indicate the respective EFM-surface type. Before the bifurcation, that is, when $\Lambda < \Lambda_C$, the grey region extends to two points on the boundary of the $(\widetilde{\Delta}_1, \widetilde{\Delta}_2)$-square. As we have seen in Fig. 15, these points are the limits of the pair of curves M and S_C and of the the pair of curves S_ω and S_N, respectively; see Fig. 25 (a1). Note further that the singularity transition curves S_N and S_C end at a (purple) codimension-two point $D\mathcal{C}_{NC}$ on the cubic tangency curve $\mathcal{C}_d$; compare with Fig. 21. The EFM-surface types in the respective regions are also shown. When Λ_C is approached, the two limit points of the pairs of curves M and S_C and S_ω and S_N approach each other. At the same time, the codimension-two point, and the curve $\mathcal{C}_a$ with it, approach the boundary of the $(\widetilde{\Delta}_1, \widetilde{\Delta}_2)$-square; as a result, the curves S_N and S_C become shorter. At the moment of transition at $\Lambda = \Lambda_C$, shown in Fig. 25 (a2), the grey region is bounded by the minimax transition curve M and by one branch of the cubic tangency curve $\mathcal{C}_d$, which both end at a single point on the boundary. The curve S_ω and a second branch of $\mathcal{C}_d$ also end at this point on the boundary. For $\Lambda > \Lambda_C$, as in Fig. 25 (a3), all curves detach from the boundary of the $(\widetilde{\Delta}_1, \widetilde{\Delta}_2)$-square; furthermore, the singularity transition curves M and S_ω are now attached to

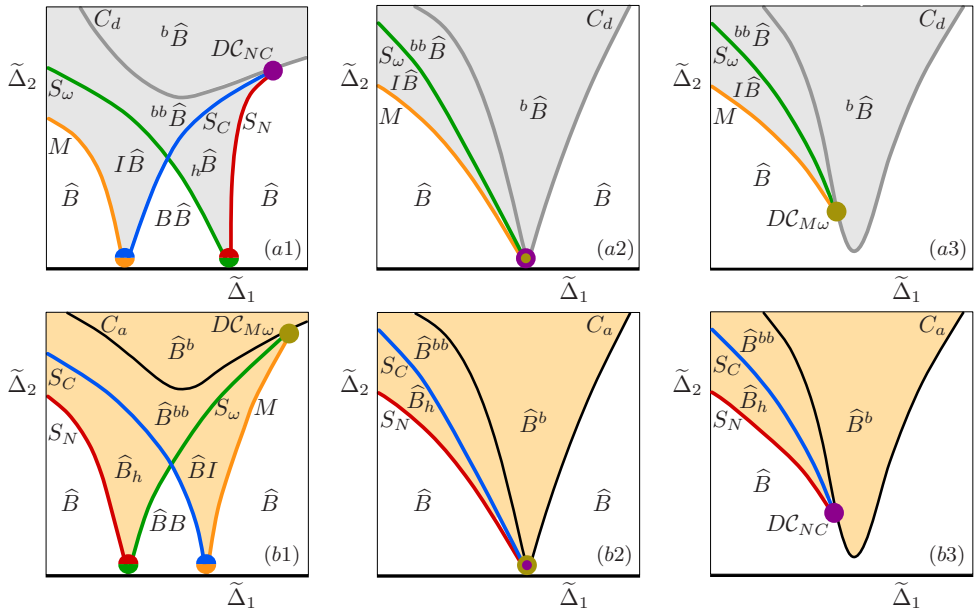

FIG. 25. *Sketch of EFM-surface bifurcation diagram near the boundary* $\{\widetilde{\Delta}_2 = -1\}$ *of the* $(\widetilde{\Delta}_1, \widetilde{\Delta}_2)$*-square in the transition through* $\Lambda = \Lambda_C$*. Panels (a1)–(a3) show the transition involving the (black) curve* $\mathcal{C}_a$ *of cubic tangency that bounds the orange islands, and panels (b1)–(b3) show the transition involving the (grey) curve* $\mathcal{C}_d$ *of cubic tangency that bounds the grey islands; compare with Fig. 24 (c)–(e).*

the cubic tangency curve $\mathcal{C}_d$ at a (golden) codimension-two point $DC_{M\omega}$; compare with Fig. 22. Hence, the grey island created in this transition, which is invariant under reflection in the diagonal, is bounded by the curves $\mathcal{C}_d$ and M.

Row (b) of Fig. 25 shows the transition for the orange regions, which involves the (black) cubic tangency curve $\mathcal{C}_a$; again, the respective EFM-surface types are indicated. This transition is very similar to that in Fig. 25 (a), but note that it now involves a (golden) codimension-two point $DC_{M\omega}$ on the curve $\mathcal{C}_a$ for $\Lambda < \Lambda_C$, and a (purple) codimension-two point DC_{NC} for $\Lambda > \Lambda_C$. As a result of this transition the orange island created in this transition, which is invariant under reflection in the anti-diagonal, is bounded by the curves $\mathcal{C}_a$ and S_N.

4.7. Islands of non-banded EFM-surface types. The grey islands are associated with the diagonal where $\Delta_1 = \Delta_2$, along which the 2FOF laser reduces to the single-FOF laser with effective feedback rate given by (3.11). Hence, the width of the grey islands along the diagonal is determined by the intersection points of the horizontal line for the given value of Λ with the curve in Fig. 7 (c). A grey island for $\Lambda = 0.1$ is shown in Fig. 26. It contains regions of (non-banded) EFM-surface types $\widehat{B}^b$, $\widehat{B}^{bb}$ and $\widehat{B}I$, which are bounded by the cubic tangency curve $\mathcal{C}_d$ and singularity transition curves M (orange) and S_ω (green); the latter curves end at two (golden) points $DC_{M\omega}$ on the curve $\mathcal{C}_d$. When Λ is increased, the grey islands remain topologically the same and simply shrink down to a point. This happens when Λ has the value of the cusp points of the curve in Fig. 7 (c), which can again be computed analytically from the formula in [28] for the single-FOF laser as

$$\Lambda_I = 2\,\Lambda_C = \frac{4}{3\sqrt{3}}\kappa\sqrt{1+\alpha^2} \approx 0.196261. \tag{4.5}$$

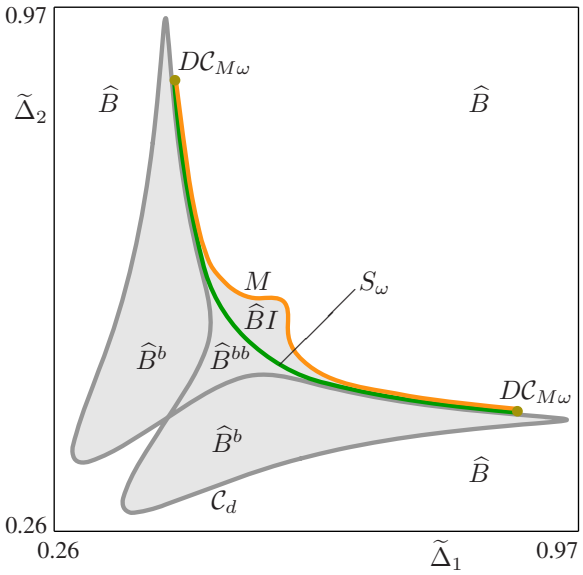

FIG. 26. *Grey island for* $\Lambda = 0.1$ *in the* $(\widetilde{\Delta}_1, \widetilde{\Delta}_2)$*-plane with regions of non-banded EFM-surface types; compare with Fig. 24 (e).*

Furthermore, we can conclude from the single-FOF limit along the diagonal that the two symmetric grey islands disappear at

$$\Delta_1 = \Delta_2 = \Delta_{Id} = \frac{8\sqrt{2}}{3\sqrt{3}}\kappa\sqrt{1+\alpha^2} \approx 0.555111. \tag{4.6}$$

For $\Lambda > \Lambda_I$ the EFM-surface bifurcation diagram in the $(\widetilde{\Delta}_1, \widetilde{\Delta}_2)$-square — and, hence, also in the (Δ_1, Δ_2)-plane — does no longer contain (grey) islands that are symmetric with respect to the diagonal.

The orange islands that exist for $\Lambda > \Lambda_C$ are associated with the anti-diagonal where $\Delta_1 = -\Delta_2$. Figure 27 (a) shows an orange island for $\Lambda = 0.1$ with regions of (non-banded) EFM-surface types; see also the enlargement in the inset panel. Apart from the cubic tangency curve $\mathcal{C}_a$, we find curves S_C (blue) and S_N (red) of singularity transition. Two curves S_C emerge from a boundary point of the island on the anti-diagonal where four branches of $\mathcal{C}_a$ connect in a pair of cusps. The two curves S_C follow two branches of $\mathcal{C}_a$ closely and end at two (purple) points $D\mathcal{C}_{NC}$ on the curve $\mathcal{C}_a$. The two curves S_N emerge from a different point on the anti-diagonal and also follows $\mathcal{C}_a$ closely to the same two end points. The (red) section of the anti-diagonal in between the two points from which the curves S_C and S_N emerge, respectively, corresponds to a degenerate saddle transition S_N. The remainder of the anti-diagonal corresponds to a degenerate saddle transition S_C; see the discussion in Sec. 4.4. Overall, we find a quite complicated but consistent structure of the orange island. It features the (non-banded) EFM-surface types $\widehat{B}_h$, ${}_h\widehat{B}_h$, $\widehat{B}^b$, $\widehat{B}^{bb}$, ${}_h\widehat{B}^b$, ${}^b\widehat{B}^b$, ${}_h\widehat{B}^{bb}$, ${}^b\widehat{B}^{bb}$ and ${}^{bb}\widehat{B}^{bb}$, of which the last five EFM types with bulges are new; compare with Fig. 19.

As Λ is increased, the orange island undergoes topological changes. First, the (purple) end points of the curves S_C and S_N move across a branch of the cubic tangency locus $\mathcal{C}_a$. As a result, the entire island is now bounded by $\mathcal{C}_a$ and the regions $\widehat{B}_h$ and $\widehat{B}^{bb}$ (and their symmetric counterparts) disappear; see Fig. 27 (b). The next qualitative change concerns the cubic tangency locus $\mathcal{C}_a$, which loses two intersection points, resulting in the loss of two (symmetrically related) regions of EFM types ${}^b\widehat{B}$ and $\widehat{B}^b$; see Fig. 27 (c). When Λ is increased further, two intersection

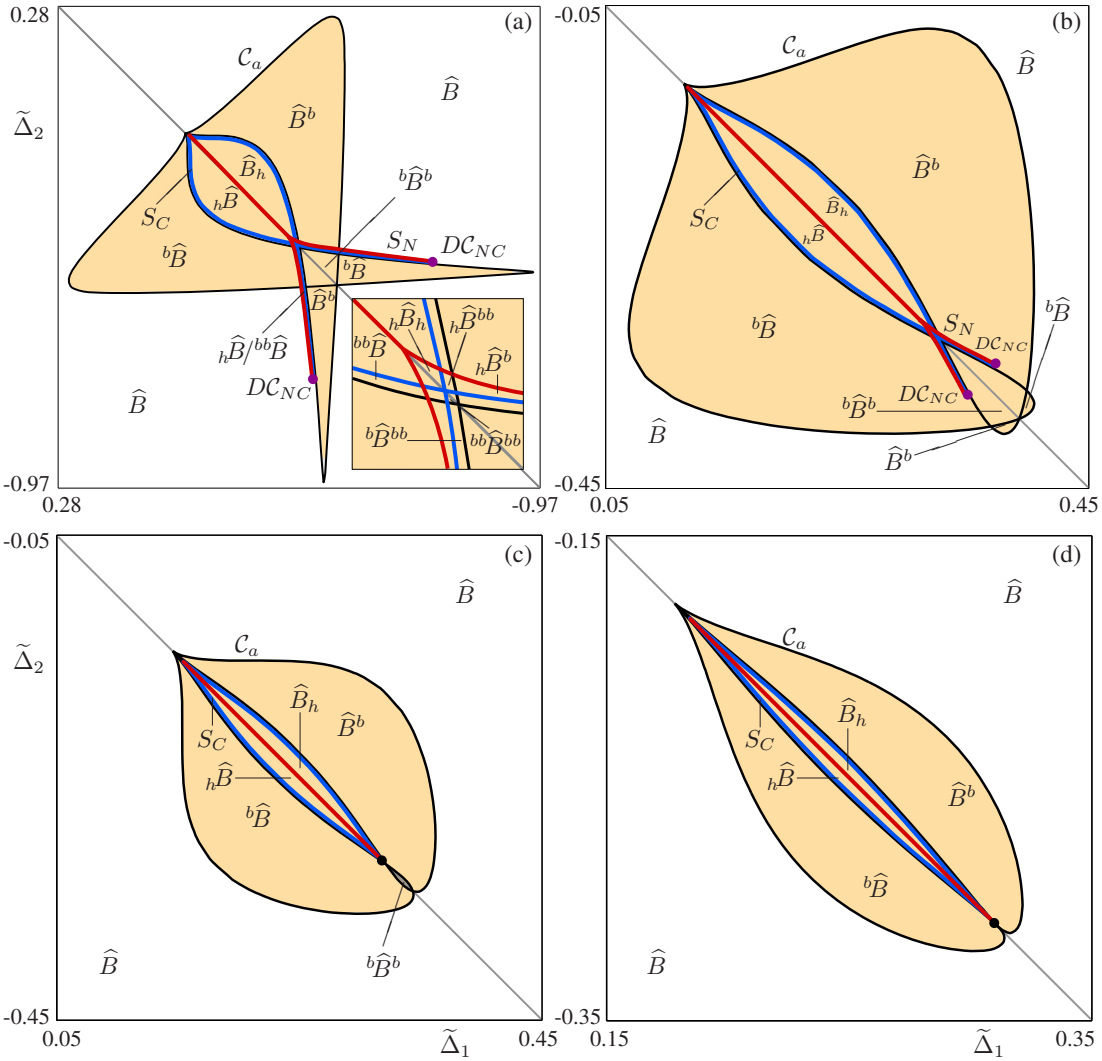

FIG. 27. *Orange island in the* $(\widetilde{\Delta}_1, \widetilde{\Delta}_2)$*-plane with regions of non-banded EFM-surface types; the inset in panel (a) shows the details of curves and regions. From (a) to (d)* Λ *takes the values* $\Lambda = 0.1$, $\Lambda = 0.145$, $\Lambda = 0.166$ *and* $\Lambda = 0.179$*; compare panel (a) with Fig. 24 (e).*

points of curves $\mathcal{C}_a$ on the anti-diagonal come together and merge into a point where four branches of $\mathcal{C}_a$ connect. The result is the loss of region ${}^b\widehat{B}^b$; see Fig. 27 (d). We found that the orange island does not undergo further qualitative changes, but rather shrinks down to a point and disappears. This happens at $\Lambda =\approx 0.196261$, and this numerical value agrees up to numerical precision with that for Λ_I from (4.5). In fact, consideration of (3.9) for $\Delta_1 = -\Delta_2$ confirms this observation; furthermore, the position of where the islands disappear can be computed as

$$\Delta_1 = -\Delta_2 = \Delta_{Ia} = \Delta_{Id}/4 = \frac{2\sqrt{2}}{3\sqrt{3}}\kappa\sqrt{1+\alpha^2} \approx 0.138778. \tag{4.7}$$

We can now conclude that for $\Lambda > \Lambda_I$ there are no islands at all, so that the entire (Δ_1, Δ_2)-plane consists of a single region of EFM type $\widehat{B}$. Physically, this means that the transmittance

profiles of both filters are so wide that the filters reflect the laser light of different frequencies effectively in the same way. In other words, for sufficiently large Λ the feedback is no longer frequency selective within the laser spectral range and the 2FOF laser is effectively a 2COF laser.

5. EFM-stability regions for $d\tau = 0$. The rationale for the classification of the EFM-surface presented in the previous section is to provide the backbone of the dynamics of the 2FOF laser. From this point of view, knowledge of the EFMs is important even when they are not stable, that is, when they are of saddle type. Indeed, it has been demonstrated that continuous waves (CWs) of saddle type may play an important role in organising the dynamics of a laser with delayed feedback. Best known is the discovery that saddle CWs of the COF laser play an important role for observed repeated and irregular power drop-outs known as low-frequency fluctuations and coherence collapse [25, 30, 56, 57, 60]. More specifically, saddle CWs are approached along their stable direction during the build-up of the laser power, until the trajectory is finally reinjected along an unstable direction of a CW to a region of low-power and the process of build-up repeats, but towards a different CW; one also speaks of itinerancy with a drift or of the Sisyphus effect [25, 46].

On the other hand, stable continuous-wave solutions, with their steady-state laser power and given fixed frequency, are of interest in many applications and can indeed be observed experimentally in lasers with delayed feedback. In the context of the 2FOF laser, these CWs are EFMs and, hence, we now address the question which of the EFMs that we found and classified are actually stable. In Sec. 4 we showed that the EFM-surface depends strongly on the parameters of the filtered feedback loop, and the goal now is to investigate the connection between changes to the surface itself and changes to the EFM stability. To this end, we consider representative choices of the EFM-surface in (ω_s, N_s, dC_p)-space and determine the regions of EFM stability on it. First, we consider in Sec. 5.1 the case of two identical undetuned feedback loops, where the EFM surface is always of type $\widehat{B}$, and we study the changes to the EFM stability region as the common filter width Λ approaches the limit of COF. We then perform a case study in Sec. 5.2 of how changes of the EFM stability regions are associated with changes of type of the EFM-surface as the detunings of the filters are changed. Throughout this section we consider a zero delay difference $d\tau = 0$ as in Sec. 4. The effect of a nonzero $d\tau$ on the EFM surface and the EFM stability regions is discussed in Sec. 6.

Stability regions on the EFM surface in (ω_s, N_s, dC_p)-space can also be found by numerical continuation with the package DDE-BIFTOOL. More specifically, we compute curves of EFMs for fixed dC_p, but now together with the relevant (largest) eigenvalues of their linearization. The result of these much more expensive calculations is a set of curves (for suitably many fixed values of dC_p) that are then rendered into a surface with EFM stability information on it. Throughout, regions of stable EFMs are marked as hatched green patches on the semitransparent grey EFM-surface; in fact, we use computed data for the hatching: each green curve is the actual stable part of the respective computed EFM branch; see Appendix A for more details. The remaining grey area of EFM-surface represents saddle EFMs. The boundary of a region of stable EFMs on the EFM-surface in (ω_s, N_s, dC_p)-space involves loci of saddle-node bifurcations and of Hopf bifurcations, and they are computed directly as curves with DDE-BIFTOOL. Throughout, saddle-node bifurcation curves are depicted as blue curves and Hopf bifurcation curves as red curves. For the purpose of this stability analysis we calculate only the saddle-node and Hopf bifurcation curves that bound the EFM-stability regions. These boundary curves meet at codimension-two Bogdanov-Takens, saddle-node Hopf and Hopf-Hopf bifurcation points.

To explain and illustrate our EFM stability results, we not only show the stability regions on the EFM-surface in (ω_s, N_s, dC_p)-space, but also in projections of the EFM-surface onto the (ω_s, dC_p)-plane. This is the representation that was used in Sec. 4 for the classification of the different topological types of the EFM-surface. As before, white regions of the (ω_s, dC_p)-plane are regions where no EFM exist. The blue region that represented the projection in Sec. 4 is now divided into regions of stable and unstable EFMs that are coloured green and grey, respectively.

This colouring of the (ω_s, dC_p)-projections is in agreement with the colouring of the EFM-surface itself. For clarity, we use solid green filling to indicate the stable EFM regions in the projections, instead of hatching. As in section Sec. 4, both the top and the bottom sheet of the EFM-surface are projected onto the (ω_s, dC_p)-plane; this means that each typical (non-boundary) point in the (ω_s, dC_p)-projection of the EFM-surface corresponds to two EFMs with different N_s values. As we will see, most EFM stability regions extend only over the bottom sheet of the EFM-surface, which corresponds to higher optical field amplitudes; however, for some parameter values stable EFMs can also be found on the top sheet of the EFM-surface.

5.1. EFM-stability for two identical undetuned filters. As we have shown in Sec. 4.5, the 2FOF laser approaches the COF laser in the limit of large filter width $\Lambda \to \infty$. In particular, for sufficiently large Λ (and any value of the detunings Δ_1 and Δ_2) the EFM-surface is of type $\widehat{B}$. For this reason we first consider the stability region on the EFM-surface of $\widehat{B}$ for $\Delta_1 = \Delta_2 = 0$.

Figure 28 shows the fundamental 2π interval of the EFM-surface. (Recall that the EFM-surface is connected at the points (ω_s, N_s, dC_p) = $(0, 0, (2n+1)\pi)$ with $n \in \mathbb{Z}$; compare with Sec. 4.) More specifically, shown is the stability region on the EFM-surface for $\Lambda = 0.001$ (a1), $\Lambda = 0.005$ (b1), and $\Lambda = 0.025$ (c1); the insets (a2)–(c2) show the corresponding projections onto the (ω_s, dC_p)-plane. Because the EFM-surface grows considerably with Λ, the three sets of panels in Fig. 28 are presented over different range of ω_s and N_s.

The EFMs are stable inside an annular region around the point $(0, 0)$ of the (ω_s, dC_p)-plane. The inner boundary of the EFM stability region formed by a (red) single closed curve of Hopf bifurcation. The outer boundary of the EFM stability region, on the other hand, changes considerably with Λ. For $\Lambda = 0.001$ as in Fig. 28 (a), it is formed by a pair of (red) curves of Hopf bifurcations and two segments of the (blue) curve of saddle-node bifurcations; this means that stable EFMs can be found only over a certain range of ω_s. For $\Lambda = 0.005$ as in Fig. 28 (b), two different pairs of Hopf bifurcation curves are involved in forming the outer stability boundary; moreover, more of this boudary is now formed by the curve of saddle-node bifurcations. Finally, for $\Lambda = 0.025$ as in Fig. 28 (c), the outer boundary of the stable EFM regions consist entirely of the (single) saddle-node bifurcation curve; more importanly, stable EFMs can now be found over the entire available range of ω_s.

Figure 28 shows only the most important changes of the EFM stability region, with increasing Λ. Indeed, the transition between the two limiting cases involves quite a number of changes to the curves that form the boundary of the EFM stability region. First of all, there are changes to the types and the numbers of codimension-two bifurcation points on the boundary of stable EFM region, which are associated with transitions through different kinds of codimension-three bifurcation points (including degenerate Bogdanov-Takens and degenerate saddle-node Hopf bifurcations). Moreover, there may be local rearrangements of curves of Hopf bifurcations that are associated with the transition through critical points on the surface of Hopf bifurcation; see [17, 27] for examples. In the spirit of this section, the detailed description of the transitions through codimension-three points is beyond the scope of this paper.

Note that Fig. 28 illustrates the transition with Λ between two limiting cases of a laser with monochromatic optical injection and the laser with COF. For $\Lambda = 0.001$ our findings are in qualitative agreement with results for the semiconductor laser subject to optical injection [75], whose locking region is bounded by curves of saddle-node and Hopf bifurcations. On the other hand, for $\Lambda = 0.25$ our results are in agreement with the findings for the COF laser [30, 38, 43, 47, 59]. Namely, stable EFMs appear in a saddle-node bifurcation and become unstable in a Hopf bifurcation that gives rise to light-amplitude oscillations known as relaxation oscillations [43, 47, 65].

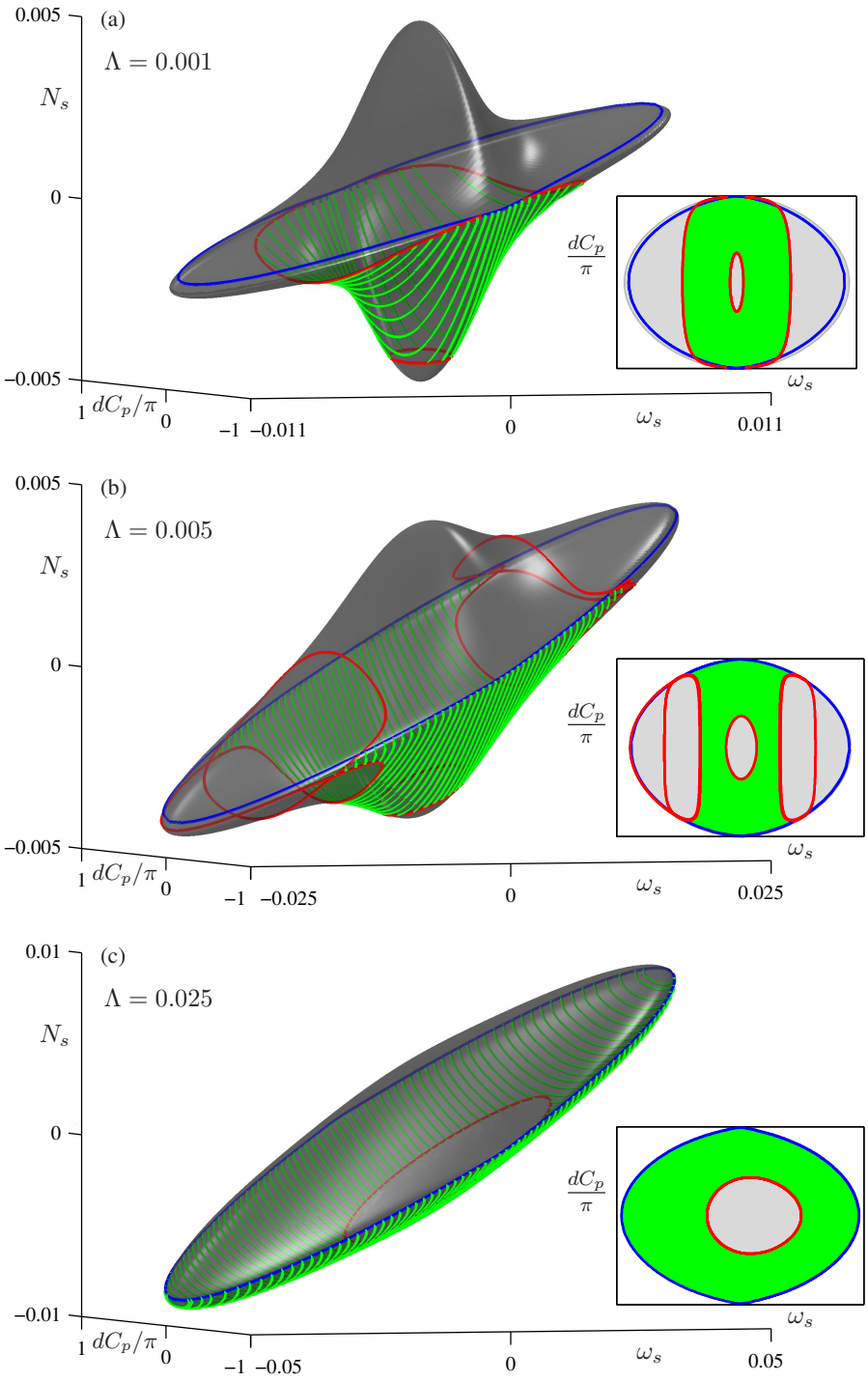

FIG. 28. *Dependence of the stability region on the EFM-surface of type* $\widehat{B}$ *for two identical and undetuned filters on their common filter width* Λ *(as indicated in the panels); here* $\Delta_1 = \Delta_2 = 0$, $\kappa = 0.01$ *and* $d\tau = 0$. *Panels (a1)–(c1) show the EFM-surface in* (ω_s, N_s, dC_p)*-space (semitransparent grey) with a stability region (green hatching) that is bounded by (blue) saddle-node bifurcation curves and by (red) Hopf bifurcation curves. Panels (a2)–(c2) show the corresponding projections onto the* (ω_s, dC_p)*-plane.*

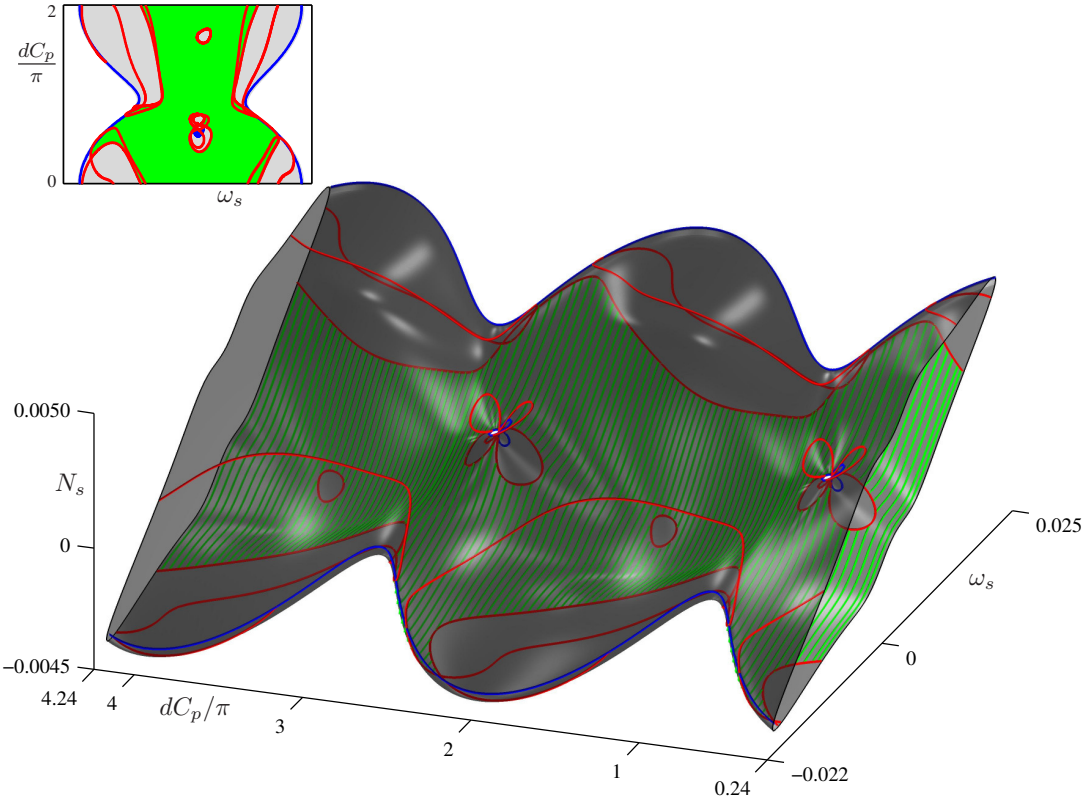

FIG. 29. *The EFM-surface with stability information, of type* $\widehat{B}_h$ *for* $\Delta_1 = 0.0065$ *and* $\Delta_2 = 0$. *Here* $\kappa = 0.01$, $\Lambda = 0.005$ *and* $d\tau = 0$*; curves and regions are coloured as in Fig. 28.*

5.2. Dependence of EFM-stability on the filter detunings. Figure 28 shows that the stability region may undergo physically relevant changes, while the EFM surface type remains unchanged. The question that we address now is what changes to the EFM stability region ensue when the type of the EFM surface changes with the filter detunings Δ_1 and Δ_2. To this end, we fix the filter width to the intermediate value $\Lambda = 0.005$ as in Fig. 28(b); moreover, as before we fix $\kappa = 0.01$ and $d\tau = 0$. Our goal is to present what the EFM stability regions looks like for several representative types of the EFM surface along a suitable path through the EFM-surface bifurcation diagram in the (Δ_1, Δ_2)-plane. Specifically, we consider the transition of the EFM surface from type $\widehat{B}$ through types $\widehat{B}_h$, ${}_h\widehat{B}_h$, ${}_h\widehat{B}$, $B\widehat{B}$, $B\widehat{B}_h$, $B\widehat{B}B$ and $I\widehat{B}B$ to type $I\widehat{B}I$. When the detuning is changed, one encounters transitions through bifurcation points of codimension-three as well as through extrema and saddle points of the surfaces of saddle-node and Hopf bifurcations in (C_p^1, dC_p, Δ_1)-space and (C_p^1, dC_p, Δ_2)-space. In these transitions boundary curves of the EFM stability regions emerge, disappear or connect differently, and this results in transformations of the stable EFM regions.

The starting point of our considerations is the EFM-surface in Fig. 28 (b), for $\kappa = 0.01$, $\Lambda = 0.005$, $\Delta_1 = 0$, $\Delta_2 = 0$ and $d\tau = 0$. Recall that in (ω_s, N_s, dC_p)-space this surface has infinitely many copies that connect at the point $(dC_p, \omega_s, N_s) = (k\pi, 0, 0)$ to form a surface of type $\widehat{B}$. Hence, its stability region is also connected and it has holes centred around the solitary laser frequency, represented here by $dC_p = 2k\pi$. We first fix $\Delta_2 = 0$ and increase Δ_1; in this way we move along the horizontal line $\Delta_2 = 0$ in the EFM-surface bifurcation diagram in the (Δ_1, Δ_2)-plane. When

Δ_1 is increased slightly, the EFM-surface remains a single band of type $\widehat{B}$, and its stability region is a band with holes around the points $dC_p = 2k\pi$.

With increasing Δ_1, we first observe that a hole appears in the EFM-surface when the saddle transition S_C is crossed so that its type changes from $\widehat{B}$ to $\widehat{B}_h$; compare Fig. 20 and Sec. 4.4.1. Figure 29 shows the EFM-surface of type $\widehat{B}_h$ for $\Delta_1 = 0.0065$ and $\Delta_2 = 0$ in (ω_s, N_s, dC_p)-space over a 4π-interval of dC_p; the inset is its (ω_s, dC_p)-projection of a 2π-interval of dC_p. Figure 29 clearly shows that there is a quite wide band of EFM-stability; the holes in the EFM-stability region near $dC_p = 2k\pi$ are now smaller and they have shifted when compared with those for $\Delta_1 = 0$ as in Fig. 28 (b). More importantly, there are now additional holes in the EFM-stability region around the hole of the EFM-surface. Clearly, there cannot be any stable EFMs if no EFMs exist, but notice that the hole in the stability region is considerably bigger than the hole in the EFM surface itself, which is actually quite small. The boundary of the EFM stability region near the hole in the EFM-surface is formed by curves of Hopf bifurcations that appeared in minimax transitions.

When Δ_1 is increased further, the curve of Hopf bifurcations around the small holes in the EFM-stability region near $dC_p = 2k\pi$ shrink to a point and disappear. At the same time, the hole in the EFM surface becomes larger, and so does the corresponding hole in the EFM-stability region. In fact, for sufficiently large Δ_1 the latter join up to form a band of instability, and this is shown in Fig. 30(a) where the EFM-surface for $\Delta_1 = 0.024$ and $\Delta_2 = 0$ is still of type $\widehat{B}_h$. The EFM-stability region is no longer connected and now effectively consists of two disjoint bands (plus two much smaller region and their synmetric copies, near the edge of the hole in the EFM surface and for negative ω_s). Note that the splitting of the single stable EFM region into two regions of stable EFMs that form bands expanding over the whole range of dC_p does not involve a topological change of the EFM-surface itself, but rather minmax tranistions and saddle connections of the saddle-node and Hopf bifurcation curves that bound the EFM stability regions.

We now fix $\Delta_1 = 0.024$ and decrease Δ_2 so that the EFM-surface type changes to ${}_h\widehat{B}_h$, as is shown in Fig. 30(b) for $\Delta_1 = 0.024$ and $\Delta_2 = -0.025$. The creation of a second hole in the EFM-surface is due to crossing the saddle transition S_N; see Fig. 13 in Sec. 4.3. Notice that the second hole does not really influence the nature of the EFM-stability region, which still consists mainly of two clearly separated band, one for positive and one for negative ω_s, which are bounded on both sides by a single curve of Hopf bifurcations. Additionally, there are small stable EFM regions near the edges of the two holes.

When Δ_2 is decreased further, the hole in the EFM surface for positive ω_s disappears and its type changes to ${}_h\widehat{B}$. As Fig. 31(a) for $\Delta_1 = 0.024$ and $\Delta_2 = -0.035$ shows, the EFM stability region is unaffected and still exists of two bands and smaller stability regions at the boundary of the holes. When the saddle transition S_ω is crossed the EFM-surface type changes to $B\widehat{B}$, as in Fig. 31(b) for $\Delta_1 = 0.024$ and $\Delta_2 = -0.037$. Notice that this topological change occurs outside the region of EFM-stability, which does not change qualitatively. However, the regions of stable EFMs near $\omega_s = 0$ is expanding.

We now fix $\Delta_2 = -0.037$ and again increase Δ_1. This initially leads to a transition of the EFM-surface to type $B\widehat{B}_h$ as in Fig. 32(a) for $\Delta_1 = 0.035$ and $\Delta_2 = -0.037$. We find that, as the extra hole in the EFM surface grows, it is also associated with the boundary of the expanding regions of stable EFMs near $\omega_s = 0$. As Fig. 32(a) shows, these regions grow so much towards one another that they then form a third, central band of EFM stability. The expansion of the stable EFM region around the central laser frequency can be explained by the observation that, as the detuning of the filters increases, the frequencies close to the central laser frequency are subject to weaker feedback from the flanks of the filter's transmittance profiles. As Δ_1 is increased further, the saddle transition S_ω is encountered and the EFM-surface type changes to type $B\widehat{B}B$. As Fig. 32(b) for $\Delta_1 = 0.036$ and $\Delta_2 = -0.037$ shows, the EFM stability region is not affected by this transition. As a result, there are now three bands of the EFM surface and each of them features

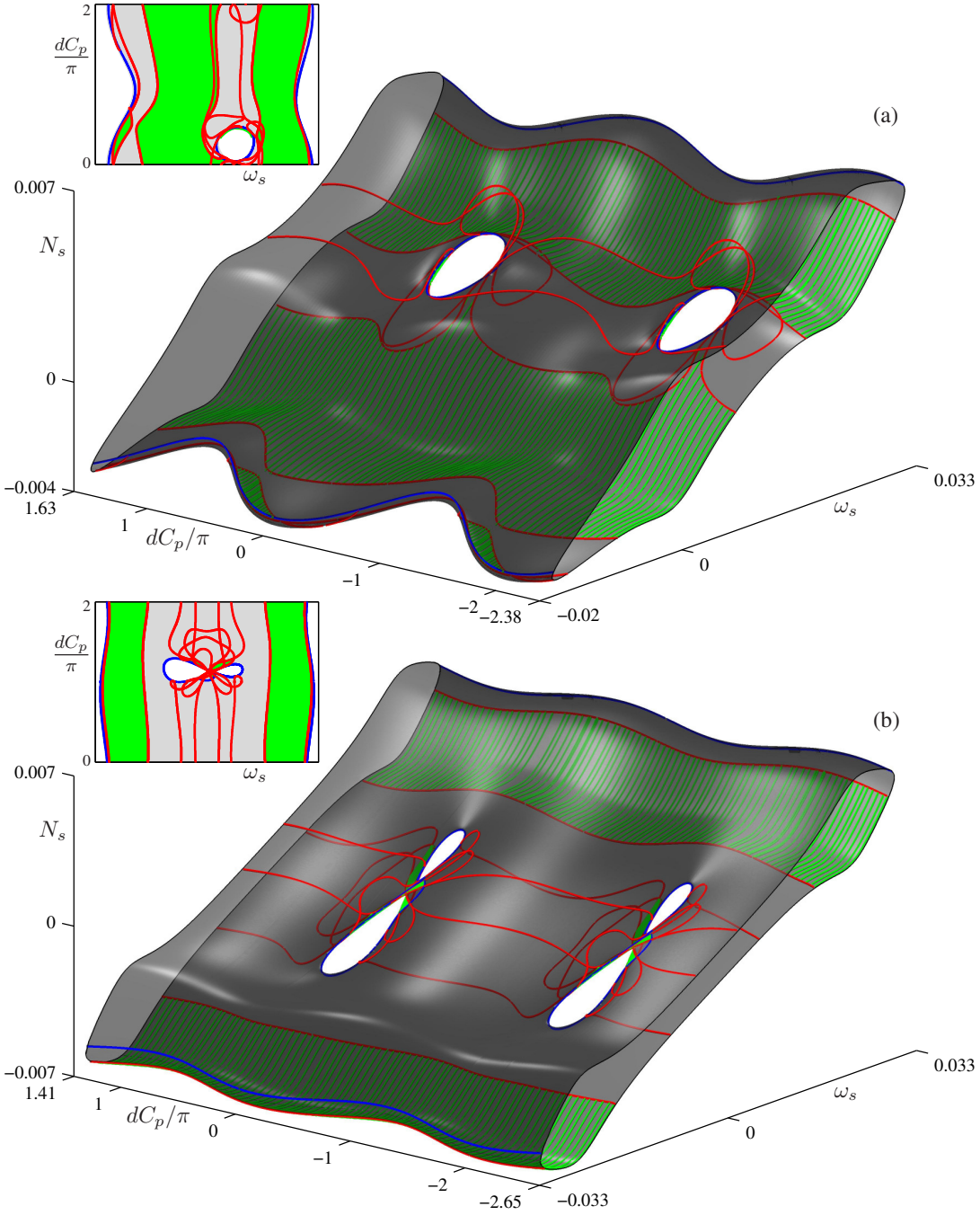

FIG. 30. *The EFM-surface with stability information, of type $\widehat{B}_h$ for $\Delta_1 = 0.024$ and $\Delta_2 = 0$ (a), and of type ${}_h\widehat{B}_h$ for $\Delta_1 = 0.024$ and $\Delta_2 = -0.025$ (b). Here $\kappa = 0.01$, $\Lambda = 0.005$ and $d\tau = 0$; curves and regions are coloured as in Fig. 28.*

a band of EFM stability. Notice that the central EFM-stability band has quite large holes around $(dC_p, \omega_s) = (2k\pi, 0)$.

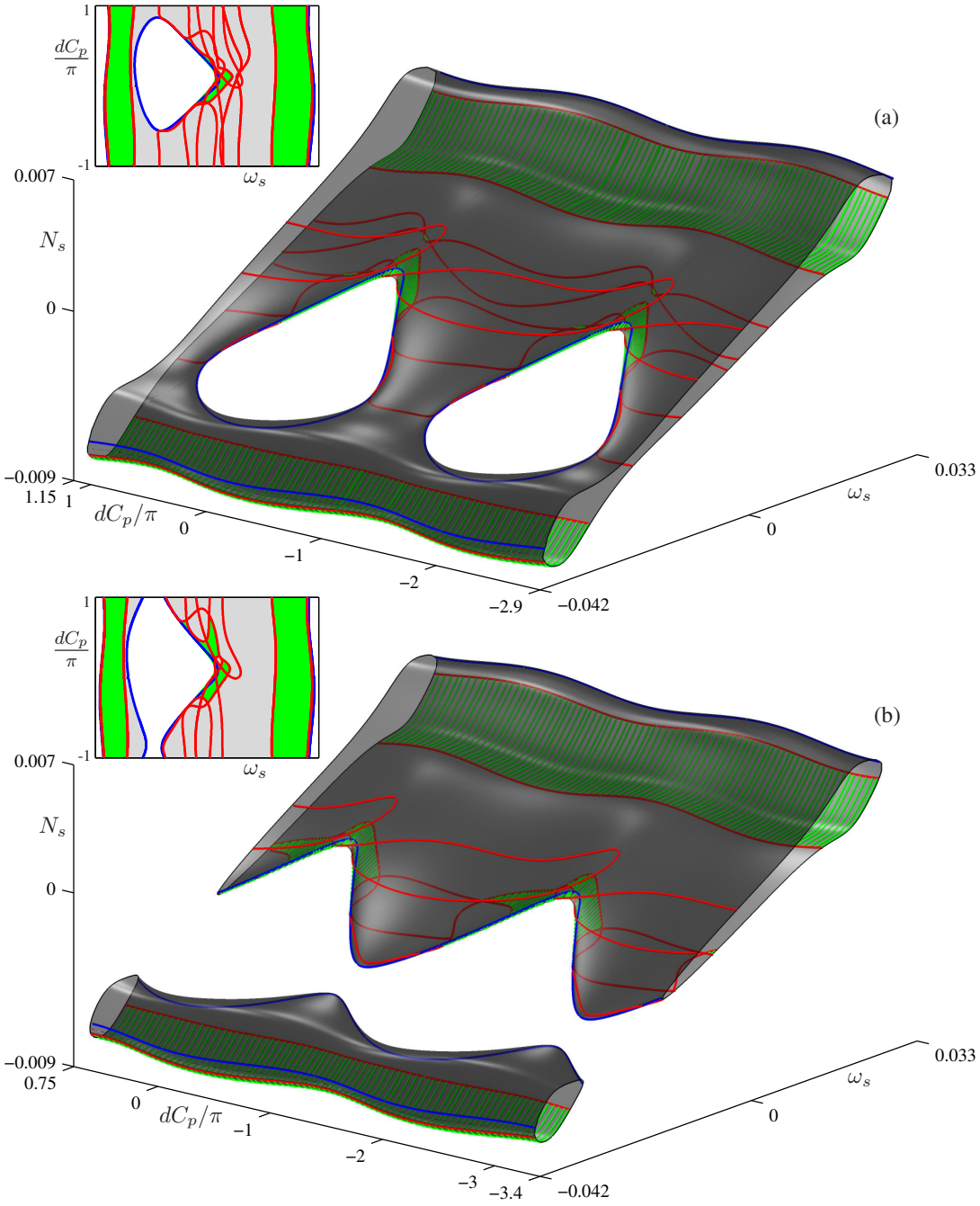

FIG. 31. *The EFM-surface with stability information, of type* ${}_h\widehat{B}$ *for* $\Delta_1 = 0.024$ *and* $\Delta_2 = -0.035$ *(a), and of type* $B\widehat{B}$ *for* $\Delta_1 = 0.024$ *and* $\Delta_2 = -0.037$ *(b). Here* $\kappa = 0.01$, $\Lambda = 0.005$ *and* $d\tau = 0$*; curves and regions are coloured as in Fig. 28.*

We now decrease Δ_2 to $\Delta_2 = -0.049$ and then increase Δ_1 so that EFM-surface undergoes saddle transitions S_C that lead to the creation of islands. Figure 33(a) shows the EFM-surface

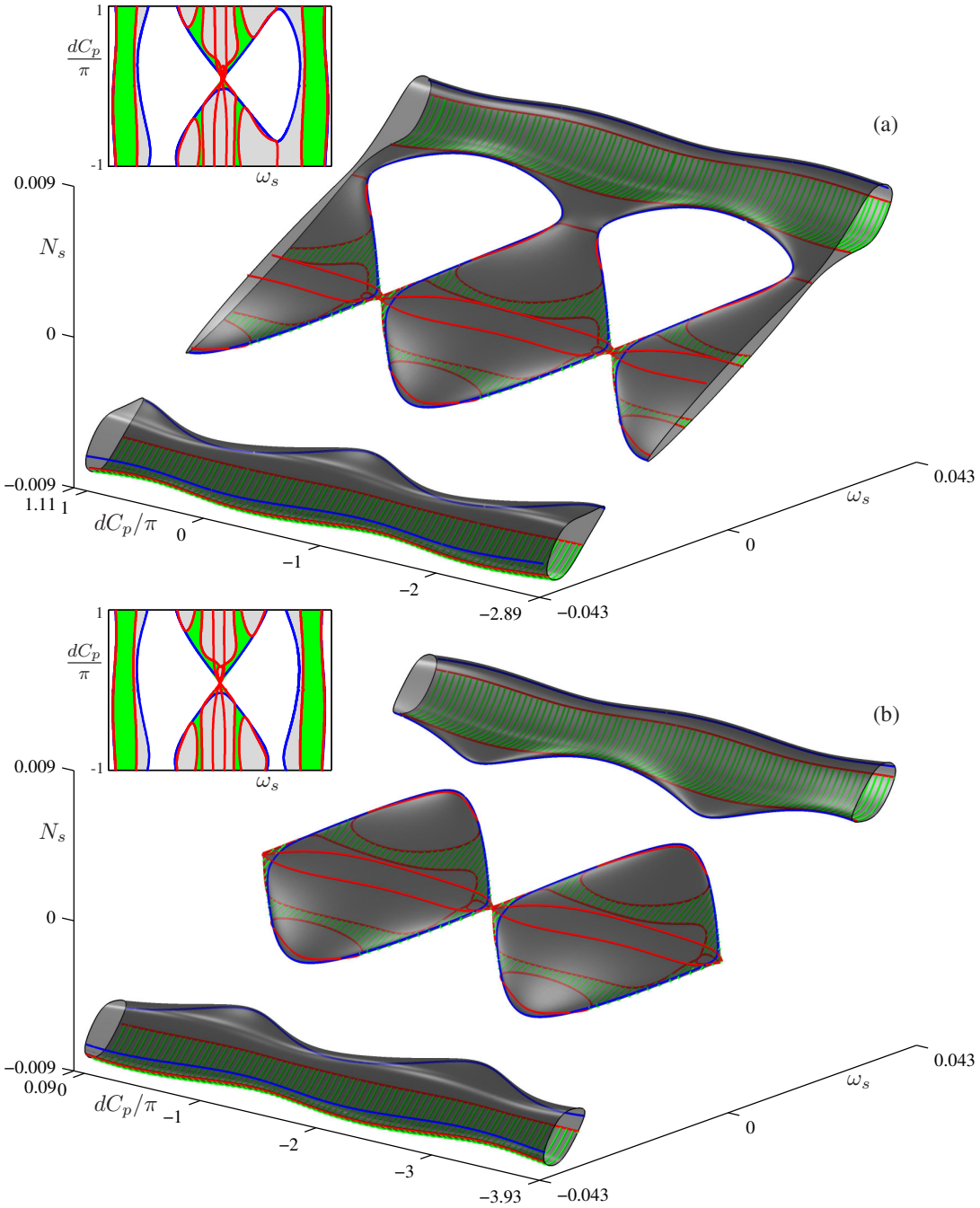

FIG. 32. *The EFM-surface with stability information, of type $B\widehat{B}_h$ for $\Delta_1 = 0.035$ and $\Delta_2 = -0.037$ (a), and of type $B\widehat{B}B$ for $\Delta_1 = 0.036$ and $\Delta_2 = -0.037$ (b). Here $\kappa = 0.01$, $\Lambda = 0.005$ and $d\tau = 0$; curves and regions are coloured as in Fig. 28.*

of type $I\widehat{B}B$ for $\Delta_1 = 0.044$. Notice that the EFM-stability region covers practically the entire (dC_p, ω_s)-range of the islands for negative ω_s. Similarly, the EFM-stability region covers practically

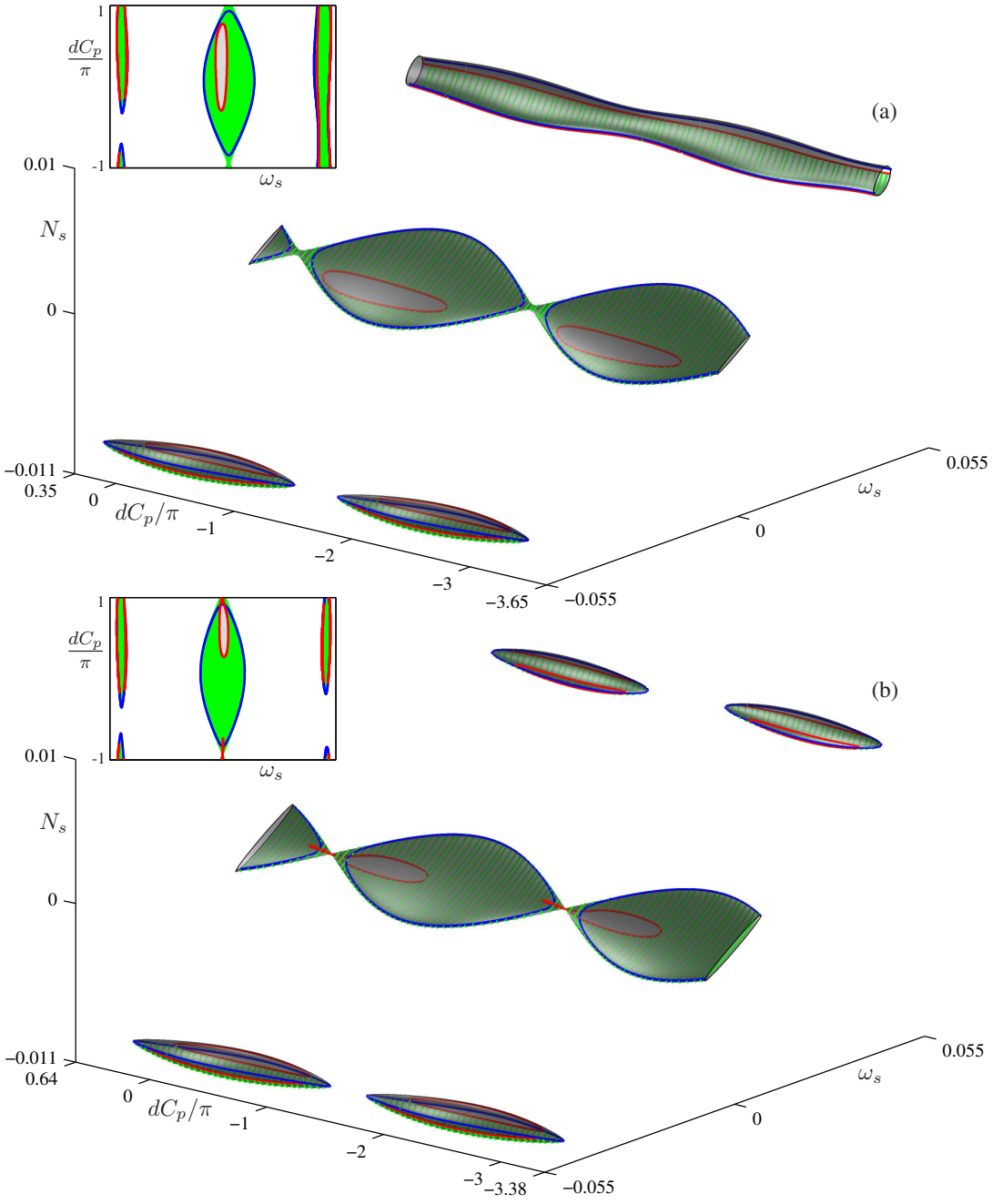

FIG. 33. *The EFM-surface with stability information, of type $I\widehat{B}B$ for $\Delta_1 = 0.044$ and $\Delta_2 = -0.049$ (a), and of type $I\widehat{B}I$ for $\Delta_1 = 0.050$ and $\Delta_2 = -0.049$ (b). Here $\kappa = 0.01$, $\Lambda = 0.005$ and $d\tau = 0$; curves and regions are coloured as in Fig. 28.*

the entire (dC_p, ω_s)-range of the band for positive ω_s. The central EFM-stability band, on the other hand, still features holes around $(dC_p, \omega_s) = (2k\pi, 0)$, but they are now considerably smaller when compared to Fig. 32(b). Moreover, near the narrow necks of the central component of the EFM-

surface the stable EFM region extends over the bottom as well as the top sheet of the EFM-surface. When Δ_1 is increased further the EFM-surface changes to type $I\widehat{B}I$, as in Fig. 33(a) for $\Delta_1 = 0.050$. Practically the entire (dC_p, ω_s)-range of the new islands for positive ω_s is again covered by the EFM-stability region. Notice that the other islands and the central band of EFM-stability are unaffected by this transition.

Overall we found EFM-stability regions for different detunings Δ_1 and Δ_2 whose characterizing features are so clearly distinguished that they may be identified experimentally. The EFM-stability regions agree with the properties of the EFM-surface type, but there is no one-to-one correspondence. More specifically, for the realistic and experimentally feasible feedback rate $\kappa = 0.01$ and filter width $\Lambda = 0.005$ we find for a 2FOF laser with two feedback loops of equal length ($d\tau = 0$) that the EFM-stability region's large-scale components are: a single central band, two bands, three bands, two bands with a string of islands, or a single central band with two strings of islands. Moreover, the central band of EFM-stability features holes that are often so large that they may be detectable.

6. The effect of a nonzero delay difference. So far we considered the EFM structure of the 2FOF laser only for the case that the two delay times are equal, that is, for a delay difference $d\tau = \tau_2 - \tau_1 = 0$. As the final part of our analysis of the dependence of EFM-surface and EFM stability regions on the filter and feedback loop parameters, we now discuss the effect of nonzero $d\tau = \tau_2 - \tau_1$, which we take to be positve without loss of generality.

Equation (4.1) for the boundary of the projection of the EFM-surface onto the (ω_s, dC_p)-plane expresses dC_p as a function of ω_s. In this equation the delay time difference $d\tau$ appears only as the coefficient of the linear term of ω_s; hence, a nonzero value of $d\tau$ introduces a shearing of the EFM-surface with shear of exactly $d\tau$.

This shearing of the EFM-surface can be made explicit for the special case that $\Delta_1 = \Delta_2$, while still considering a common filter width Λ. Namely, we can then define the center line of the projection of the EFM-surface as the line through the points where the inverse cosine term in (4.1) vanishes. The equation for this center line is then simply

$$dC_p(\omega_s) = -d\tau\omega_s, \tag{6.1}$$

which is the line with slope $d\tau$ through the origin of the (ω_s, dC_p)-plane. Since the ω_s-range of the EFM-surface does not change with $d\tau$, the shear is equal to the slope of the center line of the projection of the EFM-surface.

We conclude that an EFM-surface for $d\tau \neq 0$ can be obtained by considering the corresponding EFM-surface for $d\tau = 0$ and applying a shear of $d\tau$. As a result of this shearing, EFM-components may be present for $d\tau \neq 0$ that are not present for $d\tau = 0$. Figure 34 illustrates this effect with the example of the EFM-surface in (ω_s, N_s, dC_p)-space for $\Delta_1 = \Delta_2 = 0$ and $\Lambda = 0.005$ with $\tau_1 = 500$ and $\tau_2 = 850$, so that the shear is $d\tau = 350$. Note that this EFM-surface is the sheared version of the corresponding EFM-surface for $d\tau = 0$ in Fig. 28 (b), which is of type $\widehat{B}$. The EFM-surface in Fig. 34 still consists of all 2π-translates of a basic unit, which are connected at the points where $dC_p = \pi + 2k\pi$ for $k \in \mathbb{Z}$; however, now the basic unit of the EFM-surface extends over a dC_p-range of more than 2π. While there is always a single EFM-component for any value of dC_p for the case that $d\tau = 0$, due to the shear for $d\tau = 350$, we now find up to three EFM-components in Fig. 34. Each of those EFM-components belongs to a different 2π-translated copy of the basic unit of the EFM-surface. Physically, this is due to beating between two frequencies that are associated with the two feedback loops of different round trip times; see Eqs. (3.2)–(3.4).

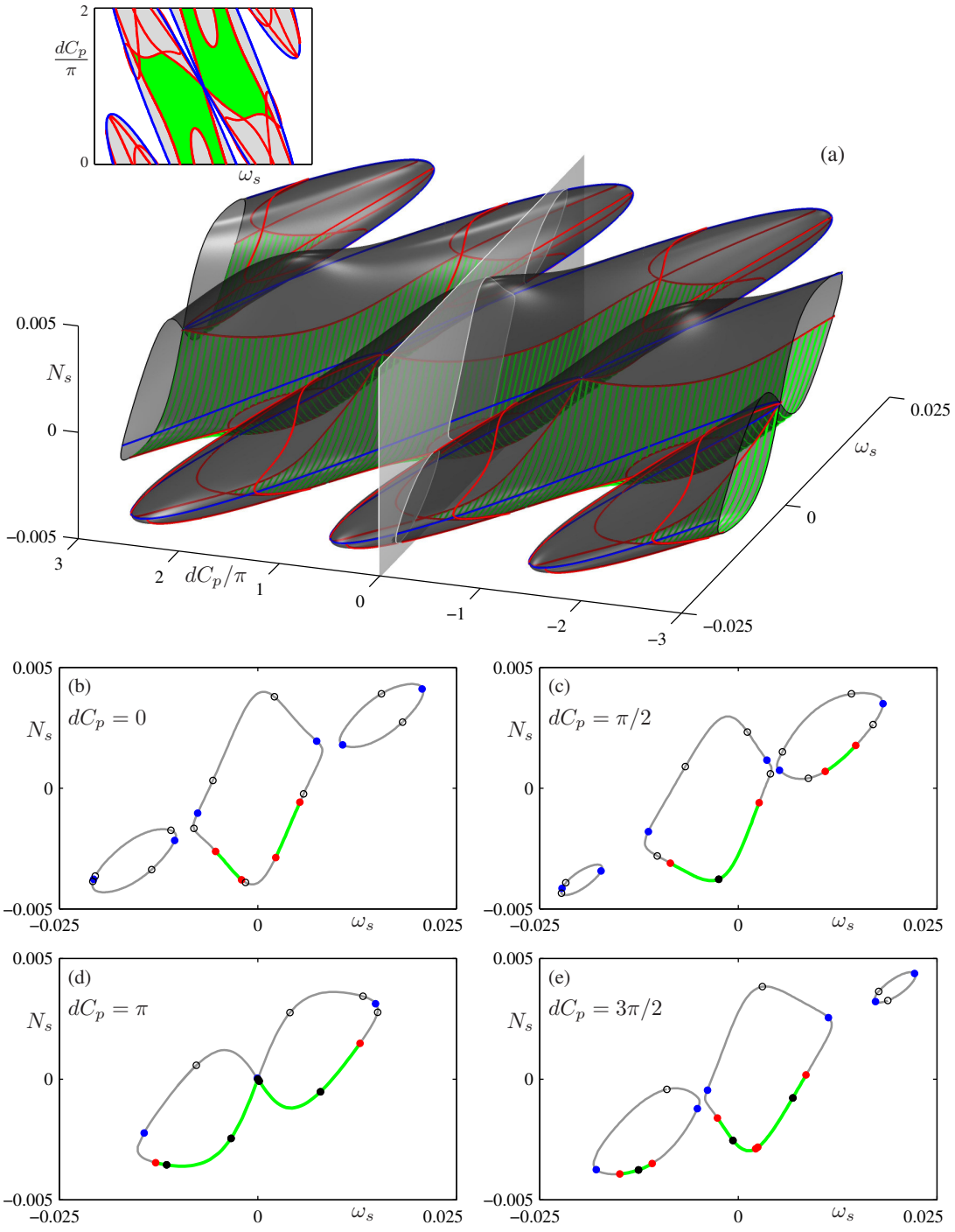

FIG. 34. *Panel (a) shows the EFM-surface with stability information for* $\kappa = 0.01$, $\Delta_1 = \Delta_2 = 0$, $\Lambda = 0.005$, $\tau_1 = 500$ *and* $\tau_2 = 850$ *so that* $d\tau = 350$, *and its intersection with the grey plane defined by* $dC_p = 0$*; compare with Fig. 4. Curves and regions are coloured as in Fig. 28. Panels (b)–(e) show the EFM-components for different values of* dC_p *(as indicated in the panels); stable segments of the EFM-components (green) are bounded by the Hopf bifurcations (red dots) or by the saddle-node bifurcation (blue dots). The actual stable EFMs for* $C_p^1 = 0$ *are the black full circles; open circles are unstable EFMs.*

As is shown in Fig. 34 (b)–(e), the exact number of EFM-components depends on the value of dC_p. More specifically, for $dC_p = 0$ there are three EFM-components, owing to the fact that the corresponding plane in (ω_s, N_s, dC_p)-space intersects three copies of the basic unit of the EFM-surface; see Fig. 34 (a) and (b). As dC_p is changed the EFM-components change. For $dC_p = \pi/2$ as in panel (c), there are still three EFM-components (the right and central EFM-components are not connected), and the left-most has become smaller and the right-most larger. When dC_p is increased further, the left-most EFM-component disappears (in a minimax transition when the plane $dC_p = const$ passes through the end point of the respective part of the EFM-surface). For $dC_p = \pi$ as in Fig. 34 (d), the two remaining EFM-components connect at the origin of the (ω_s, N_s)-plane to form a single EFM-component in the shape of a figure eight. We remark that, because for $dC_p = \pi$ equation (3.9) is equal to 0 at $\omega_s = 0$, this case for the 2FOF laser corresponds to the single-FOF laser described in [67] where the laser is resonant with the peak of the Fabry-Pérot filter transmittance profile. The single EFM-component then splits up again into two EFM-components for $dC_p > \pi$. A new EFM-component appears (again in a minimax transition) on the right, that is, for positive ω_s, so that there are again three EFM-components; see Fig. 34 (e) for $dC_p = 3\pi/2$.

Since the detunings of both filters are equal, the EFM-surface in Fig. 34 (a) is invariant under the anti-diagonal symmetry operation $(\omega_s, dC_p, N_s) \mapsto (-\omega_s, -dC_p, -N_s)$. As a result, panel (b) and (d) are invariant under rotation over π of the (ω_s, N_s)-plane, while panels (c) and (e) are symmetric counterparts.

Figure 34 (a) shows that the EFM-stability region is sheared concurrently with the EFM-surface. Stable regions of different 2π-translated copies of the basic unit of the EFM-surface coexist for chosen fixed dC_p. Hence, as is illustrated in Fig. 34 (b)–(e), one may find stable segments on any of the EFM-components. In fact, the actual number of stable EFMs — the full black circles within the green segments — strongly depends on the feedback phases. For example, in Fig. 34 (b) for $C_p^1 = 0$ and $dC_p = 0$ there is no actual stable EFM in the green segments, while in panel (e) for $C_p^1 = 0$ and $dC_p = 3\pi/2$ a stable EFM exists in each of the stable segments of the EFM-components.

Any number of EFM-components can be found for sufficiently large $d\tau$. Figure 35 illustrates this for the EFM-surface of type $\widehat{B}$ from Fig. 34 with up to five EFM-components for $d\tau = 700$ in panel (a) and up to seven for $d\tau = 1000$ in panel (b). Here the effect of shearing of the EFM-surface is illustrated with the (ω_s, dC_p)-projection of the EFM-surface (left column) and by showing the respective EFM-components in the (ω_s, N_s)-plane for $dC_p = 0$ (right column). Moreover, Fig. 35 shows that the shearing of the EFM-surface results in the possibility of finding an arbitrary number of bands of stable EFMs — stable EFM regions extending over the fundamental 2π dC_p-range — in the (ω_s, dC_p)-plane. Such stable EFM bands translate to an arbitrary number of stable segments of the EFM-components for any value of fixed dC_p. Note that the EFM-stability region in Fig. 35 (a1) and (b1) it is not simply a sheared version of the stability region for $d\tau = 0$. Rather, its outer boundary changes, so that it extends over a wider and wider range of ω_s. The hole of the EFM-stability region surrounding the points $(\omega_s, dC_p) = (0, 2n\pi)$ with $n \in \mathbb{Z}$, on the other hand, does not appear to change much apart from being sheared; compare with Fig. 28.

We finish this section by showing in Fig. 36 the effect of shearing the more complicated EFM-surface of type $B\widehat{B}_h$ for $\Delta_1 = 0.035$ and $\Delta_2 = -0.037$. Panels (a1) and (b1) shows the (ω_s, dC_p)-projection of the EFM-surface and panels (a2) and (b2) the EFM-components in the (ω_s, N_s)-plane for $dC_p = -0.5\pi$. Note that panel (a) for $d\tau = 0$ is for the EFM-surface of Fig. 32 (a), which may give rise to up to three EFM-components. However, when it is sheared with a sheer of $d\tau = 500$ one may find up to seven EFM-components; see Fig. 36 (b1) and (b2). Note that this increase in the number of possible EFM-components is due to the shearing of the undulating boundary of the bands, as well as to the shearing of the hole, which now extend over a dC_p-range of more than 2π. Moreover, Fig. 36 (a2) and (b2) indicates high level of multistability. Notice that the outer EFM-stability bands for $d\tau = 500$ are effectively sheared versions of the outer EFM-stability bands

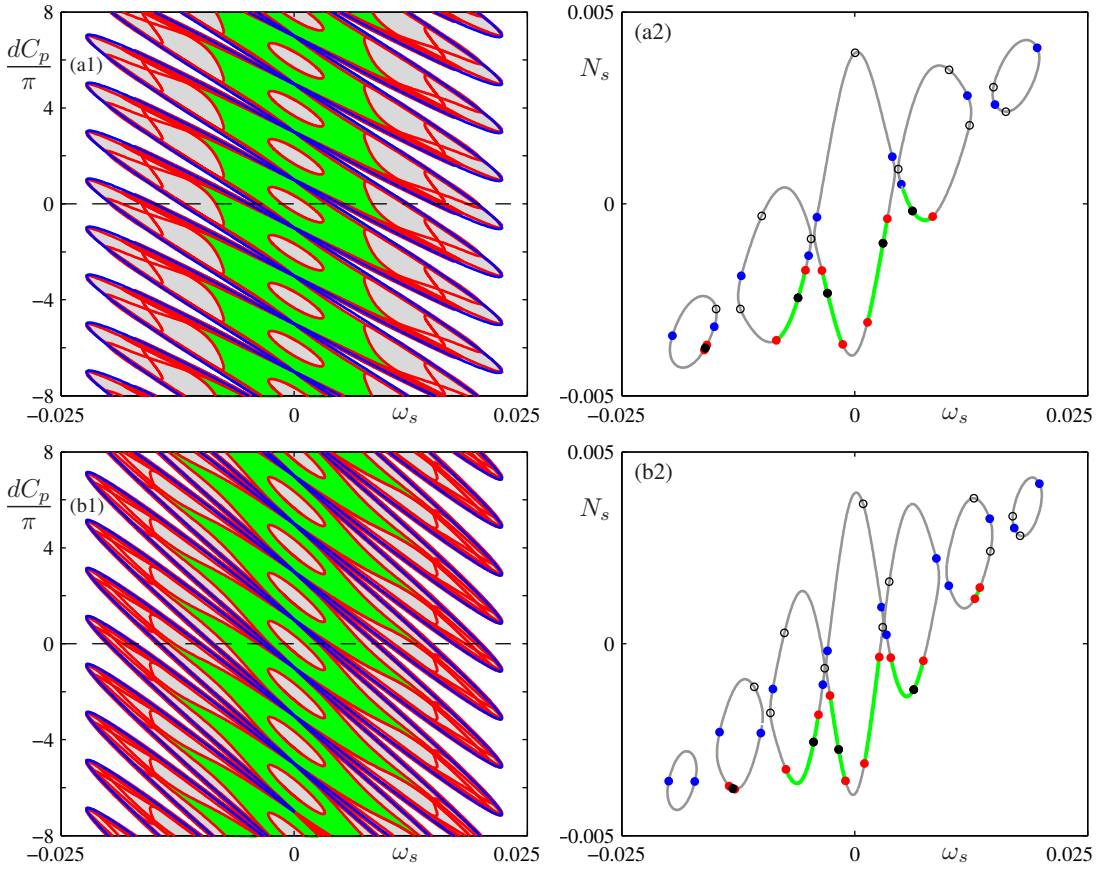

FIG. 35. *The (ω_s, dC_p)-projection of the EFM-surface for $d\tau = 700$ (a1), and for $d\tau = 1000$ (b1). Here $\kappa = 0.01$, $\Delta_1 = Delta_2 = 0$, $\Lambda = 0.005$, and $\tau_1 = 500$. Curves and regions are coloured as in Fig. 28. Panels (a2) and (b2) the EFM-components for $dC_p = 0$ with actual EFMs for $C_p^1 = 1.7\pi$ (a2) and for $C_p^1 = 0.7\pi$ (a2); curves and points are coloured as in Fig. 34.*

for $d\tau = 0$. The central region of EFM-stability, on the other hand, does not simply shear, but there are some additional changes to its boundary. As in Fig. 35, we find a larger central region of EFM-stability in Fig. 36 (b1).

In conclusion, the shearing due to nonzero $d\tau$ is an effect that is independent of the changes of the geometry and topology of the EFM-surface due to variation of the other parameters that characterize the filter loops. Indeed, to find the EFM-surface of the 2FOF laser with two different delay times, it is sufficient to find the respective EFM-surface for $d\tau = 0$ and then consider its shearing with the shear $d\tau$. This justifies our choice in Sec. 4 to classify the EFM surface for $d\tau = 0$. When it comes to the regions of EFM stability, the effect of shearing is more subtle, as it may lead to some changes of EFM-stability boundaries. Nevertheless, in first approximation the EFM-stability region on the sheared EFM-surface is 'near' the sheared EFM-stability region. In fact, for the examples we considered, the EFM-stability region on the sheared EFM-surface increases slightly with $d\tau$. We therefore suggest that the EFM-stability results for $d\tau = 0$ in Sec. 5 give a good indication of the expected EFM-stability for $d\tau \neq 0$. In particular, for sufficiently large $d\tau$ one may find, for given fixed dC_p, any number of EFM-components with segments of stable EFMs.

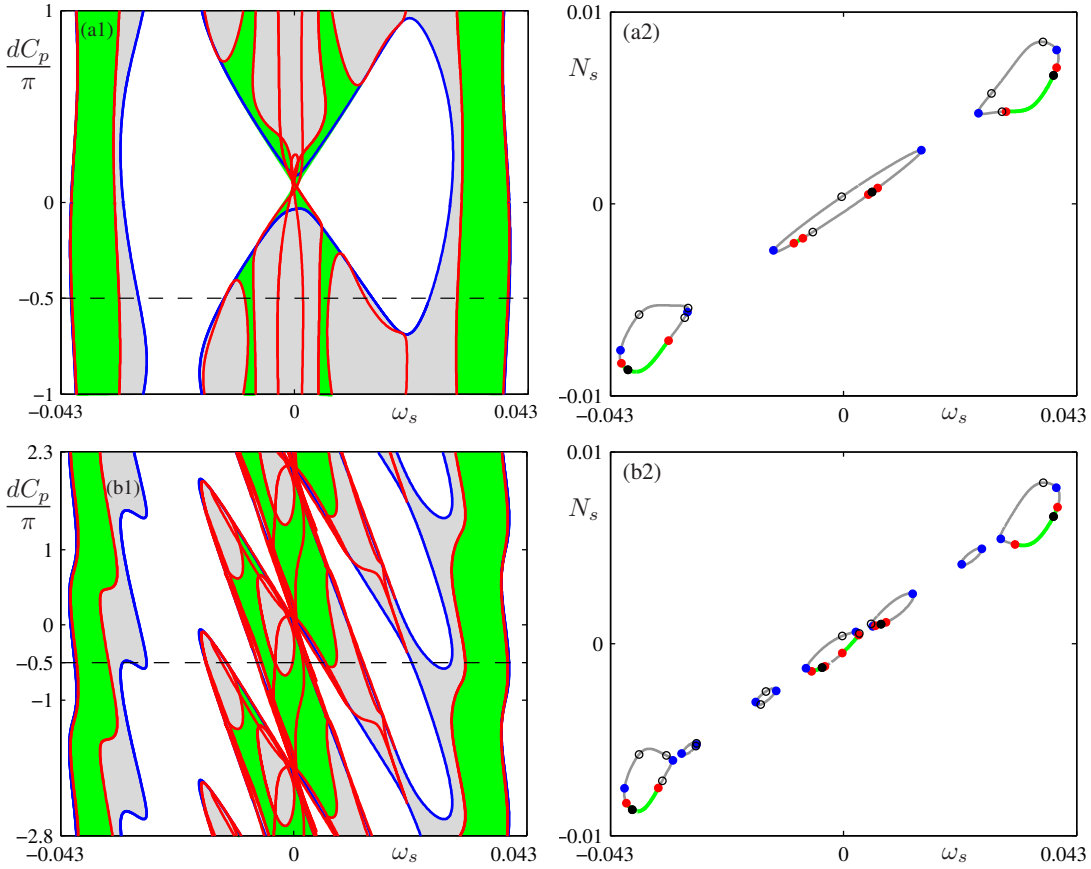

FIG. 36. *The (ω_s, dC_p)-projection of the EFM-surface of type ${}_h\widehat{B}B$ for $d\tau = 0$ (a1), and the corresponding sheared EFM-surface for $d\tau = 500$ (b1). Here $\kappa = 0.01$, $\Delta_1 = 0.035$, $\Delta_2 = -0.037$, $\Lambda = 0.005$, and $\tau_1 = 500$. Curves and regions are coloured as in Fig. 28. Projection in panel (a1) correspond to the EFM-surface in Fig. 30. Panels (a2) and (b2) show relevant EFM-components for $dC_p = -0.5\pi$ with actual EFMs for $C_p^1 = 2.7\pi$; curves and points are coloured as in Fig. 34.*

7. Conclusions. We presented a comprehensive study of how the external filtered modes of the 2FOF laser depend on the parameters that characterize the two filtered feedback loops. This study was motivated by the application of this laser system as a pump laser for optical communication systems and as a light source for sensor applications. The general idea behind the 2FOF laser is that the second feedback loop provides additional control over the laser's output with the ultimate goal of stable operation. This is why our analysis focused on the EFMs, which physically correspond to constant-intensity monochromatic laser output.

Mathematically, the EFMs are solutions of the governing delay differential equation with steady population inversion N_s, steady amplitudes of the electric fields of the laser and of the two filters, and a constant lasing frequency ω_s. The well established way of analysing the structure of the solutions of the single-FOF laser is the investigation of its EFM-components, which are closed curves of EFMs in the (ω_s, N_s)-plane that are traced out with a changing phase of the feedback field. The relevance of the EFM-components is that they correspond to the disjoint ω_s frequency ranges that are available for stable laser operation. For the 2FOF laser one also finds EFM-components, but now they depend on the difference dC_p between the feedback phases of the two filtered fields.

In other words, the number and nature of the EFM-components for the 2FOF laser depends on additional parameters, in particular, on dC_p and the difference $d\tau$ between the two delay times. This motivated us to consider the EFM-surface in (ω_s, N_s, dC_p)-space as the key object of study. This point of view provided a useful framework for the analysis of how the structure and stability of the EFMs of the 2FOF laser depends on the different parameters of the two feedback loops.

Importantly, we found that the influence of the difference $d\tau$ between the two delay times of the filters is a simple shearing of the EFM-surface for $d\tau = 0$. This allowed us to classify the possible types of EFM-surface in dependence on the filter detunings Δ_1 and Δ_2 and the common filter width Λ. More specifically, we distinguished five different mechanisms through which the EFM-surface can change locally: four singularity transitions and a cubic tangency of the EFM-surface with respect to a plane $dC_p = const.$ This choice was motivated by the fact that these transitions change the number of EFM components one encounters in different slices of fixed dC_p. We presented the EFM-surface bifurcation diagram in the (Δ_1, Δ_2)-plane, which consists of open regions corresponding to different types of the EFM-surface, bounded by the loci of the five transitions between them. Moreover, we showed how the EFM-surface bifurcation diagram in the (Δ_1, Δ_2)-plane changes with the common filter width Λ, and presented the comprehensive list of 32 representative EFM-surface types. The different EFM-surface types are characterized by a certain number of bands, with or without holes, that extend over the entire dC_p-range, and islands that extend only over a bounded dC_p-range.

We also performed a limited study of the stability of the EFMs, which showed that important features of the EFM surface are reflected in the properties of the regions of EFM-stability on the EFM surface. While there is no one-to-one correspondence between the EFM surface type and the nature of the EFM-stability regions on it, nevertheless, it is possible to find different constellations of stability regions in the form of bands and islands that are losely associated with the EFM surface type. The stability boundaries of the EFM-stability regions are formed by curves of saddle-node and Hopf bifurcations. As parameters change, these boundary curves undergo complicated transitions when passing through codimension-three bifurcations (degenerate Bogdanov-Takens and degenerate saddle-node-Hopf points), as well as through saddle points and extrema in the surface of Hopf bifurcations (in the respective three-dimensional parameter space). Similar changes of the boundary of stable EFMs have also been found in the single-FOF laser [17, 27]. Studying them in more detail for the 2FOF laser would be quite a task.

From a conceptual point of view, the influence of the two filter loops on the laser can be thought of as the feedback from a single feedback loop with a complicated filter profile. This effective filter profile is generated by the interference between the two filter fields and it consists of a pattern of maxima and minima of the transmittance as a function of the frequency of the light. This point of view provides a connection to studies that considered the output of a laser subject to feedback from a non-Lorentzian, more complicated (that is, non-Lorentzian) filter profile, such as the periodic filter profiles studied in [51, 67]. In [67] feedback from a Fabry-Pérot cavity is considered but it is not restricted to being very close to the transmittance maximum, but rather provides feedback over a large spectral range that encompasses several maxima and minima of the transmittance. In [51], on the other hand, filtered feedback with several maxima and minima of the transmittance arise due to side "bumps" of a fibre Bragg grating filter profile. We found that the observed EFM structure in [51] and [67] corresponds in the 2FOF laser to a change from constructive to destructive interference between the two filter fields for $d\tau \neq 0$ via a variation of the filter phase difference dC_p. Furthermore, we showed that the 2FOF laser has non-obvious connections with other laser systems with optical feedback. The 2FOF laser reduces to the single-FOF laser for $\Delta_1 = \Delta_2$. Moreover, for sufficiently large filter width Λ the 2FOF laser becomes a 2COF laser with two conventional optical feedback loops. It is also possible to increase the width of only one of the filters, and this will result in a laser system with FOF and COF branches. A further analysis of the connections

between the 2FOF laser and feedback from other types of filters is an interesting subject for future research.

A logical next step in the analysis of the 2FOF laser would be to perform a numerical bifurcation study into stable oscillations that may arise from the Hopf bifurcations that bound the EFM-stability regions. Any semiconductor laser with external input or feedback may display a type of oscillation, known as relaxation oscillations, where the electric field and the inversion exchange energy periodically at a frequency of a few gigaHertz. Moreover, a laser with FOF may also display so-called frequency oscillations, where the frequency of the light oscillates while its amplitude remains virtually constant [24]. In light of the strong amplitude-phase coupling given by nonzero α, this type of oscillation is quite surprising and it has been attributed to dynamics involving the flanks of the filter transmittance profile [16]. Given the complexity of the EFM-surface types and the associated EFM-stability regions, it appears more feasible to perform a targeted study into oscillating output of the 2FOF laser in a region of parameter space of interest, for example, as suggested by an actual experiment.

An experimental investigation of the EFM structure of the 2FOF laser remains a very interesting challenge indeed. Measurements of the EFM-components of the single-FOF laser have been performed in [19] for a laser with a single open air (unidirectional) feedback loop with a Fabry-Pérot filter, and an experiment with a second Fabry-Pérot feedback loop has been implemented recently in [54]. In such an experiment, stable EFMs manifest themselves as plateaux of the feedback intensity (where a different feedback intensity also means a different frequency ω_s of the laser light). Our theoretical investigation showed that the bands and islands of EFM-stability may be quite wide in the ω_s-direction. Therefore, it may be feasible to follow a stable EFM experimentally by varying dC_p to determine whether it exists over an entire period of 2π or not. In this way, it might be possible to identify and distinguish experimentally some types of EFM-stability regions in terms of their numbers of stability bands and islands.

REFERENCES

[1] V.I. Arnold, *The theory of singularities and its applications*, Accademia Nazionale dei Lincei, Pisa, 1993.

[2] A. Asok, *About the cover: the mathematics imagery of Lun-Yi Tsai*, Bulletin of the AMS, 47(4) (2010), pp 695–697.

[3] J. Chen, X. Wu, J. Ge, A. Hermerschmidt, and H. J. Eichler, *Broad-are laser diode with 0.02 nm bandwidth and diffraction limited output due to double external cavity feedback*, Appl. Phys. Lett., 85(4) (2004), pp 1104–1106.

[4] M. Chi, N-S. Bogh, B. Thestrup, and P. M. Petersen, *Improvement of the beam quality of a broad-area diode laser using double feedback from two external mirrors*, Appl. Phys. Lett., 85 (2004), pp 1107–1109.

[5] J. S. Cohen, R. R. Drenten, and B. H. Verbeeck, *The effect of optical feedback on the relaxation oscillation in semiconductor lasers*, IEEE J. Quantum Electron., 24 (1988), pp. 1989–1995.

[6] B. Dahmani, L. Hollberg, and R. Drullinger, *Frequency stabilization of semiconductor lasers by resonant optical feedback*, Opt. Lett., 12 (1987), pp. 876–878.

[7] D. H. DeTienne, G. R. Gray, G. P. Agrawal, and D. Lenstra, *Semiconductor laser dynamics for feedback from a finite-penetration-depth phase-conjugate mirror*, IEEE J. Quantum Electron., 33 (1997), pp. 838–844.

[8] O. Diekmann, S. A. van Gils, S. M. Verduyn Lunel, and H.-O. Walther, *Delay Equations: Functional-, Complex- and Nonlinear Analysis*, Springer-Verlag, New York, 1995.

[9] B. Docter, J. Pozo, S. Beri, I. V. Ermakov, J. Danckaert, M. K. Smit, and F. Karouta, *Discretely tunable laser based on filtered feedback for telecommunication applications*, IEEE J. Sel. Topics Qunat. Electronics, 16(5) (2010), pp. 1405–1412.

[10] F. Dumortier, R. Roussarie, J. Sotomayor, and H. Zoladek, *Bifurcations of Planar Vector Fields. Nilpotent Singularities and Abelian Integrals*, Lecture Notes in Math. 1480, Springer-Verlag, Berlin, 1991.

[11] K. Engelborghs, T. Luyzanina, and G. Samaey, DDE-Biftool *v. 2.00 user manual: A Matlab package for bifurcation analysis of delay differential equations*, Tech. report tw-330, Department of Computer Science, K. U. Leuven, 2001.

[12] K. Engelborghs, T. Luzyanina, and D. Roose, *Numerical bifurcation analysis of delay differential equations using DDE-BIFTOOL*, ACM Transactions on Mathematical Software, 28 (2002), pp. 1–21.

[13] I. V.. Ermakov, V. Z. Tronciu, P. Colet, and C. R. Mirasso, *Controlling the unstable emission of a semiconductor laser subject to conventional optical feedback with a filtered feedback branch*, Optics Express, 17(11) (2009), pp. 8749–8755.
[14] T. Erneux, A. Gavrielides, K. Green, and B. Krauskopf, *External cavity modes of semiconductor lasers with phase-conjugate feedback*, Phys. Rev. E, 68 (2003), p. 066205.
[15] T. Erneux, M. Yousefi, and D. Lenstra, *The injection laser limit of lasers subject to filtered optical feedback*, in Proc. European Quantum Electronics Conf., 2003.
[16] H. Erzgräber and B. Krauskopf, *Dynamics of a filtered-feedback laser: influence of the filter width*, Optics Letters, 32 (2007), pp. 2441–2443.
[17] H. Erzgräber, B. Krauskopf, and D. Lenstra, *Bifurcation analysis of a semiconductor laser with filtered optical feedback*, SIAM J. Appl. Dyn. Sys., 6 (2007), pp. 1–28.
[18] H. Erzgräber, B. Krauskopf, D. Lenstra, A. P. A. Fischer, and G. Vemuri, *Frequency versus relaxation oscillations in semiconductor laser with coherent filtered optical feedback*, Phys. Rev. E, 73, (2006), p. 055201(R).
[19] H. Erzgräber, D. Lenstra, B. Krauskopf, A. P. A. Fischer, and G. Vemuri, *Feedback phase sensitivity of a semiconductor laser subject to filtered optical feedback: experiment and theory*, Phys. Rev. E, 76 (2007), p. 026212.
[20] B. Farias, T. P. de Silans, M. Chevrollier, and M. Oriá, *Frequency bistability of a semiconductor laser under a frequency-dependent feedback*, Phys. Rev. Lett., 94 (2005), p. 173902.
[21] S. G. Fischer, M. Ahmed, T. Okamoto, W. Ishimori, and M. Yamada, *An improved analysis of semiconductor laser dynamics under strong optical feedback*, IEEE J. Quantum Electron., 9 (2003), pp. 1265–1274.
[22] A. P. A. Fischer, O. Andersen, M. Yousefi, S. Stolte, and D. Lenstra, *Experimental and theoretical study of semiconductor laser dynamics due to filtered optical feedback*, IEEE J. Quantum Electron., 36 (2000), pp. 375–384.
[23] A. P. A. Fischer, M. Yousefi, D. Lenstra, M. Carter, and G. Vemuri, *Experimental and theoretical study of semiconductor laser dynamics due to filtered optical feedback*, IEEE J. Sel. Top. Quantum Electron., 10 (2004), pp. 944–954.
[24] A. Fischer, M. Yousefi, D. Lenstra, M. Carter, and G. Vemuri, *Filtered optical feedback induced frequency dynamics in semiconductor lasers*, Phys. Rev. Lett., 92 (2004), p. 023901
[25] I. Fischer, G. H. M. van Tartwijk, A. M. Levine, W. Elsässer, E. Göbel, and D. Lenstra, *Fast pulsing and chaotic itinerancy with a drift in the coherence collapse of semiconductor lasers*, Phys. Rev. Lett., 76 (1996), pp. 220–223.
[26] M. Golubitsky and D. G. Schaeffer, *Singularities and Groups in Bifurcation Theory*, volume 1, Springer-Verlag, 1985.
[27] K. Green and B. Krauskopf, *Bifurcation analysis of a semiconductor laser subject to non-instantaneous phase-conjugate feedback*, Opt. Commun., 231 (2004), pp. 383–393.
[28] K. Green and B. Krauskopf, *Mode structure of a semiconductor laser subject to filtered optical feedback*, Opt. Commun., 258 (2006), pp. 243–255.
[29] B. Haegeman, K. Engelborghs, D. Roose, D. Pieroux, and T. Erneux, *Stability and rupture of bifurcation bridges in semiconductor lasers subject to optical feedback*, Phys. Rev. E, 66 (2002), p. 046216.
[30] T. Heil, I. Fischer, W. Elsässer, B. Krauskopf, K. Green, and A. Gavrielides, *Delay dynamics of semiconductor lasers with short external cavities: Bifurcation scenarios and mechanisms*, Phys. Rev. E, 67 (2003), p. 066214.
[31] G. Hek and V. Rottschäfer, *Semiconductor laser with filtered optical feedback: from optical injection to conventional feedback*, IMA J. Appl. Math., 72 (2007), pp. 420–450.
[32] C. Henry, *Theory of the linewidth of semiconductor lasers*, IEEE J. Quantum Electron., 18 (1982), pp. 259–264.
[33] D. M. Kane and K. A. Shore (Eds.), *Unlocking Dynamical Diversity: Optical Feedback Effects on Semiconductor Lasers*, Wiley, 2005.
[34] B. Krauskopf, *Bifurcation analysis of lasers with delay*, in *Unlocking Dynamical Diversity: Optical Feedback Effects on Semiconductor Lasers*, D. Kane and K. Shore, eds., pp. 147–183, Wiley, 2005.
[35] B. Krauskopf, H. Erzgräber, and D. Lenstra, *Dynamics of semiconductor lasers with filtered optical feedback*, in *Semiconductor Lasers and Laser Dynamics II*, D. Lenstra, M. Pessa and I. H. White, eds., Proceedings of SPIE 6184, 61840V, 2006.
[36] B. Krauskopf and C. Rousseau, *Codimension-three unfoldings of reflectionally symmetric planar vector fields*, Nonlinearity, 10 (1997), pp. 1115–1150.
[37] B. Krauskopf, G.R. Gray, and D. Lenstra, *Semiconductor laser with phase-conjugate feedback: Dynamics and bifurcations*, Phys. Rev. E, 58 (1998), pp. 7190–7197.
[38] B. Krauskopf and D. Lenstra (Eds.), *Fundamental Issues of Nonlinear Laser Dynamics*, AIP Conference Proceedings 548, AIP, Melville, New York, 2000.
[39] B. Krauskopf, H. Osinga, and J. Galán-Vioque, eds., *Numerical Continuation Methods for Dynamical Systems, Pathfollowing and boundary value problems*, Springer, Dordrecht, 2007.

[40] B. Krauskopf, G. H. M. van Tartwijk, and G. R. Gray, *Symmetry properties of lasers subject to optical feedback*, Opt. Commun., 177 (2006), pp. 347–353.
[41] B. Krauskopf, C. M. Lee, and H. Osinga, *Codimension-one tangency bifurcations of global Poincaré maps of four-dimensional vector fields*, Nonlinearity, 22 (2009), pp. 1091–1121.
[42] Yu. A. Kuznetsov, Elements of Applied Bifurcation Theory, Springer-Verlag, New York, 1995.
[43] R. Lang and K. Kobayashi, *External optical feedback effects on semiconductor injection laser properties*, IEEE J. Quantum Electron., 16 (1980), pp. 347–355.
[44] L. Larger, P.-A. Lacourt, S. Poinsot, and M. Hanna, *From flow to map in an experimental high-dimensional electro-optic nonlinear delay oscillator*, Phys. Rev. Lett., 95 (2005), p. 043903.
[45] D. Lenstra, M. Van Vaalen, and B. Jaskorzyńska, *On the theory of a single-mode laser with weak optical feedback* , Physica B+C, 125 (1984), pp. 255–264.
[46] D. Lenstra and M. Yousefi, *Theory of delayed optical feedback in lasers*, in *Fundamental Issues of Nonlinear Laser Dynamics*, B. Krauskopf and D. Lenstra, eds., AIP Conference Proceedings 548, pp. 87–111, AIP, Melville, New York, 2000.
[47] A. M. Levine, G. H. M. van Tartwijk, D. Lenstra, and T. Erneux, *Diode lasers with optical feedback: Stability of the maximum gain mode*, Phys. Rev. A 52 (1995), R3436–R3439.
[48] K. Lüdge (Ed.), *Nonlinear laser Dynamics: From Quantum Dots to Cryptography.* Wiley-VCH, 2012.
[49] B. E. Martínez-Zérega, R. Jaimes-Reategui, A. N. Pisarchik, and J. M. Liu, *Experimental study of self-oscillation frequency in a semiconductor laser with optical injection*, J. Phys.: Conf. Ser., 23 (2005), pp. 62–67.
[50] J. Mork, B. Tromborg, and J. Mark, *Chaos in semiconductor lasers with optical feedback: theory and experiment*, IEEE J. Quantum Electron., 28 (1992), pp. 93–108.
[51] A. Naumenko, P. Besnard, N. Loiko, G. Ughetto, and J. C. Bertreux, *Characteristics of a semiconductor laser coupled with a fiber Bragg grating with arbitrary amount of feedback*, IEEE J. Quantum Electron., 39 (2006), pp. 1216–1228.
[52] M. Nizette and T. Erneux, *Optical frequency dynamics and relaxation oscillations of a semiconductor laser subject to filtered optical feedback* in Semiconductor Lasers and Laser Dynamics II, D. Lenstra, M. Pessa and Ian H. White, eds., Proceedings of SPIE 6184-32, 2006.
[53] Oclaro, *data sheets for grating-stabilized 980nm pump laser modules*; LC94 300mW, PLC94 Rev 3.1 August 2009; LC96 600mW, PLC96 Rev 4.1 August 2009.
[54] V. Pal, J. S. Suelzer, A. Prasad, G. Vemuri, and R. Ghosh, *Semiconductor laser dynamics with two filtered optical feedbacks* IEEE J. Quantum Electron., 49(3) (2013), pp. 340–349.
[55] T. Poston and I. Stewart Catastrophe Theory and its Applications, Pitman Publishing Ltd., 1978.
[56] F. Rogister, P. Mégret, O. Deparis, M. Blondel, and T. Erneux, *Suppression of low-frequency fluctuations and stabilization of a semiconductor laser subjected to optical feedback from a double cavity: theoretical results*, Opt. Lett., 24 (1999), pp. 2441-2443.
[57] F. Rogister, D. W. Sukow, A. Gavrielides, P. Mégret, O. Deparis, and M. Blondel, *Experimental demonstration of suppression of low-frequency fluctuations and stabilization of an external-cavity laser diode*, Opt. Lett. 25 (2000), pp. 808–810.
[58] D. Roose and R. Szalai, *Continuation and bifurcation analysis of delay differential equations*, in *Numerical Continuation Methods for Dynamical Systems, Pathfollowing and boundary value problems*, B. Krauskopf, H. Osinga, and J. Galán-Vioque, eds., pp. 359–399, Springer, Dordrecht, 2007.
[59] V. Rottschäfer and B. Krauskopf, *The ECM-backbone of the Lang-Kobayashi equations: a geometric picture*, Int. J. Bifurcation and Chaos, 17 (2007), pp. 1575-1588.
[60] T. Sano, *Antimode dynamics and chaotic itinerancy in the coherence collapse of semiconductor lasers with optical feedback*, Phys. Rev. A, 50 (1994), pp. 2719–2726.
[61] J. Sonksen, M. Ahmad, N. Storch, H. Krause, S. Blom, A. Pötzl, and H. Hillmer, *Controlling and tuning the emission of a semiconductor optical amplifier for sensor application by means of fiber Bragg gratings,* Proceedings of the 8th WSEAS Int. Conf. on Microelectronic, Nanoelectronics, Optoelectronics (2009), pp. 59-62.
[62] J. Sonksen, M. Ahmad, N. Storch, H. Krause, S. Blom, A. Pötzl, and H. Hillmer, *Aufbau eines faserbasierten Laserresonators mit zwei Fabri-Pérot Kavitäten und einer gemeinsamen aktiven Zone für Sensonrikanwendungen ,* DGaO Proceedings 2008; ISSN: 1614-8436.
[63] M. C. Soriano, J. García-Ojalvo, C. R. Mirasso, and I. Fischer, *Complex photonics: Dynamics and applications of delay-coupled semiconductors lasers*, Rev. Mod. Phys., 85 (2013), pp. 421–470.
[64] G. H. M. Van Tartwijk and D. Lenstra, *Semiconductor lasers with optical injection and feedback*, Quantum Semiclass. Opt., 7 (1995), pp. 87–143.
[65] B. Tromborg, J. Osmundsen, and H. Olesen, *Stability analysis for a semiconductor laser in an external cavity*, IEEE J Quantum Electron., 20 (1984), pp. 1023–1032.
[66] V. Z. Tronciu, C. R. Mirasso, and P. Colet, *Chaos-based communications using semiconductor lasers subject to feedback from an integrated double cavity*, J. Phys. B: At. Mol. Opt. Phys, 41 (2008), p. 155401.
[67] V. Z. Tronciu, H.-J. Wünsche, M. Wolfrum, and M. Radziunas, *Semiconductor laser under resonant*

feedback from a Fabry-Perot resonator: Stability of continuous-wave operation, Phys. Rev. E, 73 (2006), p. 046205.
[68] S. Valling, B. Krauskopf, T. Fordell, and A. Lindberg, *Experimental bifurcation diagram of a solid state laser with optical injection*, Optics Communications, 271 (2007), pp. 532–542.
[69] H. Venghaus (Ed.), *Wavelength Filters in Fibre Optics*, Springer, Berlin, 2006.
[70] S. M. Verduyn Lunel and B. Krauskopf, *The Mathematics of Delay Equations with an Application to the Lang-Kobayashi Equations*, in *Fundamental Issues of Nonlinear Laser Dynamics*, B. Krauskopf and D. Lenstra, eds., AIP Conference Proceedings 548, pp. 66-87, AIP, Melville, New York, 2000.
[71] S. Wieczorek, B. Krauskopf, and D. Lenstra, *A unifying view of bifurcations in a semiconductor laser subject to optical injection*, Opt. Commun., 172 (1999), pp. 279–295.
[72] S. Wieczorek, B. Krauskopf, and D. Lenstra, *Sudden chaotic transitions in an optically injected semiconductor laser* , Opt. Lett, 26 (2001), pp. 816–818.
[73] S. Wieczorek, B. Krauskopf, and D. Lenstra, *Unnested islands of period doublings in an injected semiconductor laser* , Phys. Rev. E, 64 (2001), p. 056204.
[74] S. Wieczorek, T. B. Simpson, B. Krauskopf, and D. Lenstra, *Bifurcation transitions in an optically injected diode laser: theory and experiment*, Optics Communications, 215 (2003), pp. 125–134.
[75] S. Wieczorek, B. Krauskopf, T. B. Simpson, and D. Lenstra, *The dynamical complexity of optically injected semiconductor lasers*, Physics Reports, 416 (2005), pp. 1–128.
[76] J. Ye, H. Li, and J. G. McInerney,, *Period-doubling route to chaos in a semiconductor laser with weak optical feedback* , Phys. Rev. A, 47 (1993), pp. 2249–2252.
[77] M. Yousefi and D. Lenstra, *Dynamical behaviour of a semiconductor laser with filtered external optical feedback*, IEEE J. Quantum Electron., 35 (1999), pp. 970–976.
[78] M. Yousefi, D. Lenstra, A. Fischer, and G. Vemuri, *Simulations of a semiconductor laser with filtered optical feedback: deterministic dynamics and transitions to chaos*, in *Physics and Simulation of Optoelectronic Devices X*, P. Blood, M. Osinski, and Y. Arakawa, eds., Proceedings of SPIE 4646, pp. 447–452, 2002.
[79] M. Yousefi, D. Lenstra, and G. Vemuri, *Nonlinear dynamics of a semiconductor laser with filtered optical feedback and the influence of noise*, Phys. Rev. E, 67 (2003), p. 046213.
[80] M. Yousefi, D. Lenstra, G. Vemuri, and A. P. A. Fischer, *Control of nonlinear dynamics of a semiconductor laser with filtered optical feedback*, IEEE Proc. Optoelectron., 148 (2001), pp. 223–237.

Appendix A. How to find the EFM-surface.

We employ a number of numerical techniques to compute the EFMs and render them as surfaces. This is done in a number of steps. First, for the chosen parameter values, we compute a sufficient number of constant dC_p-sections through the EFM-surface by means of numerical continuation. In Sec. 3 we showed that the EFMs can be calculated as solutions of the transcendental equations (3.3)–(3.8). Hence, these equations could be used to continue EFMs in parameters with any numerical continuation package. However, this approach has the disadvantage that it does not provide information on the stability of the EFMs. To overcome this difficulty we find and continue the EFMs directly as isolated equilibria of the transformed DDE system (A.2)–(A.6) with the MATLAB package DDE-BIFTOOL [11]. We then use this computed data to render the EFM-surface in (ω_s, N_s, dC_p)-space. Finally, we add computed stability information to the EFM-surface and its two-dimensional projection. We developed a set of interactive MATLAB scripts and functions to automate these steps as much as is practical.

We now describe our strategy to deal with the mathematical and numerical challenges associated with the analysis of the EFM structure of Eqs. (2.1)–(2.4).

A.1. Dealing with the S_1-symmetry of the 2FOF laser model. The DDE (2.1)–(2.4) shares an S^1-symmetry with many other systems with coherent optical feedback. Namely, since each term in equations (2.1) and (2.3)–(2.4) is linear in E, F_1 and F_2, and since E enters Eq. (2.2) only as its modulus $|E|$, the DDE is equivariant under any element $B_\beta \in S^1$ of the form

$$B_\beta = \begin{pmatrix} e^{i\beta} & 0 & 0 & 0 \\ 0 & 1 & 0 & 0 \\ 0 & 0 & e^{i\beta} & 0 \\ 0 & 0 & 0 & e^{i\beta} \end{pmatrix},$$

which is physically a rotation of the vector (E, N, F_1, F_2) by an angle β [29, 34, 40]. As a consequence, solutions of Eqs. (2.1)–(2.4) come as group orbits under the S^1-symmetry, meaning that any phase shift of the solutions is also a solution. For example, the simplest nonzero solutions or EFMs are circular limit cycles and they could be studied as such. However, to facilitate numerical continuation and stability analysis of EFMs, we would like to exploit the symmetry and study these limit cycles as isolated equilibria in some transformed system.

The symmetry cannot simply be divided out from the equations using a constant β, as is the case for an injected laser [75]. Instead, we substitute the ansatz

$$(E,\, N,\, F_1,\, F_2(t)) = \left(Ee^{ibt}, N, F_1e^{ibt}, F_2e^{ibt}\right) \tag{A.1}$$

into (2.1)–(2.4) and divide through by an exponential factor, which results in

$$\frac{dE}{dt} = (1+i\alpha)N(t)E(t) - ibE(t) + \kappa_1 F_1(t) + \kappa_2 F_2(t), \tag{A.2}$$

$$T\frac{dN}{dt} = P - N(t) - (1+2N(t))|E(t)|^2, \tag{A.3}$$

$$\frac{dF_1}{dt} = \Lambda_1 E(t-\tau_1)e^{-iC_p^1} + (i\Delta_1 - \Lambda_1 - ib)F_1(t), \tag{A.4}$$

$$\frac{dF_2}{dt} = \Lambda_2 E(t-\tau_2)e^{-iC_p^2} + (i\Delta_2 - \Lambda_2 - ib)F_2(t). \tag{A.5}$$

where b is an extra free parameter. A suitable choice of b 'freezes' motion along the group orbit so that an EFM becomes a circle of inifintely many equilibria. This phase indeterminacy of E appears because system (A.2)–(A.5) is underdetermined: one has to solve for a suitable b for each group orbit so there are more unknowns than equations. In practice, to analyse the system with DDE-BIFTOOL, it is helpful to resolve the phase indeterminacy by considering the intersection of the group orbits with the fixed six-dimensional half space

$$S = \{(E,\, N,\, F_1,\, F_2)\,|\,\mathrm{Im}(E) = 0 \quad \text{and} \quad \mathrm{Re}(E) \geq 0\}\,. \tag{A.6}$$

These intersections are also called the trace of the solution [34, 40]. In this way, a continuous wave or an EFM of Eqs. (2.1)–(2.4) can be represented by a unique equilibrium in a six-dimensional sub-space and by the associated unique value of b. This numerical approach also has a physical interpretation: the free parameter b is equivalent to the frequency ω_s of an EFM; see Sec. 3. Note that solutions of system (A.2)–(A.5) have the same stability properties as the solutions of system (2.1)–(2.4). In particular, owing to the symmetry, they have a trivial zero eigenvalue, which must be taken into account for the appropriate stability and bifurcation analysis of the solutions [17, 40, 45].

The implementation of the above strategy in DDE-BIFTOOL is achieved as follows: in addition to defining system (A.2)–(A.5) in the form of seven real equations in file `sys_rhs.m`, one also needs to specify the condition $\mathrm{Im}(E) = 0$ as an extra equation in the separate file `sys_cond.m`. This implementation works fine as long as $E \neq 0$.

A.2. Computation and rendering of the EFM-surface. To construct the EFM-surface in $(\omega_s,\, dC_p,\, N_s)$-space we first compute a number of sections that are uniformly distributed along the 2π dC_p-range considered. Typically, to construct the EFM-surface, for $d\tau = 0$, in Sec. 5, we use 150 values of dC_p that are distributed uniformly along the dC_p interval of length 2π. However, the actual number and distribution of the points along the dC_p-axis may be adjusted to the type of the EFM-surface.

Recall, that a section through the EFM-surface for fixed dC_p consists of the EFM-components, which are closed curves traced out by the EFMs with changing feedback phase; see Sec. 3.1. To find all EFM-components we use the boundary equation (4.1) to find for each chosen value of dC_p boundary values of ω_s at the left end point of each EFM component; note that for $d\tau = 0$ there are at most three such boundary values of ω_s for each value of dC_p. We then set $C_p^1 = 0$ and use Eq. (3.5)–(3.8) to compute initial values of the other state variables. Since $C_p^1 = 0$ is only a guess, we use DDE-BIFTOOL's correction routine to correct the values of C_p^1 and of the state variables to obtain a first point on the EFM-component in question; during this correction step the values of ω_s and dC_p are kept fixed. For the purpose of surface rendering, it is advantageous that all of the EFM-components be computed in one direction, e.g. clockwise. We therefore take the first point and apply a small positive perturbation to the corrected value of C_p^1. We then again use DDE-BIFTOOL's correction routine to find this second point on the EFM component, which can then be continued with DDE-BIFTOOL for increasing C_p^1. As the result of this procedure, we obtain a set of uniformly distributed constant dC_p sections through the EFM-surface, each of which may consist of up to three EFM-components.

To render the EFM surface from these many EFM-components we make use of our knowledge of the surface type. We first group all the computed EFM-components according to the particular bands and island of the EFM-surface to which they belong. In case there are holes or bulges, we identify the associated group of EFM-components. We then consider the intervals of the 2π dC_p-range within which the number of the EFM-components is dC_p-independent and generate separate meshes to render the corresponding local segments of the EFM-surface. More specifically, we first check that each of the m EFM-components in the local segment is a single closed loop, and we trim it otherwise (since, C_p^1 is 2π-periodic it is possible to go along the EFM-component more than once); here m is the number of EFM-components in the local segment. Next, we rewrite the values of ω_s, dC_p and N_s of each point of an EFM-component from the DDE-BIFTOOL solution branch structure into a $3 \times k$ matrix K, where k is the number of points along the branch. Additionally, to ensure a smooth rendering of the surface we apply constant arclength interpolation along each curve defined by K; as a result, we obtain a new $3 \times l$ matrix L that consist of l uniformly spaced mesh points. Finally, we split each of the m matrices L into rows, and construct three separate $m \times l$ mesh matrices, for ω_s, dC_p and N_s, which are used to plot the local segment of EFM-surface; recall that, l is the number of mesh points (after arclength interpolation) and m is the number of EFM-components in the considered group. These meshes for the different groups of EFM-components are then pieced together into an overall, smooth EFM-surface; this may require the computation of some additional branches of the EFMs.

The above procedure has been implemented as a MATLAB function that automatically generates a mesh from the local segments of the EFM-components that correspond to a band or an island of the EFM-surface; the mesh yields a surface when plotted with the built-in MATLAB functions `surf` and `light` with appropriate parameters. We process each band or island of the EFM-surface separately, and later plot them one by one in the same figure. A typical size of the mesh representing the whole EFM-surface (over a 4π dC_p-range) in Sec. 5 is about $3 \times 300 \times 1500$ points.

A.3. Determining and visualizing EFM-stability. The figures in sections Sec. 5 and 6 showing the EFM-stability regions on the EFM-surface are the result of quite extensive and elaborate computations. In fact, the computation with DDE-BIFTOOL of an EFM component with stability information takes about 20 times longer than that without stability information. Therefore, the EFM-stability information is computed only for every other of the dC_p-slices that are used to construct the EFM-surface, that is, typically for 75 sliced over the 2π dC_p-interval. Moreover, we limit the number of computed points along each EFM-component to 150. In spite of these restriction, it took around three hours to calculate the stability information for a single instance of the EFM-surface.

We checked the accuracy of the stability computations by checking the alignment of the stable segments of the EFM-components with their known boundaries, given by saddle-node and Hopf bifurcation curves. These bifurcation curves are computed separately by two-parameter continuations in C_p^1 and C_p^2; starting points are conveniently chosen from saddle-node and Hopf bifurcations found at the computed EFM-components. Curves of Hopf bifurcations can be found and continued with DDE-BIFTOOL directly in Eqs. (A.2)-(A.5). Saddle-node bifurcations, on the other hand, cannot be detected and continued with DDE-BIFTOOL due to the presence of an extra eigenvalue 0 (due to equivariance under phase shifts). Instead, curves of saddle-node bifurcations are computed as turning limit points (folds) of solutions of the transcendental system (3.3)–(3.8).

The computed branches of stable EFMs and the curves of saddle-node and Hopf bifurcations are plotted with the transparently rendered EFM surface in (ω_s, dC_p, N_s)-space. In this way, the EFM-stability regions appear as clearly bounded hatched patches on the EFM surface.